이학박사 학위논문

Interplay between emergent orders in quasi-two-dimensional superconductors $Cs(V_{1-x}Ti_x)_3Sb_5$ and $2H$-$Pd_{0.05}TaSe_2$

준 이차원 초전도체 $Cs(V_{1-x}Ti_x)_3Sb_5$ 및 $2H$-$Pd_{0.05}TaSe_2$의 상 사이 상호작용에 관한 연구

2023년 8월

서울대학교 대학원

물리천문학부

서 예 환

Interplay between emergent orders in quasi-two-dimensional superconductors $Cs(V_{1-x}Ti_x)_3Sb_5$ and $2H$-$Pd_{0.05}TaSe_2$

준 이차원 초전도체 $Cs(V_{1-x}Ti_x)_3Sb_5$ 및 $2H$-$Pd_{0.05}TaSe_2$의 상 사이 상호작용에 관한 연구

지도 교수 김 기 훈

이 논문을 이학박사 학위논문으로 제출함

2023년 8월

서울대학교 대학원

물리천문학부

서 예 환

서예환의 이학박사 학위논문을 인준함

2023년 8월

위 원 장 _____ 유 재 준 (인)

부위원장 _____ 김 기 훈 (인)

위 원 _____ 이 지 은 (인)

위 원 _____ 박 철 환 (인)

위 원 _____ 김 용 관 (인)

Interplay between emergent orders in quasi-two-dimensional superconductors $Cs(V_{1-x}Ti_x)_3Sb_5$ and $2H$-$Pd_{0.05}TaSe_2$

Yeahan Sur

Supervised by

Professor Kee Hoon Kim

A dissertation Submitted to the Faculty of

Seoul National University

in Partial Fulfillment of

the Requirements for the Degree of

Doctor of Philosophy

August 2023

Department of physics and Astronomy

Graduate School

Seoul National University

Abstract

Quantum phase transitions, which are phase transitions that take place at absolute zero temperature, have been an important phenomenon in the condensed matter physics community for more than a century. This rare phenomenon occurs near the phase space where the second-order thermal phase transition temperature reaches 0 K upon varying a nonthermal tuning parameter g. In this phase space, the correlation time of the ordered phase is governed by the equation $\xi_\tau \propto 1/[\ g - g_c]^{\nu z}$, where $\boldsymbol{\nu}$ is the correlation length component and $\boldsymbol{z}$ is the dynamical exponent, and g_c is the critical point of the tuning parameter. Near the phase space of $g = g_c$, the correlation time ξ_τ diverges and becomes larger than the thermal time scale L_τ. In this special case, the ground state of the material is defined as a fluctuating state where the wavefunctions of the ordered state and the disordered state are superposed. As a result, the physical properties are determined by the quantum fluctuation related to Heisenberg's uncertainty principle and can give rise to exotic physical properties such as superconductivity. This thesis focuses mainly on the quantum critical point of various orders and the superconducting state that emerges in proximity to their respective quantum phase transitions.

Firstly, the relation between charge bond order, electronic nematicity, and superconductivity in a kagome metal $Cs(V_{1-x}Ti_x)_3Sb_5$ is investigated. In this study, high-quality single crystals of $Cs(V_{1-x}Ti_x)_3Sb_5$ ($0 \leq x \leq 0.06$) have been successfully grown, with the accurate doping ratio and systematic lattice

variation confirmed by wavelength-dispersive X-ray spectroscopy (WDS) and X-ray diffraction (XRD) measurements, respectively. Elastoresistance measurements are employed in relation to the Ti ratio x to probe the interplay between nematic order and superconductivity. A careful examination of $Cs(V_{1-x}Ti_x)_3Sb_5$ single crystals reveals a systematic suppression of the Curie-Weiss temperature θ_{nem} upon Ti doping, which changes its sign to become negative at $x \sim 0.009$, close to the critical doping of $x_c = 0.01$, where the Curie constant and nematic susceptibility are found to reach their maximum values. This constitutes strong evidence of a nematic quantum critical point (NQCP) near x_c. Remarkably, the superconducting transition temperature and Meissner volume fraction exhibit an unusual double-dome feature as a function of x, with the center of the first dome located in the vicinity of the NQCP. These observations raise the intriguing possibility that fluctuations in the nematic order play an important role in the pairing interaction to optimize superconductivity in the first superconducting dome of $Cs(V_{1-x}Ti_x)_3Sb_5$.

Secondly, the relation between strong coupling charge density wave order and superconductivity in a transition metal dichalcogenide 2*H*-$Pd_{0.05}TaSe_2$ is investigated. High pressure is used as a nonthermal tuning parameter to investigate electrical transport and vibrational properties in a 2*H*-$Pd_{0.05}TaSe_2$ single crystal, with a CDW transition temperature $T_{CDW} = 115$ K and a superconducting transition temperature $T_c = 2.6$ K. Upon applied pressure, the T_{CDW}, indicated by a shoulder in the in-plane resistivity and a drop in the Hall coefficient, shifts towards lower temperature to 0 K near a

critical pressure of P_c ~ 22.1 GPa. Furthermore, analysis of low-temperature resistivity measured at a constant magnetic field of $\mu_0 H$ = 9 T reveals a five-fold enhancement of the quadratic power-law coefficient with pressure, indicating a significent increase in the electronic density of states. Additionally, the intensity of a two-phonon Raman mode exhibits systematic suppression at ~ 21.8 GPa, suggesting the disappearance of the phonon Kohn anomaly near this pressure. These observations strongly corroborate the presence of a pressure-induced CDW quantum critical point (QCP) at P_c, induced by a tunable Kohn anomaly in 2*H*-$Pd_{0.05}TaSe_2$. Our findings lay the foundation for understanding the relationship between various electronic orders and superconductivity in quasi-two-dimensional systems, by presenting two vital experimental platforms that exhibit quantum critical points and providing insights for the enhancement of superconductivity near their quantum critical regimes.

Keyword: quantum critical point, single crystal growth, quasi-2D materials, superconductivity, charge density wave, nematicity, doping, pressure, strain.

Student Number: 2015-20330

Contents

List of Tables

List of Figures

Chapter 1 Introduction

1.1 A brief overview of superconductivity

Ever since superconductivity was first discovered in 1911 at pure mercury (Hg) with a superconducting transition temperature of 4.2 K [1], superconductivity has been one of the most intriguing phenomena within the condensed matter physics community. Superconductivity is characterized by two unique features: perfect electrical conductivity and perfect diamagnetism (Figure 1.1). While perfect electrical conductivity can be easily determined by measuring the zero resistivity of a sample, a superconductor can be clearly distinguished from a simple perfect conductor, since a superconductor exhibits another feature called perfect diamagnetism. Perfect diamagnetism, also called the Meissner effect, refers to the expulsion of a magnetic field from a superconductor during its transition to the superconducting state. For some superconductors, this effect has been demonstrated to show magnetic forces large enough to levitate trains from metallic rails, leading to the elimination of friction between the wheels and the rails [2].

In order to understand the exotic properties of superconductivity, researchers have been searching for new superconductors and their underlying mechanisms for more than one century. At 1935, Fritz and Heinz London (the London brothers) focused on the combination of the Ohm's law and the Maxwell's equations, and established the London equations of superconductivity [3]. From these London equations, the idea of penetration

depth has been adopted, which could successfully explain the Meissner effect using the concept of supercurrents flowing inside a superconductor.

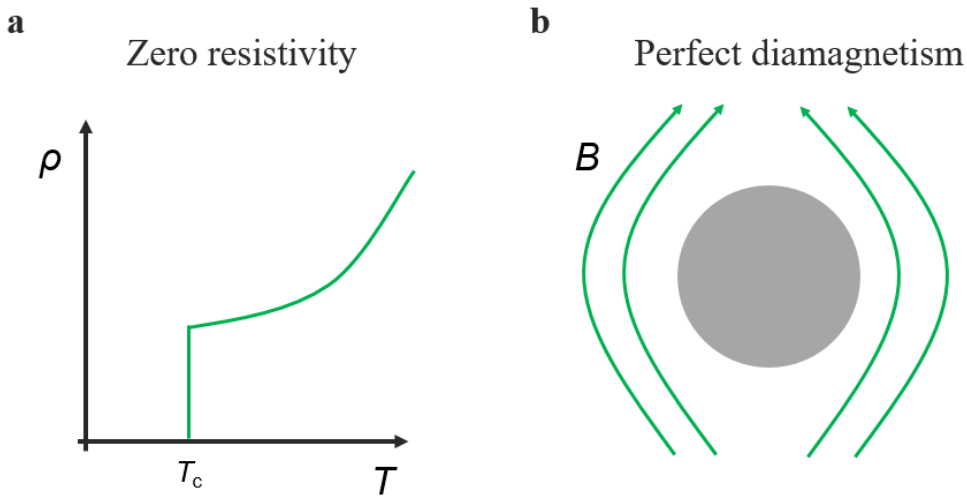

Figure 1.1 Two unique features of superconductivity: **(a)** perfect electrical conductivity and **(b)** perfect diamagnetism.

In 1950, Ginzburg and Landau introduced the Ginzburg-Landau (G-L) theory [4] that focuses on the second-order nature of the superconducting transition. The G-L theory was triumphant in two main features of superconductivity. Firstly, the G-L theory can successfully derive the London penetration depth which was predicted by the London brothers in the earlier studies. Secondly, the G-L theory derived another length scale, the Ginzburg-Landau coherence length, which is connected to the distance between the electrons that participate in superconducting pairing. By comparing these two length scales, namely the London penetration depth and the Ginzburg-Landau coherence length, the type of superconductivity can be determined, i.e. type-I superconductivity and type-II superconductivity. In a type-I superconductor,

flux vortices cannot penetrate the superconductor, leading to a single critical field (H_c), which is the magnetic field required to break the superconductinc order. In constract, in a type-II superconductor, the flux vortices can penetrate inside the superconductor at a certain range of magnetic fields between the lower critical field (H_{c1}) and the upper critical field (H_{c2}), leading to a more complex nature of superconductivity.

However, the most striking and important theory of superconductivity has been the famous Bardeen-Cooper-Schrieffer (BCS) theory, which was reported in the year of 1957. The BCS theory, named after its founders J. Bardeen, L. N. Cooper, and J. R. Schrieffer, is currently regarded as the first successful microscopic theory to explain the pairing mechanism of superconductivity [5]. The BCS theory postulates that an attractive interaction between electrons exists, which leads to the formation of correlated pairs of electrons called Cooper pairs. In this theory, as the temperature is cooled down, the Cooper pairs condense into a bosonic state and opens a superconducting energy gap in the Fermi surface. This superconducting energy gap paradoxically leads to the perfect electrical conduction in the superconductor, despite the depletion of electron density of states due to the energy gap opening. This striking theory has been shown to be highly effective in reproducing and explaining many experimental phenomena, including the Meissner effect, the energy gap at the Fermi energy level, and the isotope effect on the superconducting transition temperature. The isotope effect, which supports that heavier atoms lead to lower superconducting transition temperatures, has evidenced that the superconducting pairing of electrons is

mediated by lattice vibrations, or in other words, the phonon modes. It was eventually revealed that in most superconductors, the attractive interaction causing the pairing of electrons is indeed mediated by the phonons.

While the BCS theory has successfully explained superconductivity and related phenomena in traditional superconductors such as mercury (Hg), it has not been able to fully account for several newly discovered superconductors. One example is MgB_2, which is a conventional phonon-mediated superconductor that exhibits an exceptionally high transition temperature of 39 K. This exotic superconductivity exceeds the scope of the BCS theory, which assumes that all electrons behave in the same way. Indeed, subsequent researches revealed that multiple superconducting gaps of varying sizes exist, which eventually leads to the unexpected high transition temperature of 39 K [6]. Another example of great importance is the high-T_c cuprate superconductors. These Cu-based superconductors exhibit the Cu-O superconducting layer, and exhibits superconductivity at exceptionally high transition temperatures as high as 133-138 K ($HgBa_2Ca_2Cu_3O_{1+x}$) at ambient pressure [7]. In-depth studies of these cuprates with high transition temperatures have revealed that spin fluctuations in the compounds act as the pairing glue of the Cooper pair, substituting for the role of phonons in the conventional BCS superconductors. This spin-fluctuation-mediated superconductivity has been shown to be the underlying nature of the high transition temperature as well as other exotic superconducting properties in the cuprate superconductors, such as the anisotropic *d*-wave gap symmetry. Hence, this new type of superconductivity mediated by spin fluctuations is now

referred to as unconventional, while the phonon-mediated superconductivity is considered to be the conventional superconductivity. As the unconventional superconductors require more theoretical development beyond the conventional BCS theory, extended theories such as the multi-gap model [8] and the unconventional pairing mechanisms [9] have been developed and are being utilized up to now.

Apart from the Cu-based superconductors, the Fe-based superconductors represent another family of unconventional superconductors, which exhibit superconductivity up to approximately 50 K [10]. These superconductors all share a common structural component consisting of the Fe-As tetrahedral layer, which is reminiscent of the superconducting Cu-O layer in the high-T_c cuprate superconductors. Another commonality between the Fe-based and cuprate superconductors is their phase diagrams, which have been constructed by the temperature dependence of these superconductors studied via nonthermal tuning parameters such as chemical doping or external pressure. In detail, both superconducting systems in their pristine state exhbit a parent order i. e. spin density wave order for cuprates and nematic order for iron-based superconductors. With nonthermal tuning parameters such as pressure or doping, these parent orders can be suppressed, leading to the phase space where unconventional superconductivity is emerged [10, 11]. While the quantum fluctuations of the spin density wave order is thought to mediate superconductivity in the high-T_c cuprates, for the iron-based superconductors, quantum fluctuations of the nematic order is thought to mediate the superconducting pairing [12].

1.2 Kagome metals and kagome superconductors

In constrast to the Fe- and Cu- based superconductors which exhibit a superconducting Fe-As or Cu-O layer, superconductors that possess kagome structures have recently garnered considerable attention due to their potential realization of unconventional superconductivity. Due to their geometrical frusturation in real space, the materials with the kagome lattice hosts various peculiar features in their crystal momentum space, such as Dirac points, flat bands, and saddle points [13]. Recent theoretical calculations have indeed found that these electronic properties can lead to instabilities associated with the divergence in the density of states near the Fermi level (Figure 1.2) [13-16]. As such, several emergent orders, including charge bond order (CBO) [13-14], charge density order (CDO) [13], nematic order [15], and superconductivity (SC) [13-14, 16], have been theoretically predicted. For example, a functional renormalization group study on the kagome-Hubbard model predicted that CDW order and unconventional *d*-wave superconductivity can arise near a van Hove singularity at an electron filling of 5/4 per band [13].

The V-based kagome metals KV_3Sb_5, RbV_3Sb_5, and CsV_3Sb_5, which had been discovered in 2019, represent the experimental realizations of the various theoretical predictions, in the sense that the multiple van- Hove singularities exhibiting the divergent density of states are located very close to the Fermi level [17]. Moreover, these V-based kagome metals feature various orders predicted through theory, such as the charge order and superconductivity. Within this material class, the CsV_3Sb_5 stands as the most

extensively studied compound due to its highest superconducting transition temperature and the presence of additional orders. For example, below the charge order at T_{CDW} ~ 98 K, a nematic order is found at T_{nem} ~ 35 K which reduces the in-plane electronic rotational symmetry from C_6 symmetry to C_2 symmetry. At ~ 3.2 K, this sample exhibits a superconducting transition [18].

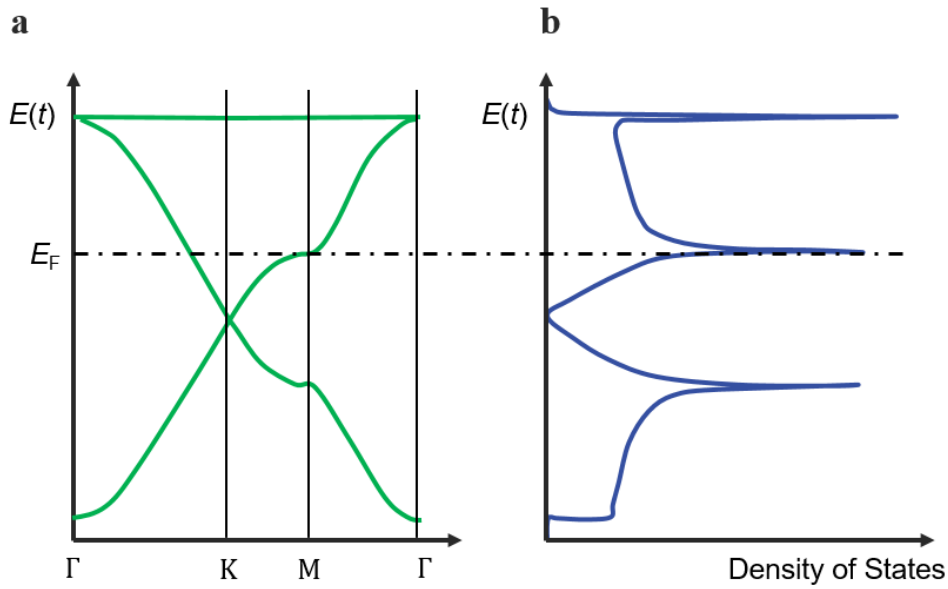

Figure 1.2 (**a)** The calculated electronic band for a theoretical kagome lattice in the kagome-Hubbard model. (**b)** The calculated electron density of states for the theoretical kagome lattice.

Currently, the charge and nematic orders are theoretically understood as the two types of charge bond orders (CBOs) [15]. Namely, the charge ordering at T_{CDW} is understood as a triple-q CBO with isotropic phase parameters, while the nematic ordering at T_{nem} is understood as a triple-q CBO with anisotropic phase parameters. Moreover, near the suppression of these CBOs, it has been predicted that quantum fluctuations of the charge bond order can mediate

sizable pairing glue for superconductivity, possibly resulting in superconductivity of various symmetries, including singlet s-wave, triplet *p*-wave, or *d*-wave superconductivity [13, 19]. Therefore, studying the nature of the superconducting order in CsV_3Sb_5, along with its relation with other emergent orders, has become an interesting puzzle in the condensed matter physics community.

1.3 Phase transitions and the quantum phase transition

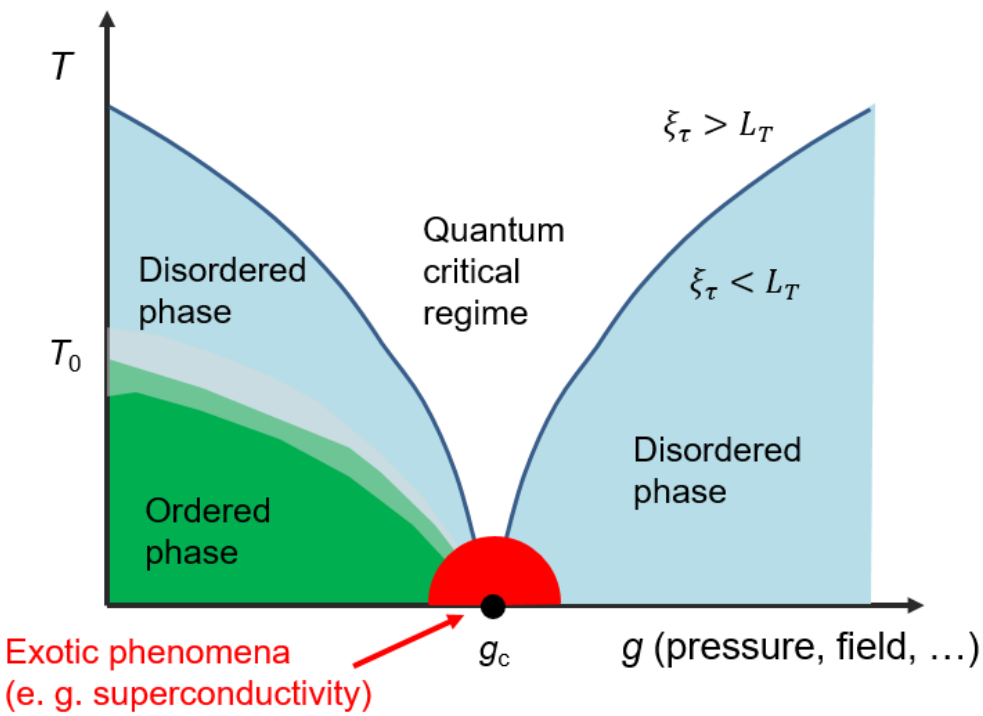

Figure 1.3 A cartoon figure of a phenomenological temperature (*T*)-tuning parameter (*g*) phase diagram. The green color indicates the ordered phase while the light blue color indicates the disordered phase. Near the thermal phase boundary between the ordered phase and the disordered phase, the coherence time ξ_τ is

always smaller than the thermal time scale L_τ. The white color indicates the quantum critical regime where ξ_τ is larger than L_τ. Near the zero temperature limit of the quantum critical regime, exotic phenomena can be exhibited, such as superconductivity.

Phase transitions, which can be distinguished into thermal and quantum phase transitions, has been an important phenomena in the condensed matter physics community for more than a century. Figure 1.3 illustrates a typical phase diagram of a material, with the horizontal axis representing the nonthermal control parameter g (such as pressure, doping, etc.) and the vertical axis representing temperature (T). When the material enters the ordered phase by lowering the temperature, a thermal phase transition can occur. In a thermal phase transition that takes place at a finite temperature, the correlation time of the ordered phase ξ_τ is always smaller than the thermal time scale $L_\tau = \hbar/k_B T$. In this thermal phase transition case, the ground state wavefunction of the ordered phase is always well-defined. However, near the phase space where the 2nd order thermal phase transtion temperature reaches 0 K, the material undergoes a quantum phase transition at $g = g_c$, in which a phase transition takes place at absolute zero temperature. In this case, the correlation time of the ordered phase is governed by the equation $\boldsymbol{\xi_\tau \propto 1/[\, g - g_c]^{\nu z}}$, where $\boldsymbol{\nu}$ is the correlation length component and $\boldsymbol{z}$ is the dynamical exponent [20]. Near the phase space of $g = g_c$, the correlation time $\boldsymbol{\xi_\tau}$ diverges and becomes larger than the thermal time scale L_τ, as illustrated in Figure 1.3.

In this special case, the ground state of the material is defined as a

fluctuating state where the wavefunctions of the ordered and disordered states are superposed. In this regime, the physical properties are determined by the quantum fluctuation related to the Heisenberg's uncertainty principle and can give rise to exotic physical properties such as superconductivity [20]. The following chapters of this thesis mainly focus on the quantum critical point of various orders and the superconducting state that emerges in proximity to the their quantum phase transitions.

Chapter 2 Experimental methods

2.1 Single crystal growth of intermetallic materials

To ensure the synthesis of high-quality single crystals and the stabilization of optimal growth conditions for various doping ratios, it is crucial to have a good understanding of the growth mechanism before exploring the physical properties of a system. In this chapter, we will introduce two different growth methods for intermetallic compounds: the flux growth method and the chemical vapor transport growth method.

2.1.1 Cs-Sb eutectic flux growth of CsV_3Sb_5

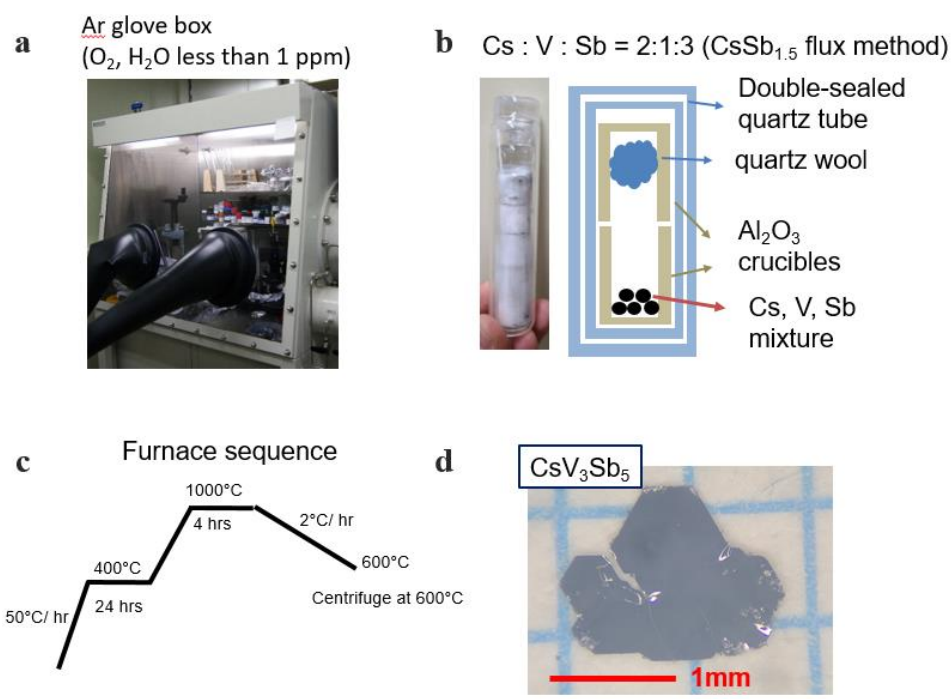

Figure 2.1 (**a)** A photograph of a conventional glove box in Prof. Kee Hoon Kim's lab. An atmosphere of inert Ar gas with O_2 and H_2O content below 1 parts per million is maintained to prevent unwanted reaction between air and the elemental compounds. (**b**) A photograph of a double-sealed quartz tube containing mixtures of the elemental Cs, V, Sb compounds covered in Al_2O_3 crucibles. The stoichiometric ratios of Cs, V, and Sb is controlled to be 2: 1: 3 in order to utilize the Cs-Sb mixture ($CsSb_{1.5}$) as a eutectic flux material. (**c**) The furnace sequence of the optimal growth condition of CsV_3Sb_5 flux growth. (**d**) A photograph of a well-grown CsV_3Sb_5 single crystal. A red scale bar indicates 1 mm length.

Since the Cs element required for the growth of CsV_3Sb_5 is highly air-sensitive, the sample preparation of the CsV_3Sb_5 was done in an Ar glove box, as shown in the optical image of Figure 2.1**a**. In the glove box filled with inert Ar gas, stochiometric amounts of Cs: V: Sb = 2: 1: 3 were weighed and placed between the alumina crucible as shown in Figure 2.1**b**. The alumina crucible was then inserted inside a double-sealed quartz tube with vaccuum conditions of $P \sim 10^{-5}$ Torr. The sealed quartz tubes were then treated in a furnace sequence as shown in Figure 2.1**c**. It is noted that the quartz ample was soaked in 400℃ for 24 hours before the actual flux growth at ~ 1000℃. This procedure is required to stabilize the formation of the liquid phase of the $CsSb_{1.5}$ eutectic flux in advance. If this sequence is omitted, the Cs liquid can vaporize at 670℃ and exhibit a high partial pressure at 1000℃, resulting in the breakage of the quartz tube. After this sequence, the melting process was carried out at 1000℃. The growth was performed while slowly lowering the temperature at a rate of 2℃/hr. Centrifuging the resulting material at 600℃ results in a clean separation of the hexagonal-shaped CsV_3Sb_5 single crystal

from the molten flux, as can be seen in Figure 2.1**d**. The synthesized crystals exhibit shiny plate-like morphologies, with a typical lateral area of 3 × 2 mm^2.

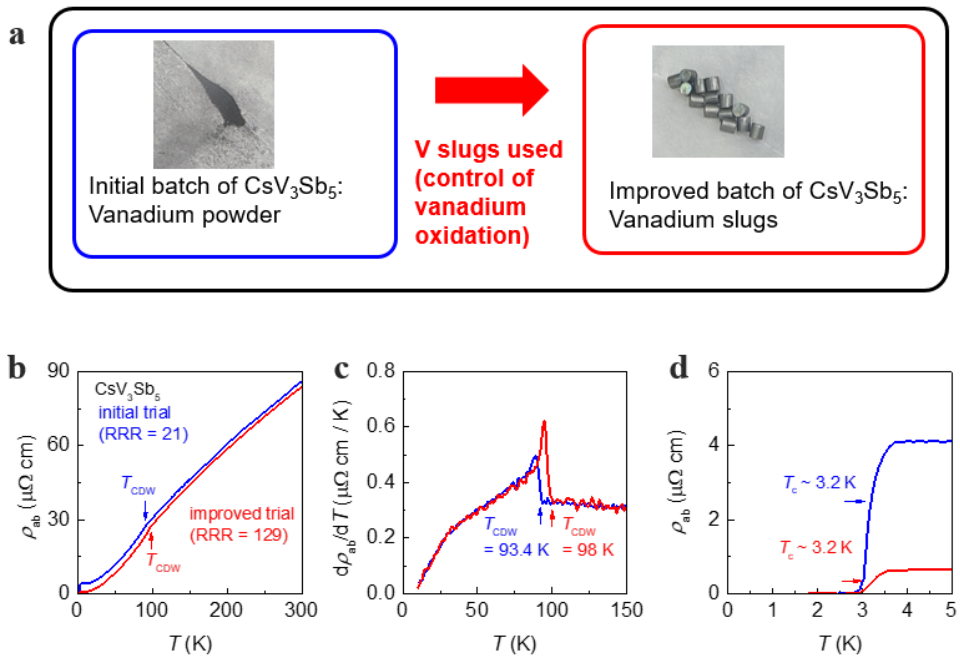

Figure 2.2 (**a)** Photographs of the vanadium starting materials of the initial batch and the improved batch. The photographs were taken inside the globe box. (**b**) Temperature dependence of the in-plane resistivity ρ_{ab} of CsV_3Sb_5 grown by different starting materials. The blue curve represents the data obtained from the powder-grown CsV_3Sb_5, while the red curve represents the data obtained from the slug-grown CsV_3Sb_5. (**c**) Temperature dependence of the derivative in the in-plane resistivity $d\rho_{ab}/dT$ of CsV_3Sb_5 grown by different starting materials. (**d**) Temperature dependence of the in-plane resistivity ρ_{ab} of CsV_3Sb_5 magnified near the low temperature region.

In order to improve the sample quality of the obtained CsV_3Sb_5 single crystals, several trial and error processes were carried out. Through multiple attempts, it was found that controlling the oxidation of the vanadium source

material is crucial in determining the sample quality of this material. As shown in Figure 2.2a, the initial trial of CsV_3Sb_5 growth was performed with the powder form of V, while the improved trial of CsV_3Sb_5 growth was performed with the slug form of V. Figure 2.2**b-d** shows the in-plane resistivity (Figure 2.2**b**), derivative of resistivity (Figure 2.2**c**), and low-temperature resistivity (Figure 2.2**d**) of the CsV_3Sb_5 samples grown by the initial method and the improved method. It can be seen that the low-temperature resistivity $\rho_{ab,\,0}$ shows a large variation between the two samples. As a lower $\rho_{ab,\,0}$ indicating lower impurity scattering is generally viewed as an indication of sample quality, this indicated that the slug-grown CsV_3Sb_5 single crystals exhibit better sample quality than the powder-grown CsV_3Sb_5 single crystals. This can be additionally confirmed by the comparision of the residual-resistivity-ratio (RRR), which is the ratio of the ρ_{ab} measured at 300 K and the $\rho_{ab,\,0}$. It can be immediately seem that the slug-grown CsV_3Sb_5 exhibits a high RRR of 129.

RRR	$\rho_{ab,0}$ (μΩ cm)	T_{CDW} (K)	Reference
16	3.8	92.2	[21]
33	3.8	94	[22]
118	1	95.4	[23]
129	0.65	98	This work (improved trial)

Table 2.1 A comparison between RRR, $\rho_{ab,0}$, and T_{CDW} between this work and other groups in the literature.

Achieving high-quality single crystals is essential for measuring intrinsic physical quantities, as it can be immediately seen by the difference of the charge ordering temperatures T_{CDW} of the CsV_3Sb_5 samples grown by the two different starting materials(Figure 2.2**c**). The charge ordering temperature of the powder-grown sample exhibits a low T_{CDW} = 93.4 K, while the slug-grown sample exhibits a relatively high T_{CDW} = 98 K. This same trend seems to hold in comparision with other group's data also, as seen in the Table 2.1. As compared with other group's data, the CsV_3Sb_5 crystals obtained in this work exhibits the highest RRR = 129, as well as the lowest $\rho_{ab,\,0}$ = 0.65 μΩ cm and the highest T_{CDW} = 98 K.

2.1.2 Chemical vapor transport growth of 2*H*-Pd_xTaSe_2

Chemical vapor transport (CVT) is a growth method for single crystals that utilizes chemical transport agents such as chlorine (Cl_2), bromine (Br_2), and iodine (I_2). This technique is often employed when flux growth is not feasible due to complex elemental phase diagrams and/or incongruent melting conditions. As compared to the flux method, the CVT method has advantages for single crystal growth since this method does not involve any melting process and only requires polycrystalline samples and a transport agent to grow the single crystals. The detailed growth process, as illustrated in Figure 2.3**a**, involves placing the target polycrystalline powder material and transport agent in a quartz tube and sealing the tube at a vacuum level of approximately $P = 10^{-5}$ Torr. For the single crystal growth, a finite temperature gradient is set

in a tube furnace or two-zone furnace, where the transport agent relocates the target material slowly from the hot zone to the cold zone and the resulting single crystals are grown within a time scale of several weeks.

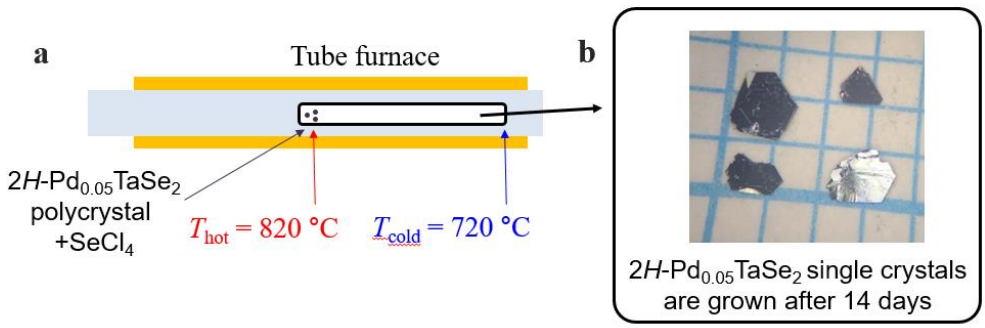

Figure 2.3 (**a**) A schematic picture of a CVT growth apparatus. A finite temperature gradient is set in a tube furnace, in which the hot zone temperature is set to T_{hot} = 820℃ and a cold zone temperature is set to T_{cold} = 720℃. A sealed quartz tube is placed between the hot zone and the cold zones, in which the target material 2*H*-$Pd_{0.05}TaSe_2$ and the transport agent $SeCl_4$ is placed at the hot zone. After the growth time of ~ few weeks, single crystals of the target material are grown in the cold zone, which can be well visualized in the photograph of a 2*H*-$Pd_{0.05}TaSe_2$ single crystal in (**b**).

In the case of 2*H*-$Pd_{0.05}TaSe_2$, the hot zone temperature was set to 820℃, and the cold zone temperature was set to 720℃ to induce the growth of the 2*H*-phase. To promote rapid growth, solid selenium tetrachloride ($SeCl_4$) was added, which produces the chlorine (Cl_2) transport agent as the Se and Cl_2 are separated at high temperatures. It is worth noting that as the molecular weight of the agent decreases in the order of Br_2 -> I_2 -> Cl_2, faster growth of the target single crystal occurs. While the Cl_2 is, in principle, favorable for the transport growth, Cl_2 in its gaseous form is toxic, which

makes it challenging to use in its gaseous state in laboratory settings. Therefore, I_2 is more commonly used due to safety issues. In order to overcome this experimental hurdle, in this study, the solid form of $SeCl_4$ was added at room temperature, which is safe to use at room temperature conditions, and is separated to Se and Cl_2 to provide the Cl_2 gas at higher temperatures. By utilizing this method, large single crystals of mm sizes could be successfully grown. The molecular amount of $SeCl_4$ per quartz tube was determined by calculating the ideal gas law at the maximum temperature, to make sure that the pressure of Cl_2 would not exceed one atmosphere at the maximum temperature of 820℃. The resulting single crystals grown using this method were formed in the cold zone, and their images can be seen on Figure 2.3**b**.

2.2 Capillary XRD measurement

Whenever a single crystal is grown, it is mandatory to check the sample quality before measurements of the physical properties can be performed. In this sense, X-ray diffraction measurements offer information of the grown crystals, as the lattice symmetry as well as the lattice parameters can be determined using the Bragg's law of $n\lambda = 2d \sin\theta$. For XRD measurements of the single crystals, the utilization of the capillary tube is recommended since this method has powerful advantages as compared to power diffraction measurements. First, measurements performed using a spinning capillary exhibit minimized preferred orientation, which enables better fitting results to

the theoretical predictions. Secondly, capillary measurements require only a small fraction of the powder of the ground single crystals, which can minimize the consumption of the valuable single crystal. Thirdly, the entire loading and sealing process in the capillary tube can be done inside the glove box, which can protect the powder from exposure to air or moisture if necessary.

There are two methods for implementing the capillary technique. The first is the Bragg-Brentano geometry, also known as the reflection geometry. This method is commonly used with standard sample holders and can be easily employed without modifying the instrument settings. The second is the Debye-Scherrer geometry, which is commonly reffered to as the transmission geometry. These two methods are complementary to each other, and several factors must be considered before choosing the appropriate geometry to use.

Firstly, samples with high absorption coefficients are unsuitable for transmission geometry, as the sample itself becomes an efficient beam stopper. Secondly, the sample quantity must be carefully calculated for the transmission geometry. A relatively small sample cross section reduces the measured intensity, but increasing the sample size does not necessarily enhance the intensity. This is because transmission through the sample and capillary is accompanied by diffraction, and larger samples result in longer transmission paths, ultimately reducing the signal intensity.

For successful sample loading, the single crystals must be grinded to fine powders. If the powder is too coarse, the capillary will be blocked, and will result in an insufficient amount of powder loaded in the capillary tube.

However, over-grinding of the single crystal can induce strain effects, which leads to broadened sample signals in the XRD measurements. Therefore, it is crucial to carefully grind the powder to an intermediate level.

Loading and aligning the capillary tube on the goniometer are the primary challenges of this measurement. For successful loading, it is recommended to secure the capillary tube to the holder using a sufficient amount of paraffin wax. After melting the wax with a gas lighter, the liquid is inserted into the capillary tube, which solidifies after a few seconds, sealing the powders inside the tube. After sealing the tube, additional treatment of the paraffin wax is required to firmly attach the tube to the holder. Aligning the capillary tube is difficult to perform with the naked eye. In this case, it is recommended to align the tube under a CCD-attached optical microscope, as the CCD pixels can provide an excellent guideline for the center axis of the capillary tube rotation.

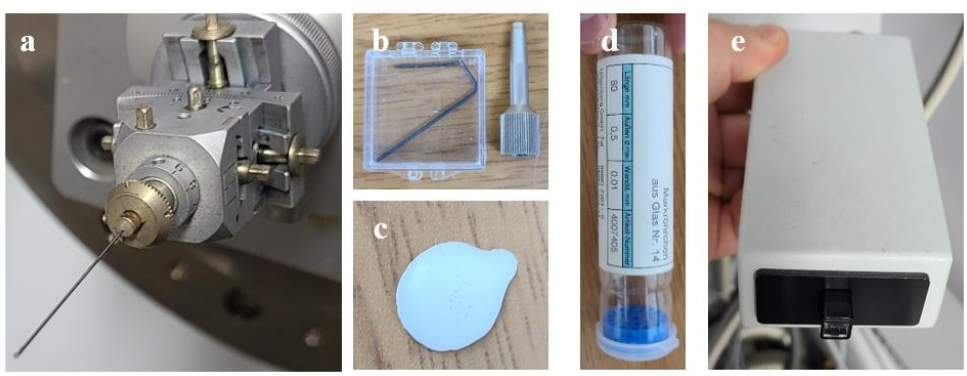

Figure 2.4 (**a**) A photograph of the spinning capillary tube loaded in the HRXRD apparatus (PANalytical Empyrean) in Prof. Kee Hoon Kim's lab. Photographs of (**b**) wrenches for adjusting the goniometer, (**c**) paraffin wax for sealing the capillary tube, (**d**) a glass capillary tube for XRD measurement, (**d**)

and a switch which enables the spinning option in the HRXRD apparatus.

In order to find the optimal condition, several options have to be considered. A thinner capillary with very fine powder filled as much as possible is better for most of the cases. Proper alignment of the spinning stage and a combination of appropriate slits are also crucial. The typical process for preparing a capillary involves the following steps:

First, prepare the sample by ensuring that the crystal pieces or powder have a very small or fine particle size, enabling them to fit into the capillary. Next, remove the capillary tube from its carrier and place it in a lab-made holder, such as a paper cup with a hole at the bottom, while taking care not to break the capillary. Slowly pour the sample into the capillary, utilizing a sharpened wooden stick if necessary to insert the samples through the narrow entrance. A weighing paper folded along the diagonal direction is good to use. Position the sample at the very end of the capillary, using shaking or tapping motions if required. After loading the sample, carefully seal or cut the capillary to an appropriate length of 5-7 cm, bearing in mind that sealing is preferred above cutting to prevent the sample from spilling out.

Then, place the prepared capillary into an adapter, aligning it with the grooved side of the Cu adapter. Apply paraffin to the adapter's empty hole and melt it with a soldering iron or gas lighter; carefully insert the capillary into the hole and ensure it is straight before the paraffin solidifies. Properly mount the adapter and capillary on the spinning stage, and align the stage so that the capillary is perfectly straight, using the two linear stages and two angular

alignment goniometers on the stage. Rotate the stage manually during the alignment to check the status.

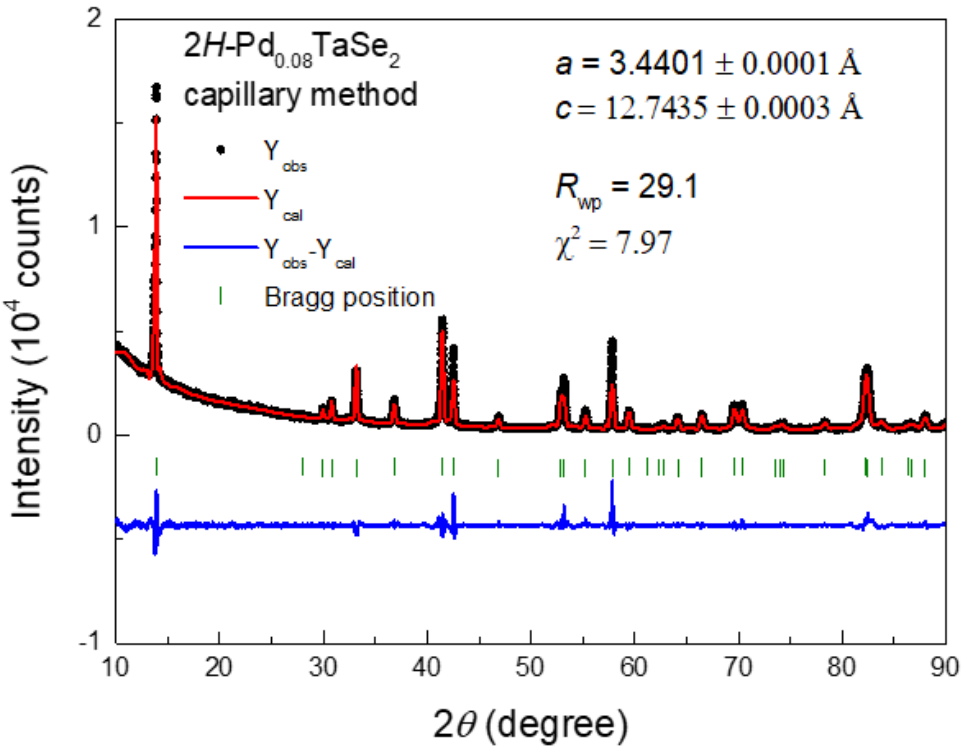

Figure 2.5 An XRD pattern of a capillary measurement of the ground crystal of 2*H*-$Pd_{0.08}TaSe_2$ (black dot), the Rietveld refinement result (red line) with R_{wp} = 29.1 and χ^2 = 7.97, and their subtracted patterns (blue line) along with the expected XRD peak positions (green ticks). Rietveld refinement of the XRD spectra shows lattice parameters of a = 3.4401 Å, c = 12.7435 Å, respectively.

If all these preparations are completed, mount the stage on the diffractometer, connect the motor supply cable to the stage, and turn on the switch to spin the capillary, noting that the switch is a manual one and cannot be controlled externally by the computer. Measure the diffraction in a minimized angle sweep around the main XRD peak to check the signal-to-

noise ratio, and adjust the slit combination to find the optimal condition. Finally, carefully measure the diffraction pattern, performing numerous repetitions with the appropriate time per step to accumulate sufficient intensity.

Figure 2.5 shows a typical measurement data using the capillary XRD method (2*H*-$Pd_{0.08}TaSe_2$). Even though the XRD measurement was performed in grinded single crystals, polycrystalline-like XRD data are achieved, which is due to the minimization of the preferred orientation in the spinning capillary tube.

2.3 Elastoresistance measurement

For materials exhibiting nematic order, studying the electronic anisotropy resulting from applied strain can provide valuable insights into the characteristics of the nematic order parameter. Specifically, analyzing variations in electrical anisotropy as a function of strain changes enables the determination of nematic susceptibility [24]. The nematic susceptibility, as denoted by the symbol $\tilde{n}$, can be determined by measuring the anisotropic change in resistance induced by anisotropic strain ε.

Figure 2.6**a** shows a schematic figure for the elastoresistance measurement. To measure the elastoresistance, a device called the piezo stack is used, which is capable of extending the length in one direction while contracting the length in a perpendicular direction. As illustrated in the figure, when a positive voltage is applied to the piezo stack, its length expands in the

x-direction when a positive voltage is applied. By gluing two single crystals with the *a*-axis parallel to the Cartesian *x*-axis on this deformable device, we can measure the change in resistance in response to the voltage applied to the piezo stack. Here, R_{xx} refers to the resistivity measured with the current and voltage applied on the *x* direction, while the R_{yy} refers to the resistivity measured with the current and voltage applied on the *y* direction.

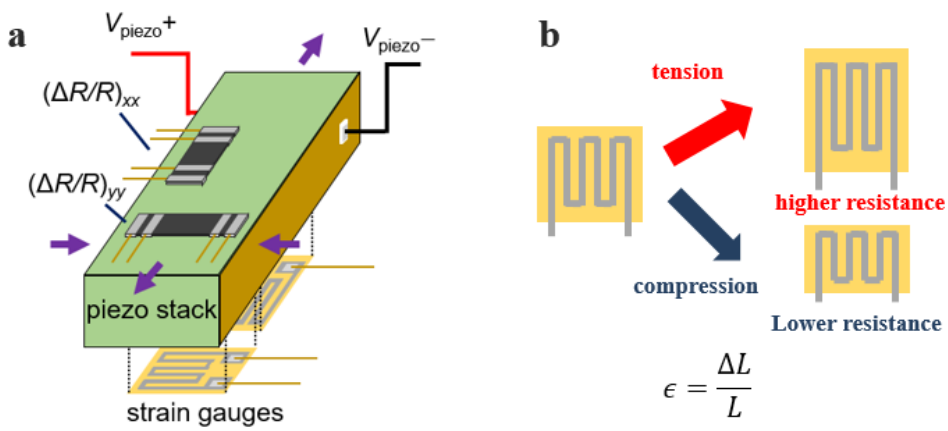

Figure 2.6 (**a**) A schematic figure of the elastoresistance measurement apparatus. (**b**) A schematic figure of a strain gauge and its working principle.

The applied directional strains induced by the piezo stack are precisely measured by the strain gauges glued on the back side of the piezo stack. Figure 2.6**b** shows a schematic figure of a strain gauge. As ε_{xx} and ε_{yy} is defined by the length change in the *x* and *y* directions, $\varepsilon_{xx} = \Delta L_x/L_x$ and $\varepsilon_{yy} = \Delta L_y/L_y$, the applied strain for each direction can be measured by measuring the length change in the strain gauges. The length changes, which is equal to strain, can be directly measured by the resistance change in the strain gauge, in which an increase in the resistance corresponds to the tension while a decrease in the

resistance corresponds to the compression on the specific direction. It is known that the nematic susceptibility can be obtained by measuring the anisotropic change in the resistance $N \equiv (\Delta R/R)_{xx} - (\Delta R/R)_{yy}$ in response to the anisotropic strain $(\varepsilon_{xx}–\varepsilon_{yy})$, $\tilde{n} = dN/d(\varepsilon_{xx}–\varepsilon_{yy})$. This measurement technique enables the acquisition of information about the electronic anisoptopy (1D modulation) in the single crystal.

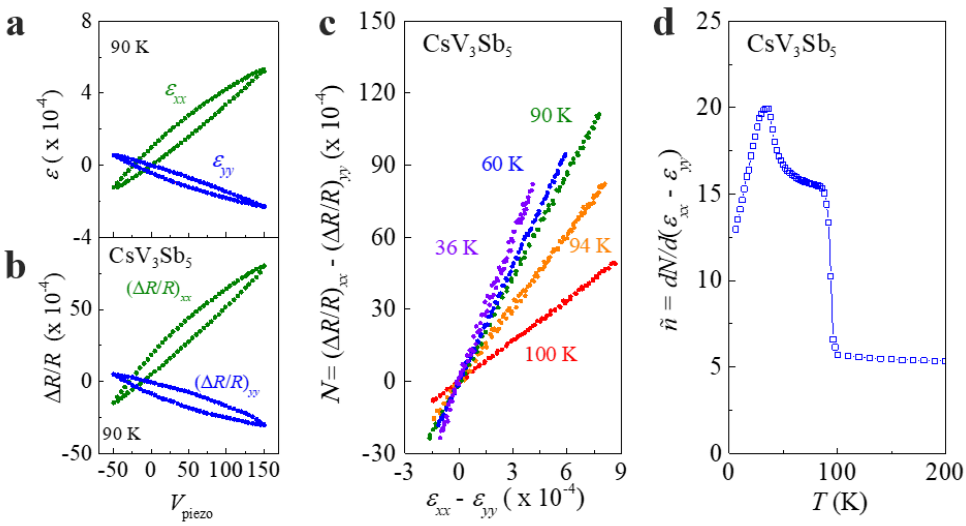

Figure 2.7 (**a**) Piezo voltage *vs*. strain plot for the *xx* and *yy* directions measured using the strain gauges at 90 K. (**b**) Piezo voltage *vs*. relative resistivity change plot for the *xx* and *yy* directions measured in CsV_3Sb_5 at 90 K. (**c**) $N = (\Delta R/R)_{xx} - (\Delta R/R)_{yy}$ *vs*. $(\varepsilon_{xx}–\varepsilon_{yy})$ plot for various temperatures. (**d**) $\tilde{n} = dN/d(\varepsilon_{xx} – \varepsilon_{yy})$ vs. T plot for CsV_3Sb_5.

Figure 2.7**a** shows the relationship between piezo voltage and strain ε_{xx} and ε_{yy}. Here, the piezoelectric voltage is applied in a range of V_{piezo} = -50 V to 150V, which represents the maximum voltage range that can be applied in the piezo stack without causing damage. Owing to the inherent properties of piezoelectric materials, the piezoelectric stack typically generates hysteresis

loops in the induced strain, which are clearly illustrated in both the ε_{xx} and ε_{yy} plots. Figure 2.7**b** shows the relationship between the voltage applied to the piezoelectric stack and the relative resistivity change $(\Delta R/R)_{xx}$ and $(\Delta R/R)_{yy}$ for a CsV_3Sb_5 single crystal. A prominent hysteresis loop can be observed in the $(\Delta R/R)_{xx}$-V_{piezo} and $(\Delta R/R)_{yy}$-V_{piezo} graphs, which closely resembles the hysteresis loops in the strain signals.

Figure 2.7**c** represents the N *vs.* $(\varepsilon_{xx}–\varepsilon_{yy})$ plot for a CsV_3Sb_5 single crystal. It can be seen that the N signal is linear to $(\varepsilon_{xx}–\varepsilon_{yy})$ across the entire strain range studied, as demonstrated in the representative temperature plots of 36 K, 60 K, 90 K, 94 K, and 100 K. The linear response of N to the $(\varepsilon_{xx}–\varepsilon_{yy})$ signals enables the determination of $\tilde{n} = dN/d(\varepsilon_{xx}–\varepsilon_{yy})$ in the zero strain limit for various tempertatures in CsV_3Sb_5. Figure 2.7**d** represents the corresponding nematic susceptibility $\tilde{n} = dN/d(\varepsilon_{xx}–\varepsilon_{yy})$ vs. T plot for CsV_3Sb_5. A more detailed analysis of the the nematic susceptibility in CsV_3Sb_5 will be discussed in Chapter 3.

In general, nematic susceptibility is defined by measuring the $dN/d(\varepsilon_{xx}–\varepsilon_{yy})$ value in the zero strain limit of $(\varepsilon_{xx}–\varepsilon_{yy}) \rightarrow 0$. However, in realistic conditions, differential thermal contraction of the piezo stack and the sample can in principle lead to a nonzero applied strain $(\varepsilon_{xx}–\varepsilon_{yy}) \neq 0$ even when zero voltage is applied to the stack. Therefore, it needs to be experimentally verified whether the 'actual zero strain point' for each measured temperature is within the dynamic measurement range of the piezo stack.

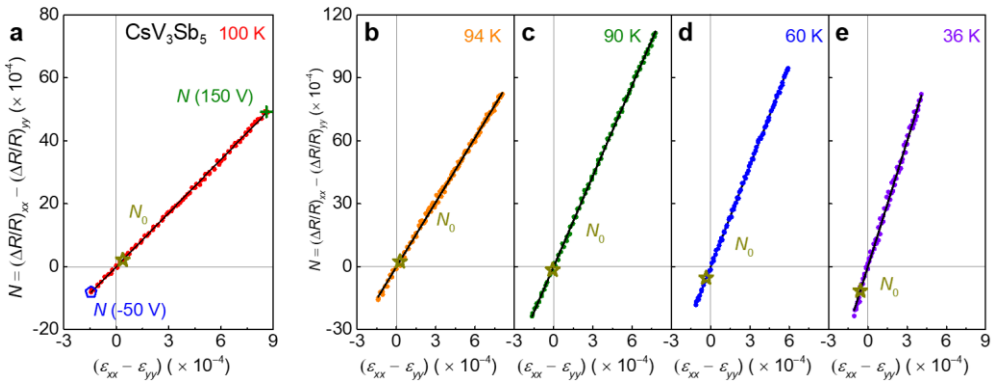

Figure 2.8 (**a**) $N = (\Delta R/R)_{xx} - (\Delta R/R)_{yy}$ *vs.* $(\varepsilon_{xx}–\varepsilon_{yy})$ plot of CsV_3Sb_5 at 100 K. A black solid line represents the best fitting result for the linear dependence of $N = \alpha \times (\varepsilon_{xx} – \varepsilon_{yy})$. The yellow star indicates N_0, which is the zero strain value for N. The blue octagon and the green cross indicates the strained N values $N(V_{piezo} = -50V)$ and $N(V_{piezo} = 150V)$, respectively. (**b**)-(**e**) N vs. $(\varepsilon_{xx}–\varepsilon_{yy})$ plots of CsV_3Sb_5 at 94 K, 90 K, 60 K, 36 K, respectively. The yellow stars indicate the N_0 values for each temperature.

In order to determine the 'actual zero strain point' for each temperature, the temperature dependence of the zero strain resistance $R_0(T)$ has been experimentally obtained by measuring the resistance of a free-standing crystal, unstrained and unattached to any substrate. As this R_0 represents the resistance value of the 'actual zero strain point' for each temperature, comparing the R_0 to the strained R values, namely R(V =150V) and R(V = -50V), would provide information of whether the 'zero strain point' is within the dynamic piezo stack range.

To investigate this feature, Figure 2.7**c** is replotted in Figure 2.8, which shows the anisotropic resistivity response upon applied anisotropic strain for various temperatures. Here, we note that experimental values of $(\Delta R/R)$ has been obtained by $(\Delta R/R) = \{(R(V) – R(V=0))/R_0\}$, following the approach of H.

–H. Kuo *et al.* [24]. It could be seen in Figure 2.8 that the zero strain N value $N_0 = \{(R_{xx,0} - R_{xx}(V=0))/R_{xx,0} - (R_{yy,0} - R_{yy}(V=0))/ R_{yy,0}\}$, indicated by the yellow stars is within the dynamic range between $N(V=-50V)$ and $N(150V)$ for the representative temperatures of 100 K, 94 K, 90 K, 60 K, and 36 K. These results confirm that 'actual zero strain point' of CsV_3Sb_5 is indeed within the dynamic measurement range of the piezo stack for all temperatures studied.

2.4 Diamond anvil cell measurement

The application of pressure has recently emerged as a popular method for introducing non-thermal tuning parameters to materials without causing disorder. Diamond anvil cells (DACs), which utilize diamonds, the hardest known material on Earth, as pressure anvils, are at the forefront of this research. These cells function by placing a sample between two diamonds and applying pressure. As indicated by the general formula Pressure = Force/Area, a small area is crucial for achieving high pressure. Thus, when the surface of the diamond anvil is compressed to a diameter of approximately 50 micrometers, it can apply around 400 GPa [25]. Considering that the Earth's core pressure is about 350 GPa, this signifies that an impressively high level of pressure can be applied at a laboratory scale using this technique.

Furthermore, the diamond anvils are optically transparent over a wide range of wavelengths, covering various wavelengths such as visible light, ultraviolet, and infrared light. This feature enables the diamond anvil cell for various spectroscopic and optical measurements techniques at high pressure,

such as X-ray diffraction, Raman, and photoluminescence measurements. This allows for the investigation of both structural and vibrational properties under high pressure.

Figure 2.9**a** shows a photograph of a diamond anvil cell along with a schematic illustration of a typical resistivity measurement scheme. The sample is placed between the diamond anvils, with the precise in-situ pressure determined by a ruby manometer located near the sample (indicated by the red dot). The in-situ calibration of pressure within a diamond anvil cell is ascertained through the peak shift of the ruby photoluminescence signal [26].

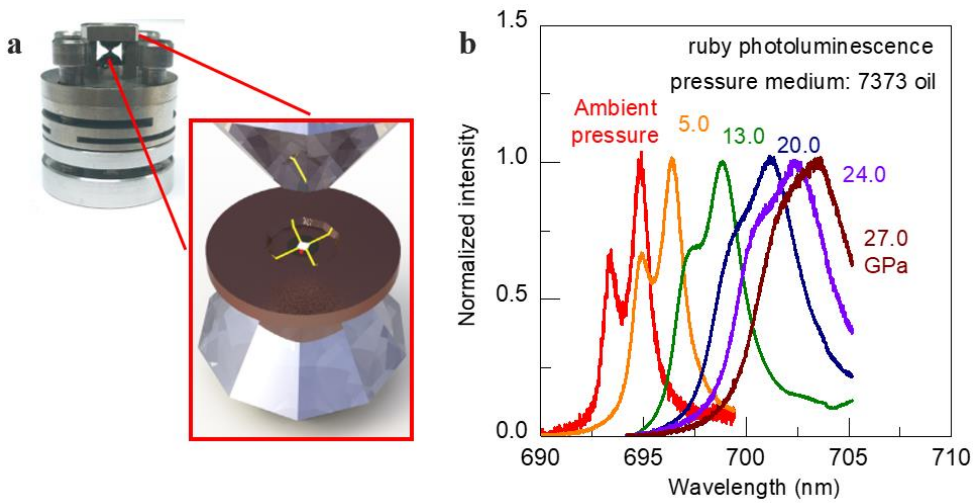

Figure 2.9 (**a**) A photograph of a diamond anvil cell in Prof. Kee Hoon Kim's lab. The inset in red is a cartoon figure of a typical resistivity measurement scheme. The brown metal plate indicates the pressure gasket, while the inner white square represents the sample. The yellow line represents the platinum contact leads and the red dot represents the ruby pressure manometer. (**b**) The normalized intensity-wavelength graph of ruby photoluminescence signals at various pressures using a Daphne 7373 oil as a pressure medium.

Figure 2.9**b** displays a graph of the normalized intensity-wavelength for ruby photoluminescence signals at various pressures. At ambient pressure, the photoluminescence of ruby exhibits two peaks, peak 1 near 693.2 nm and peak 2 near 694.22 nm. As pressure is applied to the ruby, these two peaks shift to higher wavelengths at a known rate relative to the pressure. The pressure is calibrated using the peak position of the peak 2, employing the formula $P(\text{GPa}) = A/B[\{1+\Delta\lambda/\lambda_0\}^B-1]$, where A = 19.04 MPa, B = 7.665, λ_0 = 694.22 nm, and $\Delta\lambda$ represents the shift in wavelength [26]. Figure 2.9**b** illustrates the measured normalized intensity-wavelength graphs of ruby at various pressures. A clear wavelength shift of the ruby photoluminescence peak can be observed with increased pressure, demonstrating the role of ruby as an excellent pressure manometer.

2.4.1 Diamond anvil cell Raman measurement

Raman spectroscopy is a powerful tool to study the vibrational modes of the various atoms in the crystal lattice. A Raman scattering involves two photons, one in and one out. In the Raman effect, a photon is scattered inelastically by a crystal, with either the creation or an annihilation of a phonon or a magnon. If a phonon or a magnon is created with the interaction with light, this effect is called the Stokes effect. Inversely, if a phonon is annihilated with the interaction with light, this effect is called the anti-Stokes effect [27]. As diamond is transparent to light near the visible wavelength range, a Raman measurement using a visible light as a laser source can be an

excellect probe to investigate the vibrational properties of a crystal lattice at high pressure.

Figure 2.10**a** presents a photograph of a Raman spectrometer measuring a Raman spectrum in a lab-made diamond anvil cell in Prof. Kee Hoon Kim's lab. Light is illuminated through the upper diamond and reflected on the sample surface, resulting in a combined Raman spectrum of the upper diamond and the sample under investigation. Figure 2.10**b** shows the Raman spectra of the upper diamond, which has been custom-made with low impurity standards to faciliate Raman measurements. It can be seen that the diamond exhibits only one sharp Raman peak in the range of 0-1400 cm^{-1}, providing a large transparent Raman window of 0-1300 cm^{-1} available for the sample.

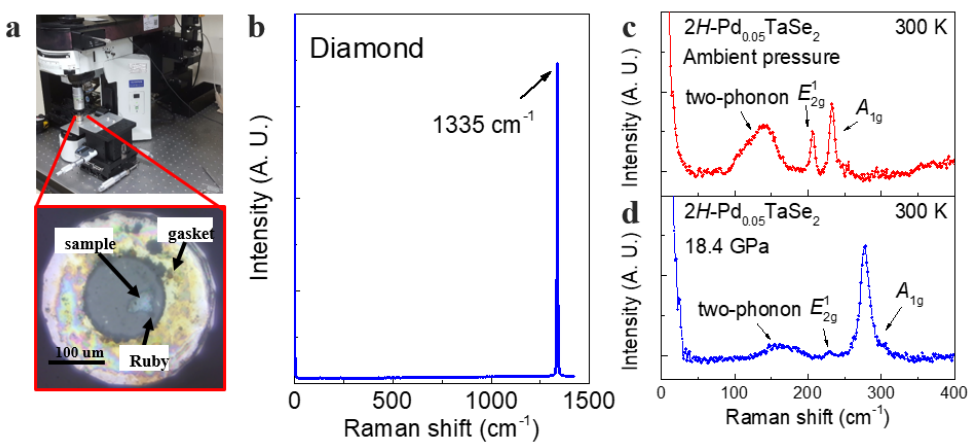

Figure 2.10 (**a**) A photograph of a Raman spectrometer (Nanobase, XperRam200^{TM}) measuring a Raman spectrum NiCrAl-based diamond anvil cell in Prof. Kee Hoon Kim's lab. The inset in red shows the sample space illuminated from the top through the upper diamond. The sample and the ruby are clearly visible inside a stainless steel gasket. Here, NaCl is used as a pressure-transmitting medium. The black scale bar indicates a 300 μm length.

(**b**) The intensity-Raman shift graph for a diamond. (**c**)-(**d**) The 300 K Raman spectra for a 2*H*-$Pd_{0.05}TaSe_2$ single crystal measured at (**c**) ambient pressure and at (**d**) 18.4 GPa pressure under a diamond anvil.

Figure 2.10**c-d** shows the 300 K Raman spectra for a 2*H*-$Pd_{0.05}TaSe_2$ single crystal measured at ambient pressure (Figure 2.10**c**) and at 18.4 GPa pressure (Figure 2.10**d**). It can be seen that the three Raman peaks visible in the measured Raman spectra shifts to higher values with applied pressure. This behavior can be understood by the hardening of the phonon modes as the lattice is compressed under pressure, and supports that the Raman measurements can probe the in-situ phonon vibrations of the crystal under pressure.

2.4.2 Diamond anvil cell transport measurement

Pressure is a clean tuning parameter to manipulate the electronic properties of the crystal by shortening bond distances and modifying the electronic bandwidth. This effect can affect the electronic correlations as well as the superconducting pairing strengths for superconducting materials. These changes in the electronic properties can be probed by measuring transport measurements at high pressure, which can offer useful information on the underlying mechanisms of various emergent orders [28]. In this chapter, the experimental details for measuring resistance and Hall effect using the van der Pauw method at high pressures will be introduced. In particular, a transport measurement scheme using a liquid pressure transmitting medium inside the diamond anvil cell will be discussed.

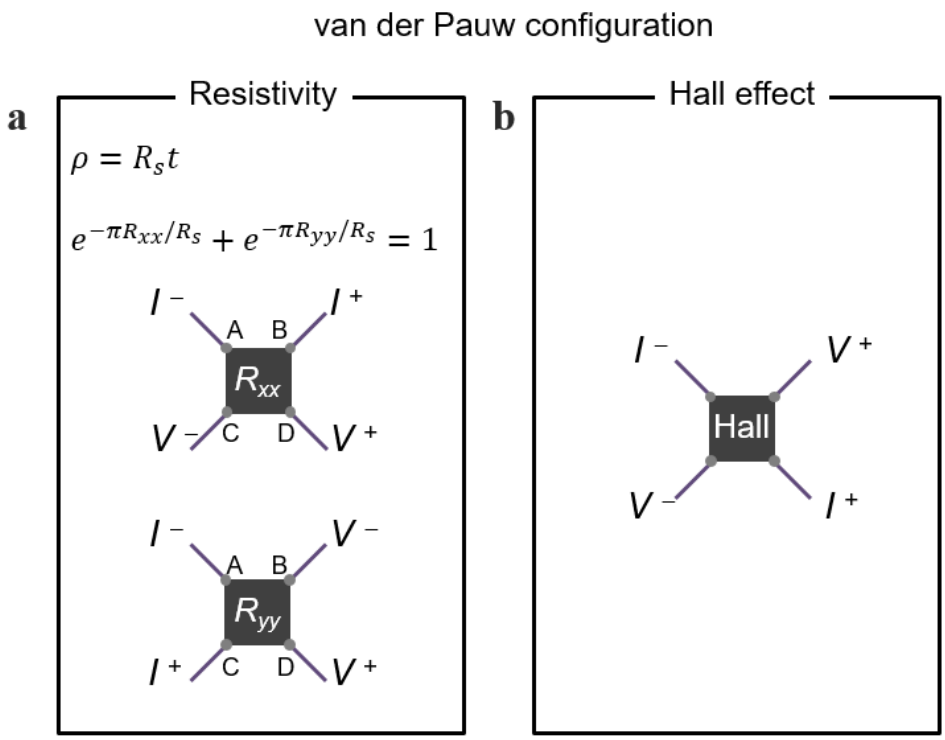

Figure 2.11 (**a**) A schematic figure of a resistivity measurement scheme in the van der Pauw configuration. The resistivity ρ can be calculated by the sheet resistance R_s and the thickness t, while R_s can be calculated by the two independent resistance measurements R_{xx} and R_{yy}. (**b**) A schematic figure of a Hall effect measurement scheme in the van der Pauw configuration.

The van der Pauw method is a method to measure the resistivity and the Hall coefficient of a sample that is approximately two-dimensional and solid with no holes, with the electrodes are placed on its edges. This method allows the determination of the average resistivity value of a sample, whereas a conventional four-probe method detects the resistivity in the current direction. Figure 2.11**a** shows a schematic figure of a resistivity measurement scheme in the van der Pauw configuration. The average resistivity of a sample can be calculated by multiplying the sheet resistance R_s and the thickness t, while R_s

can be calculated by measuring R_{xx} and R_{yy} and applying the equation $e^{-\pi R_{xx}/R_s} + e^{-\pi R_{yy}/R_s} = 1$ [29]. The Hall resistance in the van der Pauw scheme can be obtained by calculating the voltage-to-curent ratio, where the voltage is measured in the diagonal direction and the current is applied perpendicular to the voltage, as illustrated in Figure 2.11**b**.

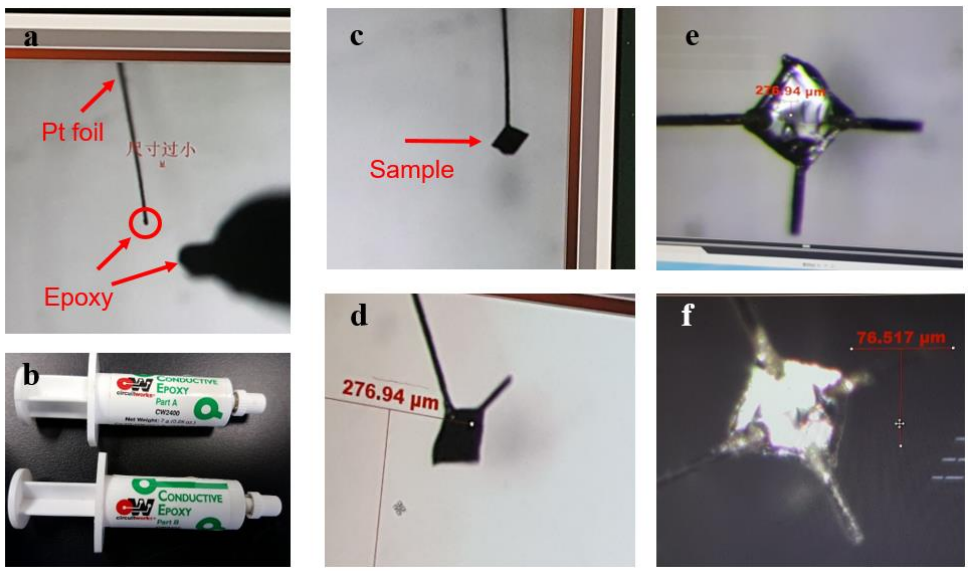

Figure 2.12 (**a**) A photograph of a razor-slices Pt foil line supported by Kapton tape. (**b**) An image of a room-temperature curable conductive silver epoxy set (Circuitworks CW2400). (**c**)-(**f**) Photographs of a lead-fabrication process for creating van der Pauw contacts.

For successful measurements using van der Pauw method on the 300 µm culet diamonds, it is necessary to create small contacts of approximately 100 µm in size. Figure 2.12 shows the experimental method to make small van der Pauw contacts on a crystal with the size of ~100 µm. The following steps describe the process of creating such contacts:

Begin by cutting the sample into a square shape, with a diagonal

distance of 100 µm. To move the sample, touch it with a very sharp wooden toothpick, allowing it to adhere to the toothpick due to van der Waals forces. Prepare a 5 µm thick Pt foil and cut it to a width of 10 µm. Use Kapton tape to attach the Pt foil to a glass slide, as illustrated in Figure 2.12**a**. Mix conducting epoxy (Circuitworks CW2400, Figure 2.12**b**) in a 1:1 mass ratio. Apply the epoxy onto the Pt foil using a sharpened toothpick. Attach the sample to the epoxy-coated Pt foil (Figure 2.12**c**). Cure the slide glass on a hot plate for 30 minutes at 100℃ to ensure conductivity and adhesion between the Pt foil and the sample. Trim the Pt foil to a length of 100 µm and repeat the process for all four sides, as shown in Figure 2.12**d-f**.

After creating the sample contacts, the sample should be loaded inside a prepared metal gasket for actual resistivity measurements. For target pressures of approximately 60 GPa, a stainless steel (SUS 304) gasket should be prepared. The following steps describe the process of making such a gasket:

To make a gasket, we require a piece of stainless steel with a thickness of 180 µm. Initially, to prepare the sample space, we must pre-indent the steel gasket with 300 µm culet diamonds by hand, resulting in applied pressure of approximately 1 GPa. Since a thin sample space of ~ 40 µm is required for actual sample measurement, preindenting the gasket to ~ 20 GPa pressure is necessary to reduce the gasket thickness before drilling a hole for the sample space. To calibrate the 20 GPa pressure, we insert a small ruby powder in the center of the hand-indented sus gasket. Using the photoluminescence signal of the ruby, we can pre-indent the gasket until 20 GPa pressure is reached. It is

crucial not to exceed 30 GPa, as doing so can make the gasket thickness below 40 μm, causing the diamond to touch each other and break.

Once the desired pressure is reached, we must wait for the pressure to stabilize for 30 minutes. Next, we should align the gasket on the gasket drilling machine and cut 280 μm of the 300 μm to make a hole for the sample space and the insulating *c*-BN material. Then, we mix the *c*-BN with insulating A, B epoxy, and cut a small amount of *c*-BN for use. We put the *c*-BN between the diamonds and inside the drilled hole, squeezing it inside firmly. Adding some ruby powder and pressing again up to 20GPa is necessary. After pressurization, we wait for another 30 minutes. We then drill a 120 μm hole on the c-BN and measure the gasket thickness using a conventional Vernier caliper.

If the thickness is more than 40 μm, we must repeat the process. To do so, we pressurize the gasket again, put the ruby in the center, and pressurize up to 20 GPa, waiting for another 30 minutes. The optimal thickness should be between 30 μm and 40 μm. If the thickness is too thick, the gasket will collapse into the sample space during actual measurements. Finally, we need to make a Pt foil of less than 40 μm using a Pt foil of thickness 5 μm and load the wires on the gasket with silver paste (Dupont 4929N), assuming all the procedures are done correctly.

After preparing the gasket, the sample should be carefully loaded into the prepared gasket. Place the sample inside, beneath the Pt wire. Once the sample wires are positioned beneath the Pt, press the piston/cylinder to prevent

the wires from moving. Finally, apply silicon oil and ruby powder before clamping the cell. Figure 2.13**a**-**b** shows the sample before loading (Figure 2.13**a)** and after loading in the diamond anvil cell (Figure 2.13**b**). Figure 2.13**c** shows a cartoon figure of a typical van der Pauw measurement scheme inside a diamond anvil cell. Figure 2.13**d** shows A photo of a diamond anvil cell with the wires loaded in a puck, prepared for measurement in a Physical Property Measurement System (PPMS^{TM}) in Prof. Kee Hoon Kim's lab.

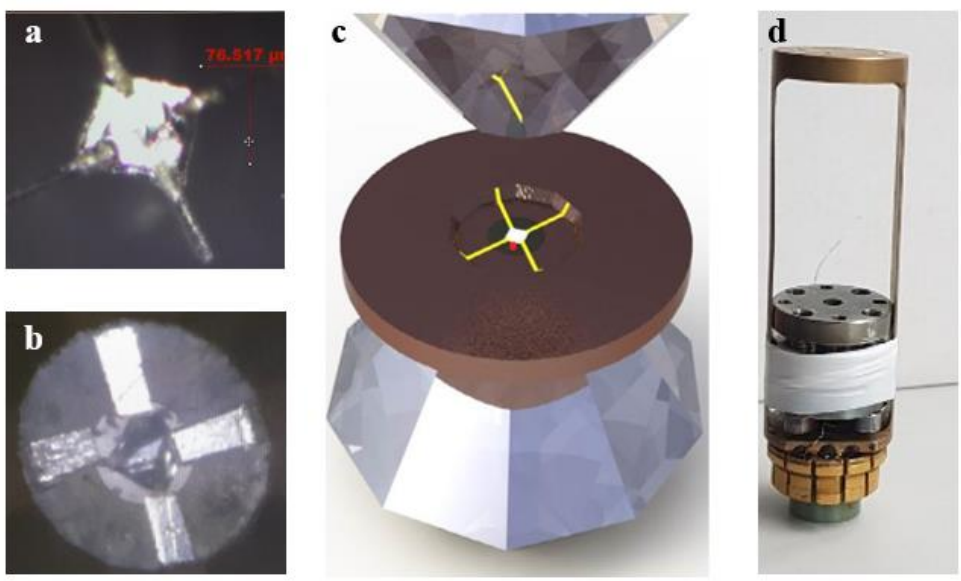

Figure 2.13 (**a**) A photograph of a crystal with van der Pauw contacts attached to the edges. (**b**) A photograph of a contacted sample loaded inside a prepared stainless steel gasket. (**c**) An illustrated representation of a typical van der Pauw measurement setup inside a diamond anvil cell. (**d**) A photograph of a diamond anvil cell with the wires loaded in a puck, prepared for measurement in a Physical Property Measurement System (PPMS^{TM}) in Prof. Kee Hoon Kim's lab.

Chapter 3 Optimized superconductivity in the vicinity of a nematic quantum critical point in the kagome superconductor $Cs(V_{1-x}Ti_x)_3Sb_5$

3.1 Overview

In recent years, metals featuring kagome lattice structures have attracted considerable attention due to their distinct electronic structure, which hosts Dirac points, flat bands, and saddle points in their crystal momentum space [13]. Specifically, the diverging density of states near the saddle points and flat bands have enabled the realization of intriguing many-body ground states, such as superconductivity [13-14], and chiral charge density wave order [13]. Among these materials, the recently discovered vanadium-based kagome metals AV_3Sb_5 (A = K, Rb, and Cs) have been most actively studied due to various electronic instabilities arising from van Hove singularities near the Fermi level. For example, each member of this family exhibits 2 × 2 charge order below their charge ordering temperatures (T_{CDW}'s = 80–104 K) and the coexistence of superconductivity [17]. Notably, the Cs variant of this compound has been found to host additional electronic orders, such as 2 × 2 × 2 and 2 × 2 × 4 out-of-plane direction CDW modulations [17], and electronic nematic order [18].

However, despite intense experimental efforts, the superconducting properties of CsV_3Sb_5 are still far from fully understood. One significant

puzzle, related to the present study, concerns the origin of an elusive double-domed superconductivity found in the studies of Sn-doped polycrystals [30] and pressurized single crystals of CsV_3Sb_5 [31-32], whereas the KV_3Sb_5 and RbV_3Sb_5 counterparts only exhibit a single superconducting dome with external control parameters [33]. Closely related to the puzzle, a very recent study identified the presence of an electronic nematic phase in CsV_3Sb_5 [18], suggesting a possibility of interplay between nematic order and superconductivity. Elastoresistance measurements, which can directly probe nematic susceptibility, have been found to be quite useful in uncovering the pivotal role of nematic fluctuation in mediating Cooper pairing, particularly in several Fe-based superconductors [34-38]. Therefore, to understand the role of nematic order on superconductivity in CsV_3Sb_5, elastoresistance studies in high-quality single crystals as a function of doping are highly desirable.

In the current investigation, high-quality single crystals of $Cs(V_{1-x}Ti_x)_3Sb_5$ ($0 \leq x \leq 0.06$) have been successfully grown, with the accurate doping ratio and systematic lattice variation confirmed by wavelength-dispersive X-ray spectroscopy (WDS) and X-ray diffraction (XRD) measurements, respectively. Elastoresistance measurements are employed in relation to the Ti ratio x to probe the interplay between nematic order and superconductivity. A careful examination of $Cs(V_{1-x}Ti_x)_3Sb_5$ single crystals reveals a systematic suppression of the Curie-Weiss temperature θ_{nem} upon Ti doping, which changes its sign to become negative at $x \sim 0.009$, close to the critical doping of $x_c = 0.01$, where the Curie constant and nematic

susceptibility are found to reach their maximum values. This constitutes strong evidence of a nematic quantum critical point (NQCP) near x_c. Remarkably, the superconducting transition temperature and Meissner volume fraction exhibit an unusual double-dome feature as a function of x, with the center of the first dome located in the vicinity of the NQCP. These observations raise the intriguing possibility that fluctuations in the nematic order play an important role in the pairing interaction to optimize superconductivity in the first superconducting dome of $Cs(V_{1-x}Ti_x)_3Sb_5$. The findings will be discussed one by one in the following chapters.

3.2 Introduction

CsV_3Sb_5, one prominent member of the vanadium-based kagome metal, has been found to exhibit multiple electronic and structural orders which has been theoretically predicted in the kagome Hubbard model [17]. This compound is known to exhibit at least three phase transitions to various orders as the temperature is lowered: a charge order at T_{CDW} ~ 98 K [17], a nematic order at T_{nem} ~ 35 K [18], and a superconducting state at T_c ~ 3.2 K [17]. Figure 3.1**a** depicts the evolution of the vanadium kagome net in CsV_3Sb_5 as the phase transitions are exhibited upon lowering the temperautre. At room temperature (300 K), the vanadium atoms form a kagome structure. However, below the charge ordering temperature T_{CDW}, the structure is transformed into a tri-hexagonal arrangement, with distinctly shaped hexagons and triangles [39]. As the temperature is further reduced to 35 K, it exhibits an electronic

nematic state, characterized by a one-directional modulation in the electronic structure.

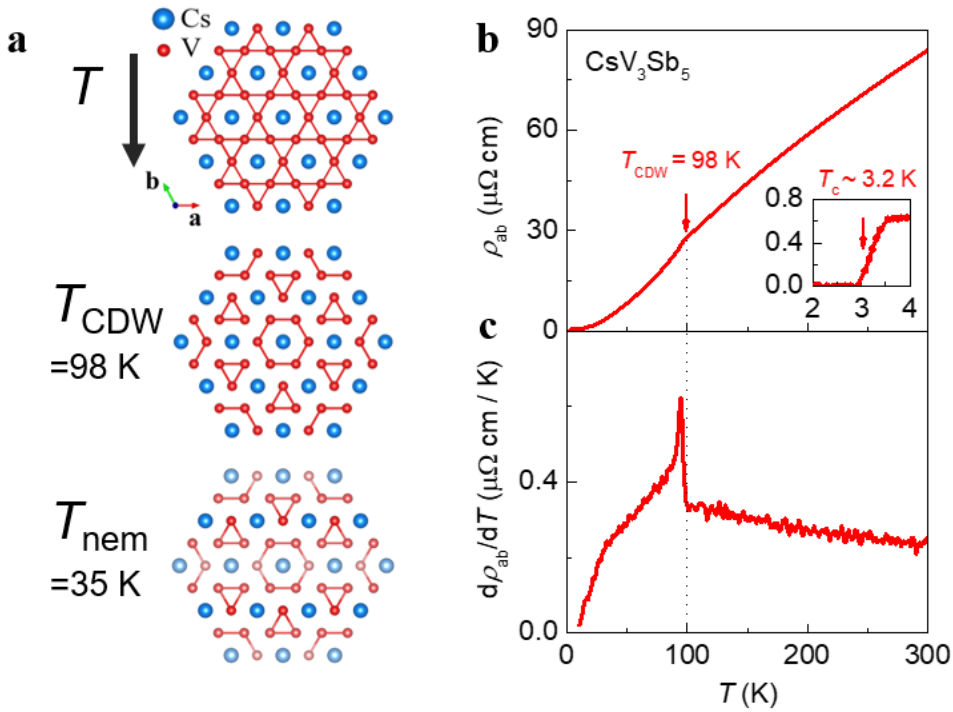

Figure 3.1 (**a**) A schematic figure of the temperature dependent evolutions due to the known phase transitions in the vanadium kagome net of CsV_3Sb_5. (**b**) The temperature dependence of the in-plane resistivity ρ_{ab} of CsV_3Sb_5. (inset) A low temperature plot of the temperature dependent in-plane resistivity ρ_{ab} (**b**) The temperature dependence of the derivative of the in-plane resistivity $d\rho_{ab}/dT$ of CsV_3Sb_5.

Figure 3.1**b** depicts the temperature dependence of the in-plane resistivity ρ_{ab} of CsV_3Sb_5. As temperature is lowered, an upturn in resistivity is observed indicating at the charge ordering temperature T_{CDW} of ~ 98 K. At low temperatures, the superconducting phenomenon of zero resistivity can also be observed near T_c ~ 3.2 K, as shown in the inset of Figure 3.1**b**. Figure 3.1**c**

shows the derivative of the in-plane resistivity $d\rho_{ab}/dT$ of CsV_3Sb_5. The precise charge ordering temperature T_{CDW} can be defined using the upturn in the $d\rho_{ab}/dT$ data.

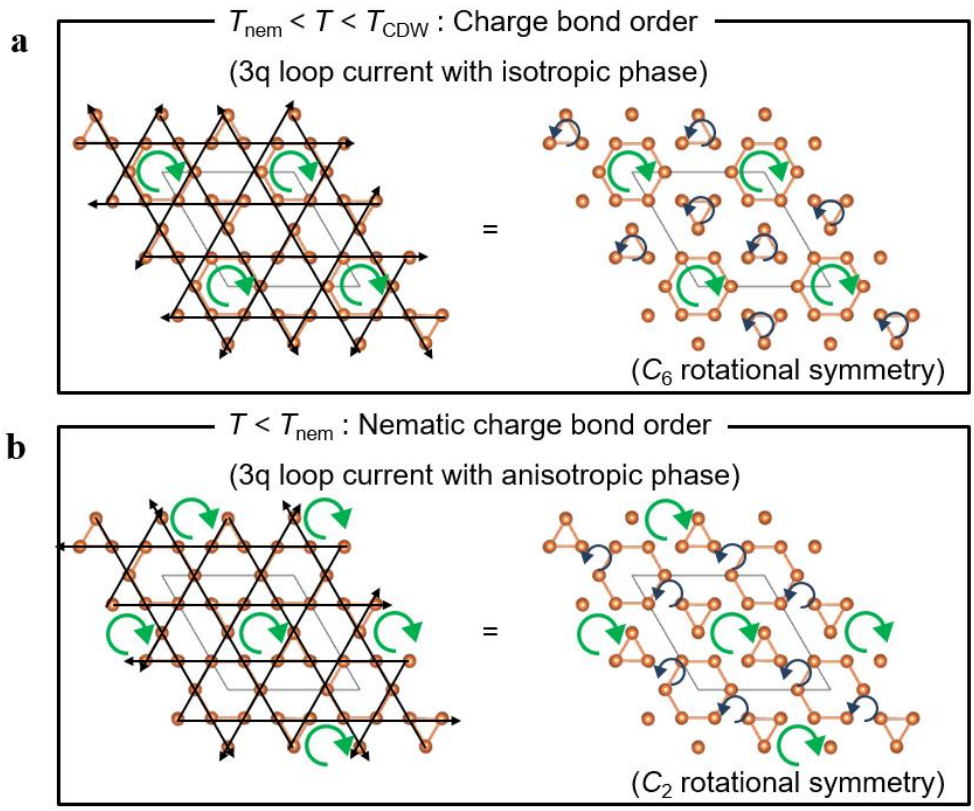

Figure 3.2 Schematic figures depicting the 3**q** charge loop currents of CsV_3Sb_5 (**a**) in the charge bond order state at $T_{nem} < T < T_{CDW}$ and (**b**) in the nematic charge bond order state at $T < T_{nem}$.

Interestingly, due to the extensive theoretical calculations available for this material, it is possible to achieve a deeper understanding of the observed charge order and nematic order [15, 40]. In this material, geometrical frustration due to the kagome structure is believed to generate small orbital currents, named the chiral loop currents. Theoretically, these chiral loop

currents exist in three different **q** vector directions with a 120 degree angle with respect to each other. Figure 3.2**a** shows a schematic figure of the 3**q** charge loop currents of the CsV3Sb5 at $T_{nem} < T < T_{CDW}$. At this temperature regime, the 3**q** charge loop currents exhibit the same amplitude as well as the same phase order parameters, which result in a chiral loop in one direction inside the hexagon structure and a chiral loop in the opposite direction in the triangular structures. This in turn preserves the intrinsic 6-fold rotational symmetry (C_6) as exhibited by the structure.

However, when one or two phases of the chiral loop current is changed, namely becomes the chiral loop current with anisotropic phase, the chiral loop translates a specific vector *a* along the lattice structure, resulting in a new phase with electronic rotational symmetry lowerring from sixfold (C_6) to twofold (C_2) with one-dimensional modulation. According to various theories [15, 40], these phenomena account for the charge order and nematic order in CsV_3Sb_5 and are referred to as charge bond order and nematic charge bond order in theoretical terms.

In this interesting system of CsV_3Sb_5, recent experiments have demonstrated that, with various control parameters such as applying pressure in the single crystal [31-32], or doping Sb with Sn in the polycrystals [30], the superconducting transition temperature exhibits a double-dome shape. This occurrence of the double-dome feature is exceptionally rare and not yet fully understood. Therefore, in this chapter, the superconducting properties, as well as the relation between superconductivity and other emergent orders in

CsV_3Sb_5 have been investigated. Specifically, I investigated the physical phenomena associated with doping the V site with Ti atoms, which can directly alter the kagome lattice and also provide hole doping.

3.3 Characterization of the Ti content in $Cs(V_{1-x}Ti_x)_3Sb_5$

To determine the elemental composition ratio in a sample, a wavelength dispersive spectroscopy (WDS) measurements can be performed, which enables the characterication of the elemental compositions in a non-destructive method. In order to determine the Cs, V, Ti, and Sb content in the lab-grown $Cs(V_{1-x}Ti_x)_3Sb_5$ single crystals, wavelength dispersive X-ray spectroscopy (WDS) was conducted using a field emission electron probe microanalyzer (JEOL Ltd., JXA-8530F), with V (99.99%), Ti (99.9%), and Sb (99.99%) metals as standard specimens. Due to the high air sensitivity of elemental Cs metal, the standard specimen data for Cs was obtained from the JEOL database.

Figure 3.3**a** shows a measured WDS raw data image of a $Cs_{1.01}(V_{0.973}Ti_{0.027})_3Sb_5$ single crystal, where the *x*-axis represents X-ray energy and the *y*-axis represents the X-ray intensity. It can be seen from the raw data that the X-ray signals from each of the Cs, V, Ti, and Sb elements are detected in the WDS spectra. Figure 3.3**b** displays a scanning electron microscope (SEM) image of a $Cs_{1.01}(V_{0.973}Ti_{0.027})_3Sb_5$ single crystal (top) and the the relative molar ratio of Cs, V, Ti, and Sb content of the same crystal (bottom). It is immediately apparent that the atomic ratio of V (~2.919) is lower than 3, while the sum of the atomic ratios of Ti and V is approximately equal to a

value of ~3. This indicates that upon doping, Ti atoms replace V atoms rather than occupying Cs or Sb sites.

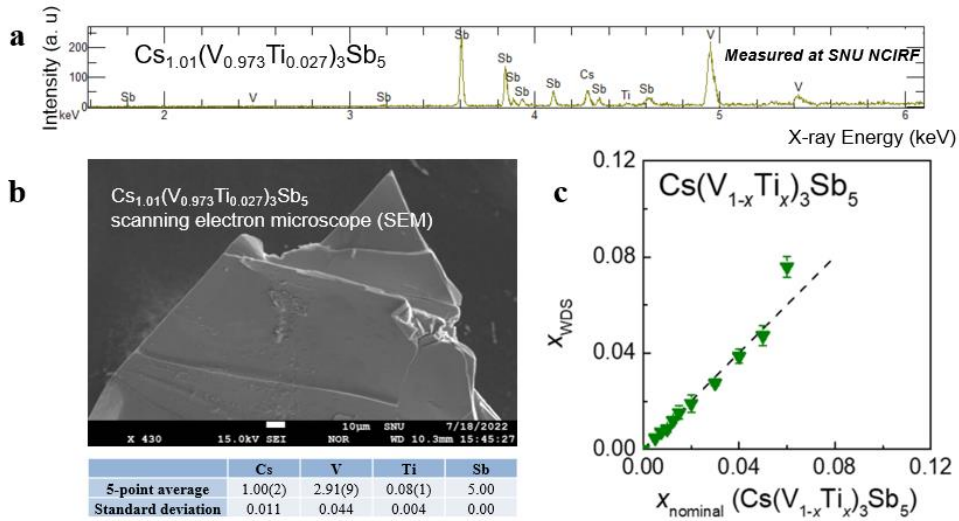

	Cs	V	Ti	Sb
5-point average	1.00(2)	2.91(9)	0.08(1)	5.00
Standard deviation	0.011	0.044	0.004	0.00

Figure 3.3 (**a**) The X-ray intensity *vs*. energy graph of a $Cs_{1.01}(V_{0.973}Ti_{0.027})_3Sb_5$ single crystal as measured in the field emission electron probe microanalyzer in NCIRF, Seoul National University. (**b**) (top) The scanning electron microscope image of a $Cs_{1.01}(V_{0.973}Ti_{0.027})_3Sb_5$ single crystal and (bottom) the relative molar ratio of Cs, V, Ti, and Sb content of $Cs_{1.01}(V_{0.973}Ti_{0.027})_3Sb_5$. (**c**) The actual Ti content x *vs*. nominal Ti content x of the grown $Cs(V_{1-x}Ti_x)_3Sb_5$ single crystals.

Figure 3.3**c** shows a plot of the actual V:Ti ratio ($x_{nominal}$) *vs*. the nominal V:Ti ratio (x_{WDS}) obtained from the WDS analysis. It can be observed that the actual V:Ti ratio closely follows the nominal V:Ti ratio, at least up to $x_{nominal} = 0.05$. For $x_{nominal} = 0.06$, the x_{WDS} exhibits a slight upward deviation from the linear guideline, indicating a higher doping ratio compared to the nominal value. It was confirmed that the actual Ti doping ratio closely follows the nominal value in the lab-grown $Cs(V_{1-x}Ti_x)_3Sb_5$ single crystals, at least up

to 5% Ti content.

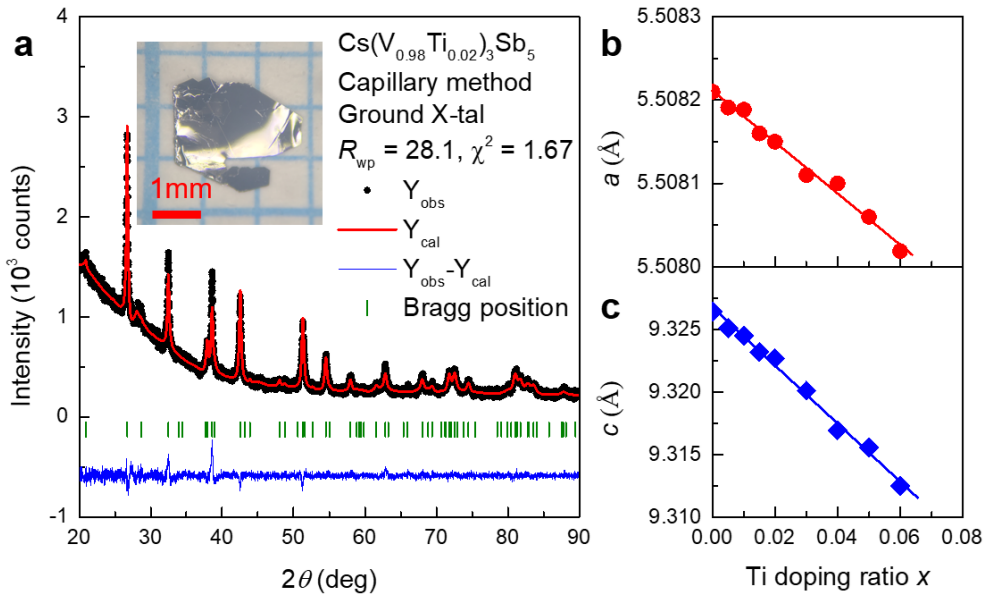

Figure 3.4 (**a**) Capillary x-ray diffraction patterns (black dots) and the corresponding Rietveld refinement result (red line) with R_{wp} = 28.1 and χ^2 = 1.67 of a $Cs(V_{0.98}Ti_{0.02})_3Sb_5$ single crystal. The subtracted patterns are shown as blue lines and the expected peak positions are shown as the green ticks. Inset shows a photograph of a $Cs(V_{0.98}Ti_{0.02})_3Sb_5$ single crystal placed on top of a graph paper with one unit of 1 mm (red scale bar). (**b**) and (**c**) show the evolution of *a* and *c* lattice parameters, respectively, with Ti doping ratio *x*.

To investigate the relationship between doping and lattice constants, the lab-grown $Cs(V_{1-x}Ti_x)_3Sb_5$ single crystals were ground and placed inside a quartz capillary tube with a 0.5 mm inner diameter. X-ray diffraction (XRD) θ-2θ scans were performed using a high-resolution X-ray diffractometer (PANalytical Empyrean). Figure 3.4**a** shows the XRD pattern for ground single crystals of $Cs(V_{0.98}Ti_{0.02})_3Sb_5$ (black dots) alongside the calculated Rietveld refinement result (red line) obtained using FullProf software. The refinement, which accounted the preferential orientation along the *c*-axis,

could successfully reproduced the XRD pattern, yielding an R_{wp} = 28.1 and χ^2 = 1.67. Similar analyses were also conducted for other doping values, resulting in R_{wp} values below 30 and χ^2 values below 2. Consequently, the refined *a* and *c* values were obtained, which is shown in Figures 3.4**b-c**. It could be seen that both *a* and *c* lattice parameters exhibit a decreasing trend as the Ti doping ratio *x* is increased. This effect can be attributed to the smaller ionic radii of Ti^{4+} ions (60.5 pm) as compared to V^{3+} ions (64 pm) and supports that Ti atoms substitute the V site upon doping.

3.4 Evolution of the CDW transition temperature

Figure 3.5**a** shows the in-plane resistivity ρ_{ab} of $Cs(V_{1-x}Ti_x)_3Sb_5$ normalized by the resistivity at 300 K ($\rho_{ab}/\rho_{ab,300\ K}$). The resistivity of the undoped CsV_3Sb_5 exhibits an upturn behavior near T_{CDW} ~ 98 K due to the development of the charge order. With increased Ti doping concentration *x*, the residual resistivity ratio (RRR) of $Cs(V_{1-x}Ti_x)_3Sb_5$ is systematically decreased. The RRR is a measure of the ratio of resistivity at low temperature to that at high temperature and is a key parameter for characterizing the quality of a material. A decrease in RRR indicates an increase in impurity scattering within the kagome plane, which can be attributed to the presence of Ti dopants. This result suggests that Ti doping introduces impurity states in the kagome lattice, leading to increased scattering of electrons and a reduction in electronic conductivity.

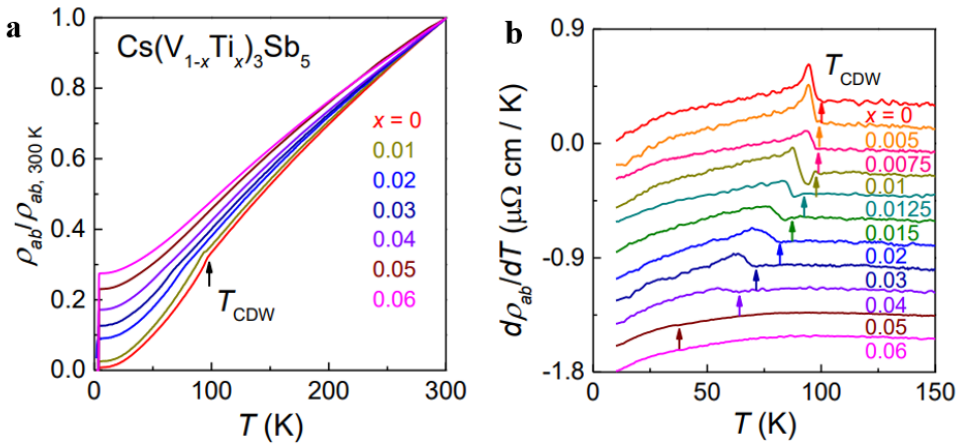

Figure 3.5 (**a**) Temperature dependence of the in-plane resistivity ρ_{ab} normalized by the resistivity value of $Cs(V_{1-x}Ti_x)_3Sb_5$ single crystals at 300 K for $0 \leq x \leq 0.06$. (**b**) $d\rho_{ab}/dT$ curves of $Cs(V_{1-x}Ti_x)_3Sb_5$ single crystals. The curves have been vertically shifted down for clarity. The colored arrows indicate the charge ordering temperature T_{CDW}.

Along with the decreased RRR value, $Cs(V_{1-x}Ti_x)_3Sb_5$ exhibits increasingly broadened CDW transitions with increasing x, which are well visualized in the $d\rho_{ab}/dT$ curves in Figure 3.5**b**. This suggests that the Ti dopants introduce disorder into the electronic structure of the kagome lattice, leading to a broadened formation of the CDW order. Furthermore, the anomalies in $d\rho_{ab}/dT$ shift to lower temperatures, indicating the development of a lower T_{CDW} at higher x, for example, ~ 59 K at $x = 0.04$. This indicates the weakening of CDW order as the vanadium kagome net is altered with Ti doping.

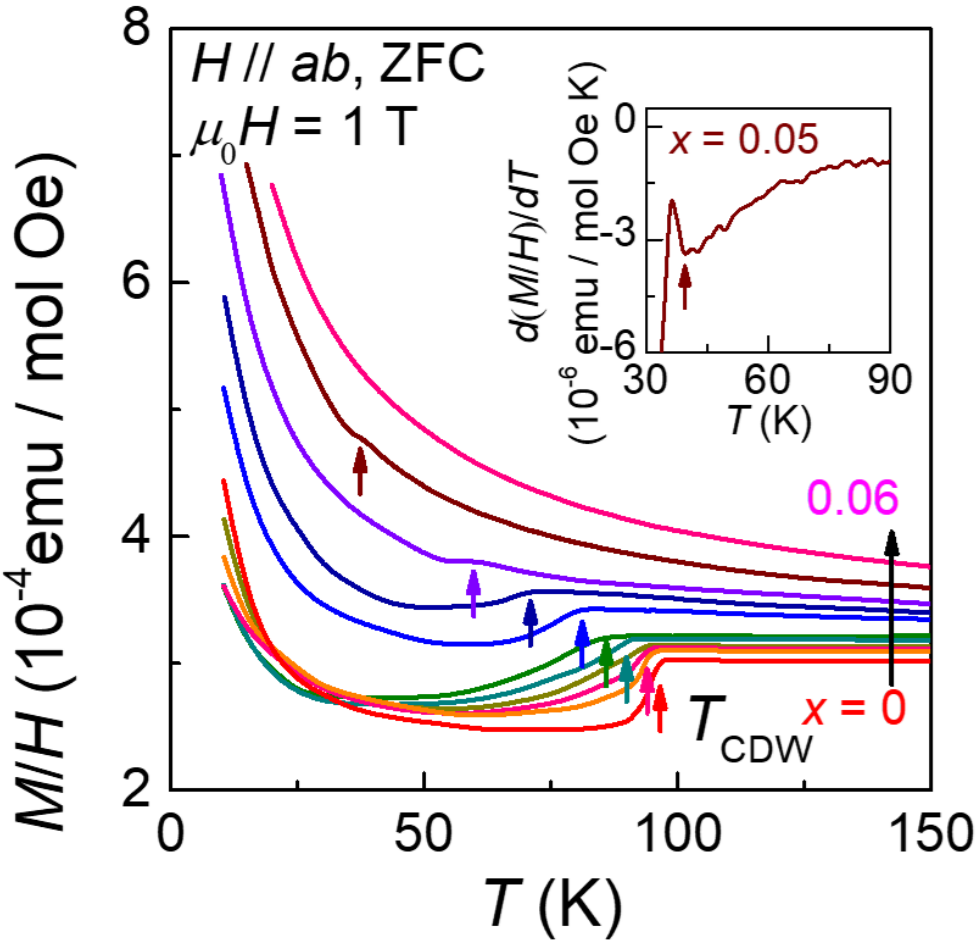

Figure 3.6 Temperature dependence of the M/H of the $Cs(V_{1-x}Ti_x)_3Sb_5$ single crystals measured at a constant external field of $\mu_0 H$ = 1 T after zero-field cooling (ZFC). Here, M indicates the magnetization and H indicates the magnetic field. The inset represents the temperature dependence of the $d(M/H)dT$ of $Cs(V_{0.95}Ti_{0.05})_3Sb_5$ near the charge ordering temperature T_{CDW}.

The trend of decreasing T_{CDW} is further supported by the dc magnetic susceptibility (M/H) data shown in Figure 3.6. According to the equation of Pauli Paramagnetism, $M/H = \mu_0 \mu_B g(E_F)$, where μ_0 is the vaccuum permeability, μ_B is the Bohr magneton, and $g(E_F)$ is the electron density of states [27]. The drop in the M/H curve observed in pristine CsV_3Sb_5, which is known as a Pauli

paramagnet, signifies a depletion of the density of states due to the CDW gap opening at T_{CDW} = 98 K. Consistent with the behavior observed in ρ_{ab}, increasing the Ti doping concentration results in a shift in T_{CDW} to lower temperatures. Furthermore, the charge ordering transition becomes decreased and broadened with increasing Ti doping concentration. This suggests that the Ti dopants systematically reduce the depletion of electronic density of states at the long-range CDW transition, leading to a decrease in the averaged T_{CDW} and an increase in the T_{CDW} distribution.

3.5 Evolution of the superconducting properties

As the systematic suppression of T_{CDW} has been established through Ti doping, we now shift our attention to the evolution of superconductivity and its interplay with the pre-existing CDW order. Figure 3.7 shows the temperature dependence of the in-plane resistivity ρ_{ab} and the temperature dependence of $4\pi\chi$ data of $Cs(V_{1-x}Ti_x)_3Sb_5$ single crystals. The superconducting transition temperature (T_c) is determined by the 50% criteria of the normal-state resistivity in the in-plane resistivity ρ_{ab} data.

Notably, it is found that the superconducting transition temperature T_c exhibits a non-monotonic behavior with increased Ti doping concentration. At x = 0.0075, a maximum value of T_c is found at 4.1 K, which is ~ 1K higher than the T_c = 3.2 K of the pristine CsV_3Sb_5. Moreover, in the doping range of x = 0.0-0.01, a full Meissner shielding of $-4\pi\chi \approx 1$ is exhibited, which can be seen in Figure 3.7**c**. However, with a further increase in Ti doping

concentration towards x = 0.02, T_c is progressively suppressed to ~1.9 K (Figure 3.7**a**-**b**), followed by a decreased Meissner shielding fraction of $-4\pi\chi \sim 0.3$ at x = 0.015 and $-4\pi\chi \sim 0$ around x = 0.02. Above $x > 0.02$, T_c increases again to exhibit a second maximum value of 3.8 K at x = 0.05 and recovers the full Meissner shielding of $-4\pi\chi \sim 1$. Therefore, the evolution of the superconducting properties, the superconducting transition temperature T_c and the Meissner shielding $-4\pi\chi$ is found to reveal a double-dome feature upon Ti doping x.

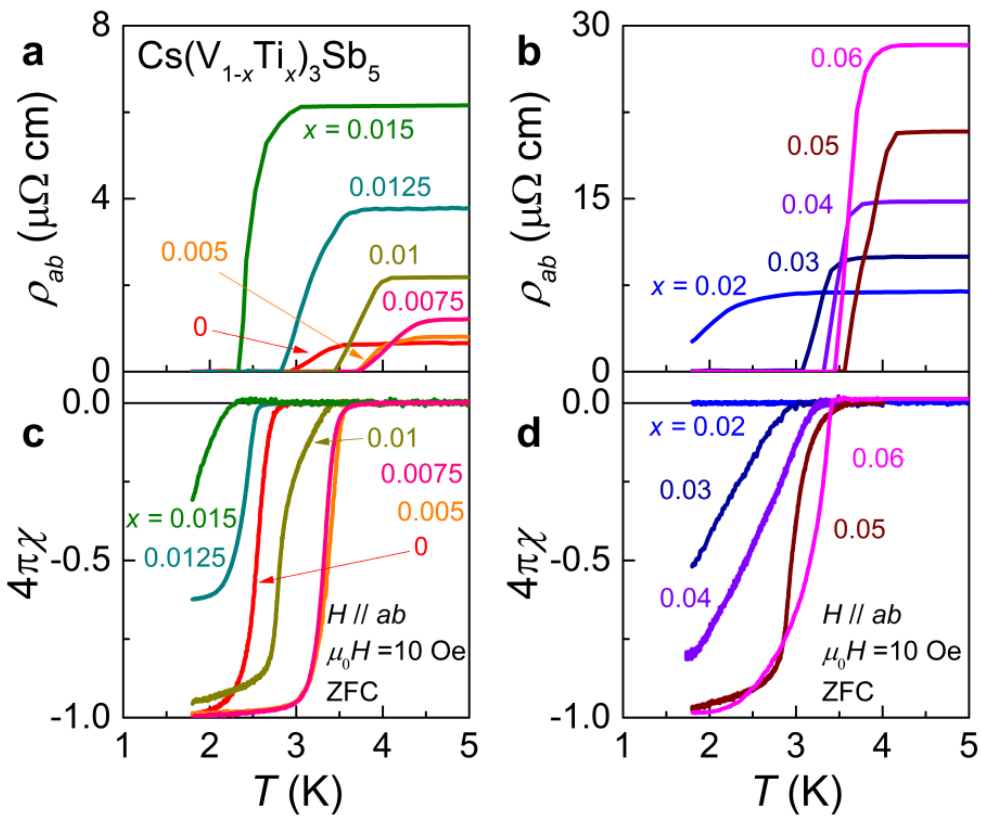

Figure 3.7 Low-temperature behaviour of the in-plane resistivity ρ_{ab} in $Cs(V_{1-x}Ti_x)_3Sb_5$ for (**a**) $0 \leq x \leq 0.015$ and (**b**) $0.02 \leq x \leq 0.06$. Temperature dependence of $4\pi\chi$ (χ: magnetic susceptibility) measured at $\mu_0 H$ = 10 Oe after

zero field cooling (ZFC) for (**c**) $0 \leq x \leq 0.015$ and (**d**) $0.02 \leq x \leq 0.06$.

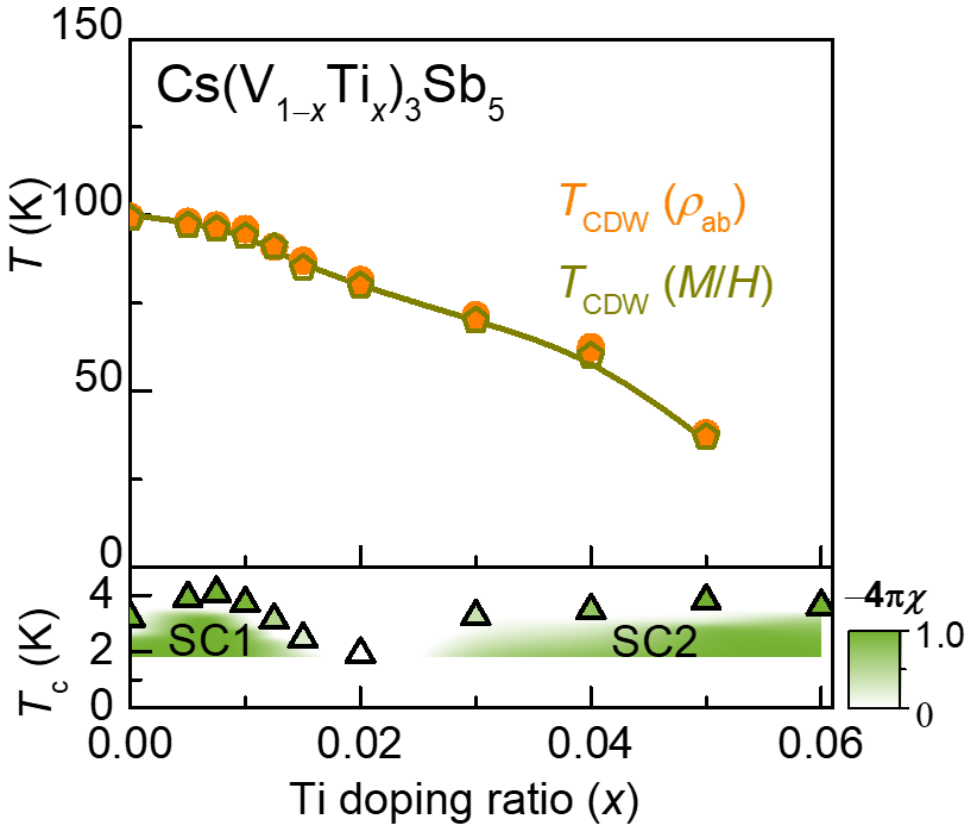

Figure 3.8 A temperature(T)-doping(x) phase diagram of $Cs(V_{1-x}Ti_x)_3Sb_5$, indicating the charge ordering temperatures T_{CDW} and the superconducting transition temperatures T_c. The orange circles and the yellow octagons indicate the T_{CDW} obtained by the ρ_{ab} and M/H measurements. The green triangles indicate the superconducting transition temperature T_c defined by the 50% criteria of the normal-state resistivity values. The green color contour indicates the Meissner volume fraction ($-4\pi\chi$).

Figure 3.8 represents the temperature-doping phase diagram of $Cs(V_{1-x}Ti_x)_3Sb_5$, obtained by analysis of the charge ordering temperatures T_{CDW}s and the superconducting transition temperatures T_cs. It can be seen that a double superconducting dome is clearly exhibited, with the whole first

superconducting region (SC1) found within the charge order and the second superconducting region (SC2) found near the suppression point of the charge ordering temperature T_{CDW}. While the SC2 can be understood as a superconductivity dome stabilized at a putative CDW quantum critical point (QCP) [41], the emergence of another superconducting dome within the CDW order is indeed a rare finding within the CDW bearing materials. This strongly suggests that additional fluctuating orders could be present to enhance the superconducting pairing interaction near the first superconducting region (SC1).

3.6 Evolution of the nematic order: elastoresistance

To investigate the origin of the unusual trend in T_c, the elastoresistance in $Cs(V_{1-x}Ti_x)_3Sb_5$ was investigated. Figure 3.9**a** illustrates the experimental configuration for the elastoresistance measurements. It is known that the nematic susceptibility $\tilde{n}$ can be obtained by measuring the electronic anisotropy induced by anisotropic strain. In other words, $\tilde{n}$ becomes linearly proportional to the anisotropic change in the resistance $N \equiv (\Delta R/R)_{xx} - (\Delta R/R)_{yy}$ in response to anisotropic strain $(\varepsilon_{xx}-\varepsilon_{yy})$, which results in $\tilde{n} = dN/d(\varepsilon_{xx}-\varepsilon_{yy})$.

Before analysing the nematic susceptibility signals, it is essential to comprehend two fundamental properties related to the crystal under study. The first property concerns the allowed symmetry channels in nematic susceptibility that the sample can exhibit, while the second is related to the exact symmetry channel that

$\tilde{n} = dN/d(\varepsilon_{xx}-\varepsilon_{yy})$ measures. This information depends on the specific space group of the crystal being studied and the definition of the *x*-cartesian axis in respect to the crystal axis.

Particularly, for a crystal in the D_{6h} point group such as CsV_3Sb_5 with *x* along the [100] axis, the elastoresistance tensor m_{ij} in the absence of magnetic field can be expressed as

$$m_{ij}^{D6h} = \begin{pmatrix} m_{11} & m_{12} & m_{13} & 0 & 0 & 0 \\ m_{12} & m_{11} & m_{13} & 0 & 0 & 0 \\ m_{13} & m_{13} & m_{33} & 0 & 0 & 0 \\ 0 & 0 & 0 & m_{44} & 0 & 0 \\ 0 & 0 & 0 & 0 & m_{44} & 0 \\ 0 & 0 & 0 & 0 & 0 & (m_{11}-m_{12})/2 \end{pmatrix},$$

according to the general definition of elastoresistance coefficients $(\Delta R/R)_i \equiv \Sigma^6_{j=1} m_{ij}\varepsilon_j$ [18]. Here, ε_j represents the engineering strain m_{ij} represents the elastoresistance tensor components, and the subscripts *i* and *j* represent the Voigt notation (1 = *xx*, 2 = *yy*, 3 = *zz*, 4 = *yz*, 5 = *zx*, 6 = *xy*). According to this definition, $\tilde{n} = dN/d(\varepsilon_{xx}-\varepsilon_{yy})$ can be expressed in terms of m_{ij}. By substituting m_{ij}^{D6h} into the definition of the elastoresistance coefficient, one can obtain the following two equations,

$$\left(\frac{\Delta R}{R}\right)_{xx} = m_{11}\varepsilon_{xx} + m_{12}\varepsilon_{yy} + m_{13}\varepsilon_{zz}$$
$$\left(\frac{\Delta R}{R}\right)_{yy} = m_{12}\varepsilon_{xx} + m_{11}\varepsilon_{yy} + m_{13}\varepsilon_{zz}.$$

The subtraction of these two equations results in the following expression $(m_{11}-m_{12}) = \{(\Delta R/R)_{xx} - (\Delta R/R)_{yy}\}/(\varepsilon_{xx}-\varepsilon_{yy})$, which becomes $dN/d(\varepsilon_{xx}-\varepsilon_{yy})$ in the small strain limit of $(\varepsilon_{xx}-\varepsilon_{yy}) \rightarrow 0$.

Moreover, according to the irreducible representations of the D_{6h} point group, any arbitrary strain in the hexagonal lattice can be divided into the three strain components [18], $\varepsilon_{A1g} = (1/2(\varepsilon_{xx}+\varepsilon_{yy}), \varepsilon_{zz})$, $\varepsilon_{E1g} = (\varepsilon_{xz}, \varepsilon_{yz})$, and $\varepsilon_{E2g} = (1/2(\varepsilon_{xx}-\varepsilon_{yy}), \varepsilon_{xy})$. As the elastoresistance (m_{11}–m_{12}) represents the nematic susceptibility induced by (ε_{xx}–ε_{yy}) strain, (m_{11}–m_{12}) represents the nematic susceptibility along the E_{2g} symmetry channel. In conclusion, the elastoresistance coefficient (m_{11}–m_{12}) which represents the nematic susceptibility along the E_{2g} symmetry channel can be obtained by measuring the strain-dependent resistivity anisotropy along two perpendicular crystallographic directions, with x axis along the [100] crystal axis.

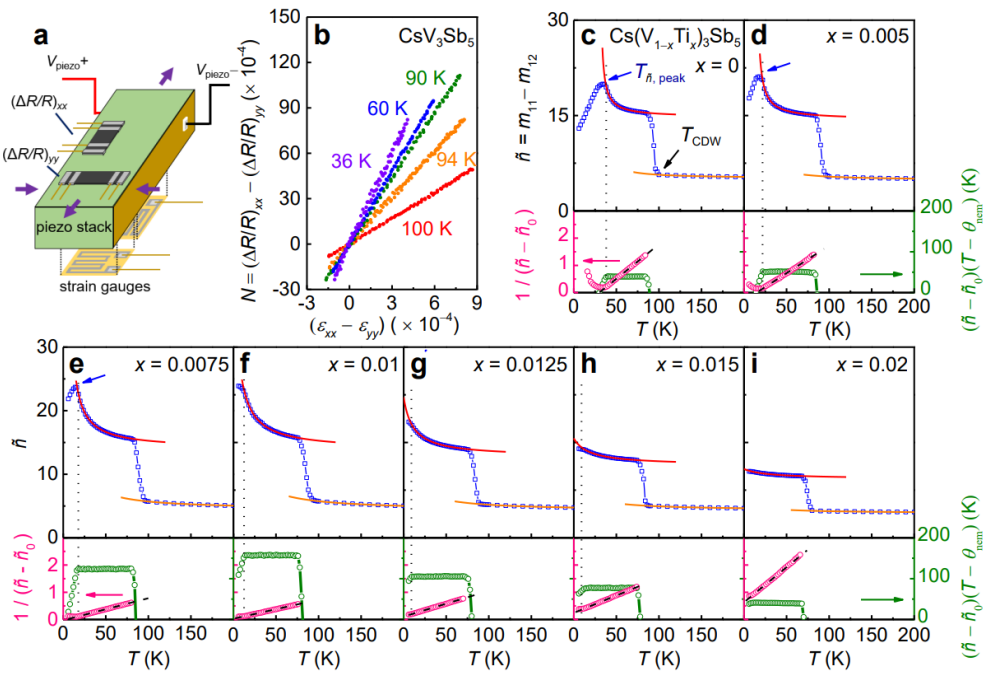

Figure 3.9 (**a**) Schematic illustration of the elastoresistance measurement setup. (**b**) N vs. (ε_{xx}–ε_{yy}) plot of CsV_3Sb_5 at several representative temperatures. (**c**)-(**i**) (top panel) Temperature dependence of $\tilde{n}$ in $Cs(V_{1-x}Ti_x)_3Sb_5$ for $0 \leq x \leq 0.02$. A sharp jump in $\tilde{n}$ is observed near T_{CDW}. Below and above this jump, the data can be clearly fitted to the Curie–Weiss formula (Eq. (1)) (red and orange solid lines,

respectively). The black dotted line indicates the deviation temperature from a Curie–Weiss fit, while the blue arrow indicates the peak temperature of $\tilde{n}$, $T_{\tilde{n},\,\mathrm{peak}}$. (**c**)-(**i**) (bottom panel) Temperature dependence of $(\tilde{n}\text{-}\tilde{n}_0)^{-1}$ and $(\tilde{n}\text{-}\tilde{n}_0)(T\text{-}\theta_{\mathrm{nem}})$ below T_{CDW}, represented by the pink and green open circles, respectively. The black dashed line refers to a linear guide line.

Figure 3.9**b** depicts the response of N to $(\varepsilon_{xx}–\varepsilon_{yy})$ for CsV_3Sb_5 at selected temperatures. N shows a linear relationship with $(\varepsilon_{xx}–\varepsilon_{yy})$. The resulting $\tilde{n}(T)$ curve for CsV_3Sb_5 is presented in the top panel of Figure 3.9**c**. A sharp jump in $\tilde{n}$ is found at T_{CDW} = 98 K, implying that the first-order structural transition due to the charge order results in an abrupt offset change in the elastoresistance anisotropy. It is found that at temperatures above 36 K and below the sharp jump near T_{CDW}, $\tilde{n}$ is well fitted by the Curie–Weiss-type temperature dependence,

$$\tilde{n} = \tilde{n}_0 + \frac{C}{T-\theta_{\mathrm{nem}}} \quad .$$

Here, $\tilde{n}_0$ describes the intrinsic anisotropy in the piezoresistivity effect, unrelated to electronic nematicity, θ_{nem} is the mean-field nematic transition temperature, and C is the Curie constant of the corresponding nematic susceptibility. A good agreement of the experimental data to Eq. (1) can be confirmed by a fitted red solid line with θ_{nem} = 30 K, $\tilde{n}_0$ = 14.7, and C = 39 K. A good fit to Eq. (1) can also be verified by the plots of $(\tilde{n}-\tilde{n}_0)^{-1}$ and $(\tilde{n}-\tilde{n}_0)(T-\theta_{\mathrm{nem}})$ at the bottom panel of Fig. 3**c**, which exhibit linear (pink open circles) and constant (green open circles) behaviours with temperature, respectively. The nearly constant value of $(\tilde{n}-\tilde{n}_0)(T-\theta_{\mathrm{nem}})$ should directly correspond to the C value.

Similar measurements and analyses were performed for $Cs(V_{1-x}Ti_x)_3Sb_5$ up to x = 0.06 (Figures 3.9**d-i)**. It is noted that the jump in $\tilde{n}$ at T_{CDW} systematically decreases with increasing x, indicating weakened elastoresistance anisotropy at the CDW ordering. More importantly, we find that all the samples up to x = 0.03 exhibit the Curie–Weiss temperature dependence of $\tilde{n}$ in broad temperature ranges above deviation temperatures represented by black dotted lines. For x = 0-0.0075, $\tilde{n}$ data clearly develop a peak at $T_{\tilde{n},\,peak}$. In a previous work on the pristine sample[14], T_{nem} identified by NMR and $T_{\tilde{n},\,peak}$ determined by the $\tilde{n}$ measurements were indeed nearly same as ~35 K. Therefore, $T_{\tilde{n},\,peak}$ can be used as a good estimate of T_{nem} for each doping. In our case, the resultant $T_{\tilde{n},\,peak}$ = 34 K for x = 0 is indeed close to the known value of T_{nem} = ~35 K [18]. For other x, $T_{\tilde{n},\,peak}$ shows a monotonous decrease; $T_{\tilde{n},\,peak}$ = 18 K (x = 0.005) and 14 K (x = 0.0075). For x = 0.01, however, we did not identify any peak feature at least down to 6 K, except finding the deviation temperature from the Curie-Weiss behaviour at ~12 K. This observation indicates that for x = 0.01, the true long-range nematic ordering is located well below 6 K or might not even exist at a finite temperature. For x = 0.0125 and 0.015, $\tilde{n}(T)$ doesn't show any peak feature either, and only the deviation from the Curie-Weiss behaviour is identified around ~8 K. This indicates that in x = 0.0125 and 0.015, only nematic correlation exists without development of true long-range order at a finite temperature.

In order to understand quantitatively the evolution of $\tilde{n}$ over the broad doping ranges, we have tried to fit the experimental $\tilde{n}(T)$ of all the samples by Eq. (1) below T_{CDW}. (see, SM Table S2 for detailed fit parameters). Firstly, we discuss the evolution of C for each doping. In contrast to the monotonic decrease in the

jump of $\tilde{n}(T)$ and $T_{\tilde{n},\,\mathrm{peak}}$ with x, C is found to exhibit non-monotonic behaviour, i.e. increasing trend with x for x = 0.0-0.01 and decreasing trend for $x \geq 0.0125$; C, as indicated by the slope of $(\tilde{n}-\tilde{n}_0)^{-1}$ or the value of $(\tilde{n}-\tilde{n}_0)(T-\theta_{\mathrm{nem}})$, increases with x from C = 39 K (x = 0) to 124 K (x = 0.0075), and exhibits a maximum value of C = ~157 K at a critical doping of x_c = 0.01. As a result, the highest value of $\tilde{n}(T = 6\ \mathrm{K}) \sim 23.8$ can be found at x_c. For $x \geq 0.0125$, C decreases with x to exhibit C = 2 K at x = 0.03, resulting in a flattening of the $\tilde{n}(T)$ curve at higher doping ratios. For $x \geq 0.04$, Eq. (1) cannot be fitted very well to the $\tilde{n}(T)$ curves due to almost temperature-independent behaviour below and above the T_{CDW}.

The fit to Eq. (1) strikingly reveals that θ_{nem} is systematically suppressed from 30.0 K (x = 0) to 3.6 K (x = 0.0075), and to eventually exhibit a sign change (x = ~0.009). At higher x, θ_{nem} is suppressed further, resulting in θ_{nem} = -42 K at x = 0.03. In general, a nematic quantum critical point (NQCP) is often located at the phase space where θ_{nem} goes to zero temperature and strongly enhanced nematic susceptibility exists. The systematic suppression of θ_{nem} to zero temperature at x = ~0.009, combined with the sharp maximum of the C value and the disappearance of $T_{\tilde{n},\,\mathrm{peak}}$ near x_c, strongly suggests the presence of a NQCP near the doping level close to $x \sim$ 0.009-0.01. Indeed, similar phenomena have been observed in numerous Fe-based systems having the NQCP [34-38].

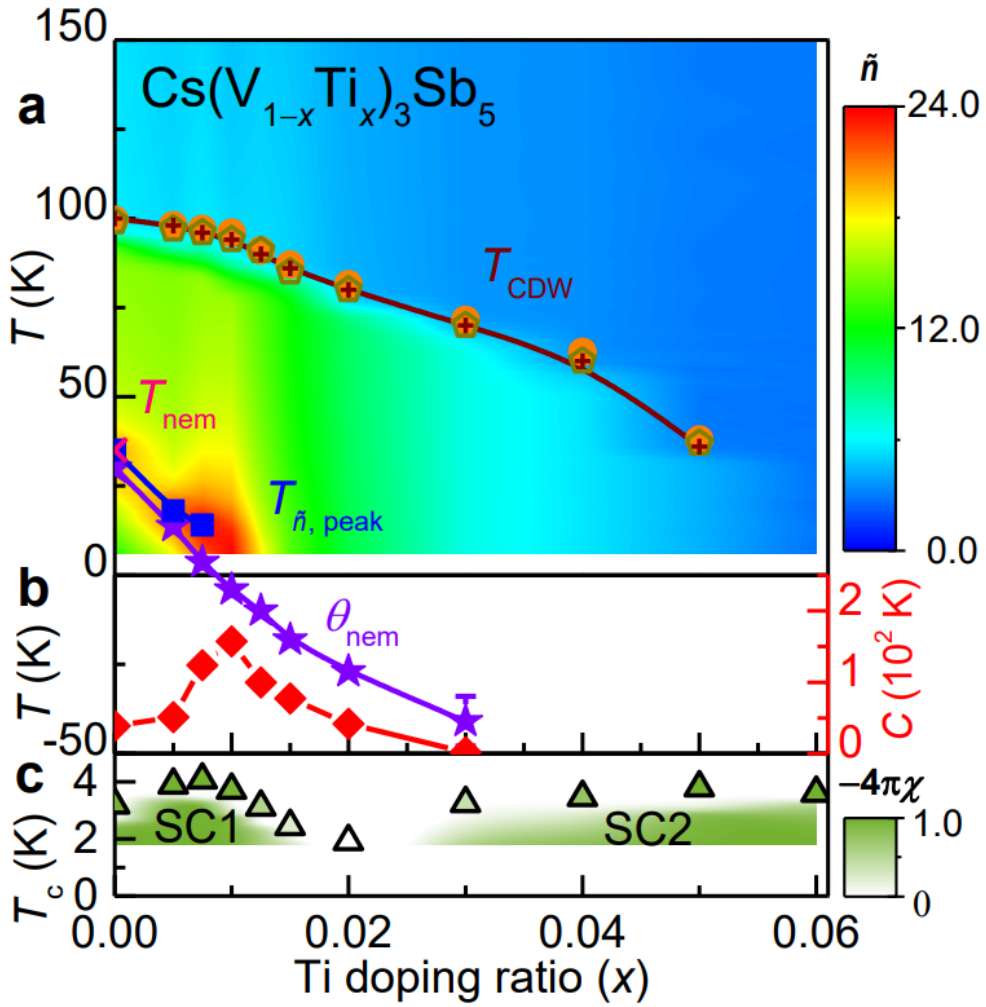

Figure 3.10 (**a**) A temperature(T)-doping(x) phase diagram of $Cs(V_{1-x}Ti_x)_3Sb_5$, indicating the charge ordering temperatures T_{CDW}, the nematic transition temperature T_{nem}, the peak temperature of the elastoresistance data $T_{\tilde{n},\,peak}$, and the Curie-Weiss temperature θ_{nem}. The orange circles, yellow octagons, and the brown crosses indicate the T_{CDW} obtained by the ρ_{ab}, M/H, and elastoresistance measurements. The pink cross, blue squares, and purple stars represents the nematic transition temperature obtained from ref. [18], the $T_{\tilde{n},\,peak}$, and the θ_{nem} respectively. A color contour of $\tilde{n}$ is plotted on top of the phase diagram. (**b**) Doping dependence of the Curie constant C obtained from the elastoresistance measurements. (**c**) Doping dependence of the superconducting transition temperatures T_c (green triangles). The green color contour indicates the

Meissner volume fraction (-4πχ).

Figure 4**a**-**b** summarises the phase diagram of $Cs(V_{1-x}Ti_x)_3Sb_5$ plotted on top of the colour contour of $\tilde{n}$; T_{CDW} as derived from the data of ρ_{ab} (orange circles), M/H (yellow octagons), and $\tilde{n}$ (brown crosses) are plotted for each x. Moreover, $T_{\tilde{n},\,peak}$ (blue squares) and θ_{nem} (purple stars) obtained from $\tilde{n}$ in Fig. 3 are plotted with the T_{nem} (pink cross) of $x = 0$ determined in a previous work [18]. At $x = 0$, a jump in $\tilde{n}(T)$ near T_{CDW} can be clearly identified by the abrupt change of colour in $\tilde{n}$ from blue at $T > T_{CDW}$ to green at $T < T_{CDW}$. Near T_{nem}, the contour exhibits a yellow colour, indicating a local maximum of $\tilde{n}$ at $T_{\tilde{n},\,peak}$. With increase in doping, the $T_{\tilde{n},\,peak}$ shifts to low temperatures, resulting in the most intensified $\tilde{n}$ (6 K) indicated by the red colour near x = 0.0075-0.01. This behaviour is also confirmed by the maximum of the C value, indicated by the red diamonds.

The superconducting phase diagram of $Cs(V_{1-x}Ti_x)_3Sb_5$ is also plotted in Fig. 4**c**. Here, the green triangles indicate the T_c obtained from transport measurements, while the Meissner volume fraction (-4πχ) is represented below the trace of T_c as a green colour contour. Surprisingly, it is found that T_c is optimized to 4.1 K (3.7 K) near this doping range of x = 0.0075 (0.01), when the nematic correlations indicated by the $\tilde{n}$ and C values are sharply enhanced near the NQCP. Our observation thus raises an intriguing possibility that fluctuation of the nematic order plays an important role in the pairing interaction to optimize superconductivity in the first superconducting dome of $Cs(V_{1-x}Ti_x)_3Sb_5$. At higher doping ratios of $0.01 \leq x \leq 0.02$, T_c is monotonically suppressed with doping, which could be related to the reduced nematic fluctuations as indicated by the decreased $\tilde{n}$ and C values.

Based on our experimental findings and implications, the nematic fluctuations may be important in understanding the superconductivity in the AV_3Sb_5 family. In support of this scenario, it should be noted that the T_c values in KV_3Sb_5 (T_c = 0.93 K) and in RbV_3Sb_5 (T_c = 0.92 K) are lower than that in CsV_3Sb_5 (T_c = 3.2 K) [17]. In addition, unlike the Cs variant, a recent study of Sn doping in polycrystalline KV_3Sb_5 and RbV_3Sb_5 revealed single superconducting domes near the suppression of the CDW orders [33]. All these results, if interpreted correctly, potentially indicate that nematic order and its fluctuations might be absent in both compounds, motivating similar experiments for these materials. Furthermore, our scenario supports that nematic fluctuations should be also considered as an important factor to understand the double superconducting domes reported in pressurized CsV_3Sb_5 [31-32] and in $CsV_3Sb_{5-x}Sn_x$ polycrystals [30].

It should be pointed out that the experimental results found here well resemble those found in the Fe-based superconductors, where unconventional superconductivity is optimized near the NQCP [34-38]. However, in contrast to the iron-based superconductors where the spin density wave order is closely coupled to the nematic order [42], the nematic order in CsV_3Sb_5 are intertwined with the unconventional CDW order, possibly in a form of charge bond order [15, 40]. Recent theoretical studies considering the kagome-Hubbard model have indeed shown that a triple-**q** charge bond order is stabilized below T_{CDW}, described by three complex CDW order parameters. Furthermore, those theories suggest that these CDW order parameters can undergo a continuous variation of their phases at T_{nem} from a triply-degenerate, isotropic phase of $\pi/2$ into two different values, without the change of the isotropic amplitude, thereby resulting in one dimensional

nematic modulation. Therefore, the enhanced nematic correlation might be linked to the quantum phase transition involving a continuous variation of the phases of the triple-**q** CDW order parameters, at which the charge bond order with anisotropic phases, thus called nematic charge bond order, develops from the one with a homogenous phase.

3.7 Conclusion

In conclusion, our experimental findings coherently suggest that a NQCP is located near x = ~0.009-0.01. Moreover, a maximum T_c = ~4.1 K with full Meissner shielding is realized at x = ~0.0075-0.01, forming the first superconducting dome near the NQCP. This not only points out the vital role of nematic fluctuation in enhancing superconductivity but also provides important insights into understanding the link between the multiple orders and superconductivity in CsV_3Sb_5 and related kagome superconductors.

Chapter 4 Pressure-induced quantum critical point of a strong coupling charge density wave order in 2*H*-$Pd_{0.05}TaSe_2$

4.1 Introduction to charge density waves and its origin

In this chapter, the discovery of the pressure-induced quantum critical point of a strong-coupling charge density wave order in 2*H*-$Pd_{0.05}TaSe_2$ will be introduced. However, before addressing the details, the basic concepts of the two different origin of the charge density waves, weak-coupling and the strong-coupling charge density waves should be discussed first.

4.1.1 Weak-coupling origin of charge density wave order

A charge density wave state indicates an ordered state in which the electrons within a material are periodically arranged with respect to each other. These electrons in a charge density wave order can either form a standing wave pattern or in rare cases collectively carry an electron current. In the simple one-dimensional case, the charge density wave order can be explained as the Peierls instability caused by Fermi surface nesting [43]. The top figure of Figure 4.1**a** illustrates a one-dimensional atomic chain model, in which each atom site has one occupied electron above the charge density wave transition temperature T_{CDW}. Figure 4.1**b** shows the representative Fermi surface for

materials that possess similar structures reminescent to this one-dimensional chain. In this case, Most of the Fermi surface is located near the Fermi wave number $q = \pm k_F$, and they overlap completely when a translation of $q = 2k_F$ is applied. This condition where two Fermi surfaces of different electron bands have similar shapes, and some parts of two Fermi surfaces are arranged almost parallel to each other is called the Fermi surface nesting condition. In 1936, Peierls discovered that the 1D system is unstable under this Fermi surface nesting condition [43].

In order to overcome this condition and achieve a stable state, a gap at the position of $q = \pm k_F$ should open, forming the zone boundary of a new unit cell. For the case of $k_F = \pi/a$, a new periodicity will be formed with the real space periodicity of $2a$ and the wavevector of $q = 2k_F$. The bottom figure of Figure 4.1**a** shows the rearranged atoms and the corresponding charge density of the one-dimensional atomic chain model below the charge density wave transition temperautre T_{CDW}. This phenomenon is called the Peierls transition, and the charge density wave formed by this origin of Fermi surface nesting is called the weak-coupling charge density wave order.

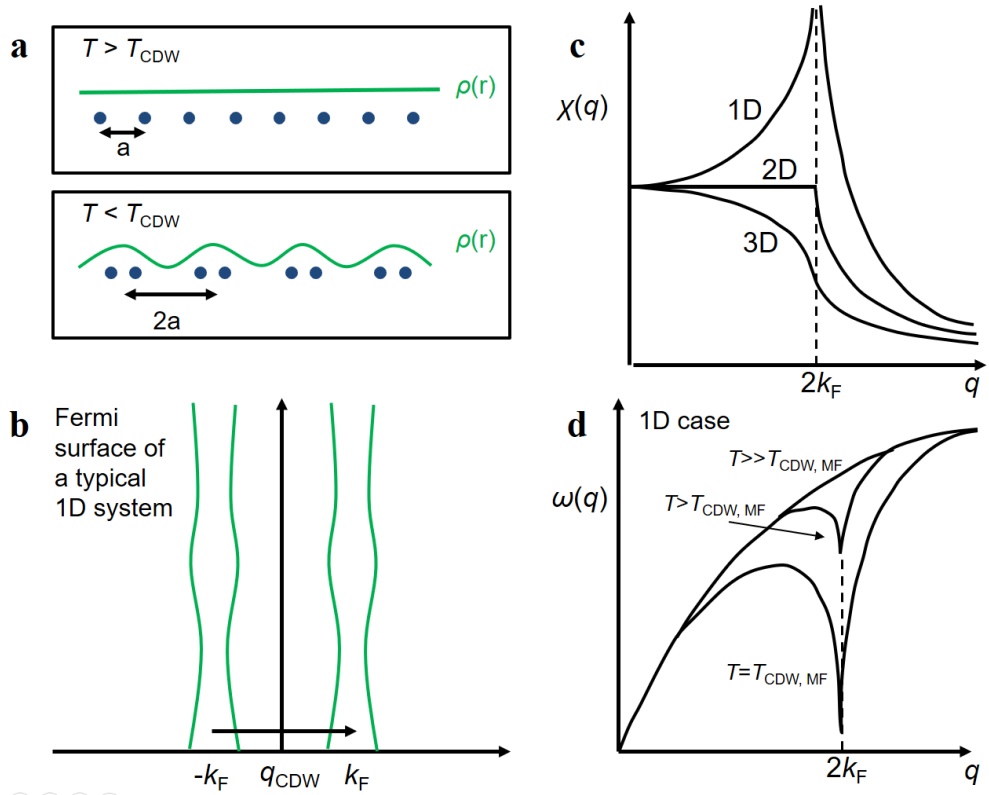

Figure 4.1 (**a**) (top) The atomic positions and the charge density ρ(r) of a one-dimensional atomic chain model. The atoms are equally spaced at a distance a and the charge distribution ρ(r) is shown in the green line. (bottom) a rearranged atomic chain in the charge density wave phase at temperatures below the charge density wave transition temperautre T_{CDW}. (**b**) Representative figure of a two-dimensional Fermi surface for typical quasi-one dimensional material system that exhibits Fermi surface nesting. Here, k_F represents the Fermi wave number, and q_{CDW} represents the Fermi wave vector of the charge density wave. These Fermi surfaces are realized in typical quasi-1D materials such as TTF-TCNQ (Tetrathiafulvalene-Tetracyanoquinodimethane) [44] and $ZrTe_3$ [45]. (**d**) A graph of the momentum (q) dependent Lindhard response function $\chi(q)$ for the 1D, 2D, and 3D ideal free electron gas cases, respectively. (**d**) A schematic figure of the phonon energy $\omega(q)$ in the theoretical 1D atomic chain model for various temperatures relative to the charge density wave transition temperature T_{CDW}.

In order to better understand the Peierls mechanism, one needs to understand the Lindhard response function $\chi(q)$, which represents the electronic stability of the material system. The complex Lindhard response function is defined as below

$$\chi_0(\vec{q},\omega) = \frac{2}{\hbar}\int d\vec{k} f_{\vec{k}}(1-\vec{k}+\vec{q})\left[\frac{1}{\omega+(\epsilon_{\vec{k}}-\epsilon_{\vec{k}+\vec{q}}+i\eta)} - \frac{1}{\omega-(\epsilon_{\vec{k}}-\epsilon_{\vec{k}+\vec{q}}+i\eta)}\right],$$

where ε represents the energy of the electron, and f represents the electron's Fermi distribution function [46]. For the static charge density wave case, in which the imaginary term can be neglected, the Lindhard response function becomes

$$\mathrm{Re}[\chi_0(\vec{q},\omega)] = \frac{1}{(2\pi)^d}\int d\vec{k}\frac{f_{\vec{k}+\vec{q}}-f_{\vec{k}}}{\epsilon_{\vec{k}}-\epsilon_{\vec{k}+\vec{q}}+\omega}.$$

For the theoretical cases in 1D, 2D, and 3D free electron gases, respectively, the equations for the Lindhard response function becomes the equations below.

1D case : $$\mathrm{Re}[\chi_0(\vec{q},\omega)] \propto -\frac{1}{2q} ln\left|\frac{1+q/2}{1-q/2}\right|$$

2D case : $$\mathrm{Re}[\chi_0(\vec{q},\omega)] \propto \begin{cases} -\left(1-\sqrt{1-\left(\frac{2}{q}\right)^2}\right), (q \geq 2k_F) \\ -\frac{1}{E_F}, (q < 2k_F) \end{cases}$$

3D case : $$\mathrm{Re}[\chi_0(\vec{q},\omega)] \propto -\left[1+\frac{1-(q/2)^2}{q}\,ln\left|\frac{1+q/2}{1-q/2}\right|\right]$$

These equations for each dimension is plotted in Figure 4.1**c**, which shows the momentum (q) dependent Lindhard response function $\chi(q)$ for the 1D, 2D, and 3D ideal free electron gas cases. As illustrated in the picture, the $\chi(q)$ for the 2D and 3D systems do not exhibit a divergence in respect to q, indicating that the systems are electronically stable for all q. However, for the 1D system, it is found that the $\chi(q)$ is unstable around a certain q vector, $q = 2k_F$.

In 1959, Kohn discovered that due the phonon energy near this $q = 2k_F$ is reduced in order to prevent this divergence in the $\chi(q)$ value [47]. This reduced value of the phonon energy is called the renormalized phonon energy $\omega_{ren}(q)$, and this phenomena of phonon energy renormalization is referred to as the Kohn anomaly. Interestingly, $\omega_{ren}(q)$ has been found to be a highly temperature dependent functions, and as the temperature is lowered, the value of $\omega_{ren}(q)$ at $q = 2k_F$ reaches to zero at a certain temperature of $T = T_{CDW}$. At this temperatuare, phonons with energy of $q = 2k_F$ freeze out, and a charge density wave order is exhibited. This criteria for the charge density wave formation can be mathematically expressed as below

$$\omega_{ren,q}^2 = \omega_q^2 - \frac{2g_q^2\,\omega_q}{\hbar}\,|Re[\chi_0(\vec{q},\omega)]| \le 0$$

.

Here, $\omega(q)$ represents the original phonon energy, and $g(q)$ represents the momentum dependent electron-phonon coupling constant. As displayed in Figure 4.1**d**, it can be seen that $\omega_{ren}(q = 2k_F)$ in the 1D theoretical model reaches to zero value when $T = T_{CDW}$, leading to the formation of charge density wave order. In the case of $T > T_{CDW}$, the phonon renormalization is still exhibited, but the $\omega_{ren}(q = 2k_F)$ value is a finite positive value. In this case, the charge density wave transition is not exhibited in the system.

4.1.2 Strong-coupling origin of charge density wave order

Unlike the 1D cases where the Fermi surface nesting can naturally arise, in the 2D and 3D cases, it is not possible for all the Fermi surfaces to exhibit the Fermi surface nesting. Therefore, in 2D and 3D cases, only a small portion of the Fermi surfaces typically participate in nesting and the $\chi(q)$ value cannot diverge at any q vector (Figure 4.1**d**). Figure 4.2**a** shows the graph of the momentum dependent phonon energy $\omega(q)$ in the theoretical free electron gas model in 1D, 2D, and 3D cases, which assume the momentum dependent electron-phonon coupling parameter $g(q)$ to be constant. It can be seen that $\omega(q)$ does not become zero for any q value in the 2D and 3D case.

However, several experimental measurements have shown that a sufficient amount of Kohn anomaly and the resulting charge density wave order is still exhibited in some 2D materials (e. g. 2*H*-$NbSe_2$ [46] and 2*H*-$TaSe_2$ [48]), even though there is no divergence in $\chi(q)$ (Figure 4.2**b**). Later, it has been found that this unusual behavior of the Kohn anomaly is due to the

large value of the momentum dependent electron-phonon coupling parameter $g(q)$ near $q = 2k_F$ [46]. This new origin of the charge density wave formed by the increase in $g(q)$, rather than the divergence of $\chi(q)$, is called the strong coupling charge density wave order. Interestingly, in the strong coupling charge density wave cases, a broad Kohn anomaly as large as $\Delta q = 0.2$ is exhibited [48], while the Kohn anomaly in the weak coupling charge density wave cases are found to be narrow with $\Delta q \sim 0.04$ or less [45].

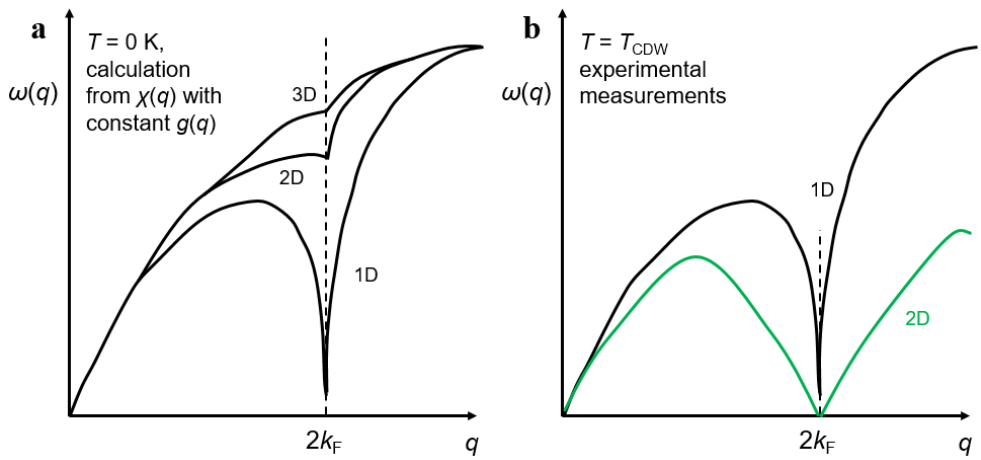

Figure 4.2 (**a**) A graph of the momentum dependent phonon energy $\omega(q)$ in the theoretical free electron gas model in 1D, 2D, and 3D cases, respectively. The calculation was performed assuming constant $g(q)$ values for each cases. (**b**) A schematic figure of the experimentally obtained momentum dependent phonon energy $w(q)$ for the quasi-1D case (e. g. $ZrTe_3$ [45], TTF-TCNQ [44], etc.) and the quasi-2D case (e. g. 2*H*-$NbSe_2$ [46], 2*H*-$TaSe_2$ [47]).

4.1.3 Quantum critical points of charge density wave orders

It is widely documented that superconductivity (SC) can emerge near

the quantum critical point (QCP) of various symmetry-broken phases [11, 49-50, 41, 35]. Defined as a continuous phase transition occurring at absolute zero temperature (T = 0 K), the QCP and its corresponding fluctuations are currently believed to promote superconductivity in various materials in condensed matter physics [11, 49-50, 41, 35]. For example, QCPs of antiferromagnetic orders have been found near the superconducting phase in various cuprates [11] and Mn-based superconductors [49-50]. Similarly, it is well established that fluctuations arising from nematic QCPs are responsible for the superconductivity of iron based superconductors [35, 12]. A charge density wave state, which is an ordering of charge carriers, has also been found alongside superconductivity in many systems so far, ranging from cuprates [11] and Heusler compounds [41] to the recently investigated topological kagome systems [17]. Therefore, similar to other neighboring orders, it is natural to speculate that low-energy fluctuations of a CDW order could also pair the electrons and induce superconductivity.

However, contrary to other orders, the emergence of SC near CDW orders is far from complete understandings. While a competing relation between CDW and SC has been well established since the early 1970s [51], the mechanism for stabilizing superconductivity, as well as the origin of a dome shaped behavior in the superconducting properties, is still not fully understood [52-53]. One of the major laybacks is the scarcity of the material family that exhibits a CDW QCP. While materials that exhibit CDW are not rare, most CDW systems have been found to exhibit a 1st order quenching of the CDW order by external tuning parameters, leading to the avoidance of the CDW QCP and an extended region of superconductivity after the CDW order has been

suppresed [54-56]. Therefore, it is highly desirable to search for systems in which the CDW order exhibits a continuous phase transition at zero temperature.

One promising approach of inducing such a CDW QCP is to tune a temperature dependent 2nd order CDW transition to 0 K, which has been successful in provoking CDW / structural QCPs in $Lu(Pt_{1-x}Pd_x)_2In$ [41] and $(Ca_xSr_{1-x})_3Rh_4Sn_{13}$ [57-58]. In this aspect, the 2*H*-polymorph of tantalum diselenide 2*H*-$TaSe_2$, which exhibits a 2nd order CDW transition at T_{CDW} = 122 K [59] and a superconducting transition at a superconducting transition temperature T_c = 0.14 K [60], can be another good candidate for observing the QCP by applying an external tuning parameter. However, instigation of the CDW QCP in 2*H*-$TaSe_2$ has not been available due to the strong persistence of T_{CDW} under tuning parameters, such as intercalation or doping. For instance, T_{CDW} is reduced by only ~16 K with Pd intercalation between the $TaSe_2$ layers [61], and by ~ 42 K by S doping in the Se site [62] before the CDW order is destabilized by disorder.

In this regard, pressure (*P*), which is a clean method that does not introduce disorder, can be a suitable tuning parameter to fully suppress the CDW energy scale down to zero temperature. Here, we employ high pressures to study the electrical transport and vibrational properties in a Pd 5% intercalated 2*H*-$TaSe_2$ single crystal with a reduced CDW transition temperature of T_{CDW} = 115 K. The combined measurements of resistivity and Hall effect indicates that a full suppression of the CDW order is exhibited near a critical pressure P_c = 22.1 GPa. In order to study the phonon dispersions related to the CDW order, the two-

phonon Raman modes were performed as a function of pressure. Furthermore, the low-temperature resistivity measured at a magnetic field of $\mu_0 H$ = 9 T is analyzed to investigate the variation of the electronic density of states near the QCP. Our observations point to a rare example of a CDW QCP at P_c ~ 22.1 GPa, induced by a pressure-tuned Kohn anomaly in 2*H*-$Pd_{0.05}TaSe_2$.

4.2 Crystal structure and electronic properties of 2*H*-$Pd_{0.05}TaSe_2$

Figure 4.3**a** displays the crystal structure of 2*H*-$Pd_{0.05}TaSe_2$. This compound consists of two layers of 1*H*-$TaSe_2$, stacked with a relative angle of 180° to each other. Intercalated Pd ions are situated between the van der Waals layers, as denoted by a red shaded area. Figure 4.3**b** presents the X-ray diffraction (XRD) pattern of a ground single crystal of 2*H*-$Pd_{0.05}TaSe_2$, synthesized using the chemical vapor transport method. The lattice parameters acquired through Rietveld refinement are a = 3.440 ± 0.0005 Å and c = 12.739 ± 0.0005 Å. These values closely resemble the a and c parameters observed in polycrystalline 2*H*-$Pd_{0.05}TaSe_2$ [61], indicating successful intercalation of Pd ions between the 1*H*-$TaSe_2$ layers.

The temperature (T) dependence of in-plane resistivity $\rho_{ab}(T)$ reveals a variety of electronic phase transitions in 2*H*-$Pd_{0.05}TaSe_2$ (Figures 4.3**c-d**). The T-linear behavior at high temperatures suggests an unconventional metallic state associated with pseudogap behavior [61]. As the temperature decreases, a hump near T_{CDW} = 115 K is characterized by the formation of a charge density

wave (CDW) phase, followed by a superconducting (SC) transition near T_c = 2.6 K (Figure 4.3**c**, inset). It is important to note that the intercalation of Pd ions moderately suppresses the CDW phase while significantly enhancing the SC phase, as evidenced by the changes in T_{CDW} and T_c compared to pristine 2*H*-$TaSe_2$ (T_{CDW} = 122 K, T_c = 0.15 K). The suppression of T_{CDW} can be attributed to the reduced dimensionality due to Pd intercalation, as confirmed by the decreased c/a ratio obtained in our previous work [61].

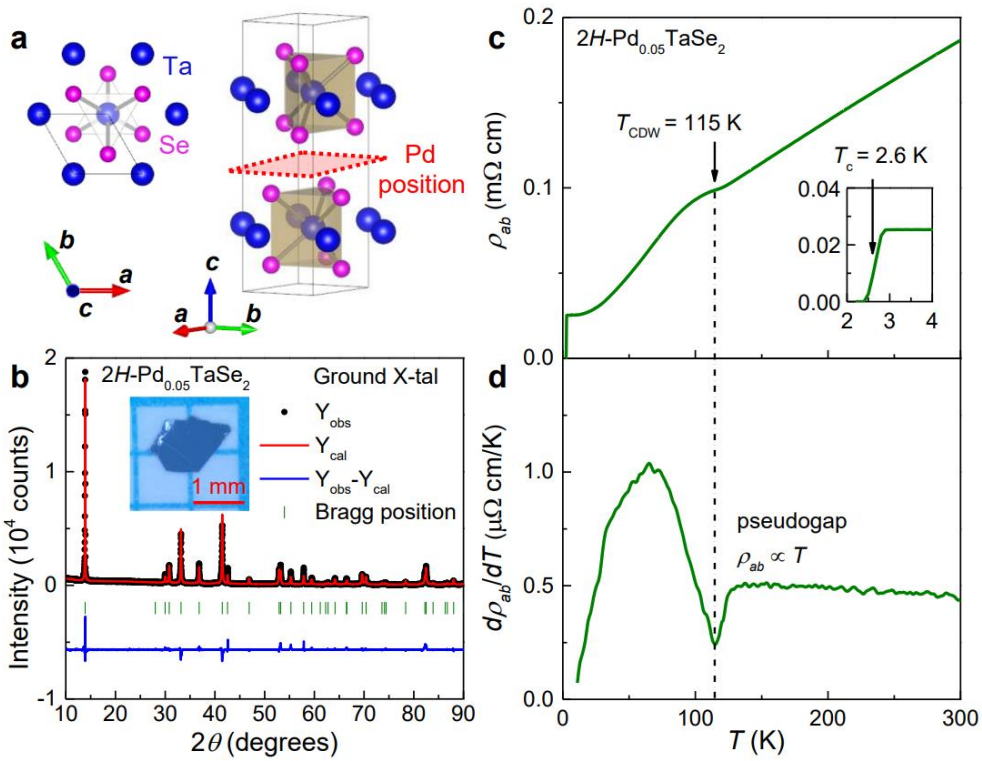

Figure 4.3 (**a**) The crystal structure of 2*H*-$Pd_{0.05}TaSe_2$. The area in red indicates the Pd position. (**b**) An X-ray diffraction pattern of 2*H*-$Pd_{0.05}TaSe_2$. A picture of a 2*H*-$Pd_{0.05}TaSe_2$ single crystal is shown in the inset. (**c**) Temperature-dependent in-plane resistivity of 2*H*-$Pd_{0.05}TaSe_2$. The inset shows a magnified figure of the

temperature-dependent in-plane resistivity near the low temperature region. (**d**) $d\rho_{ab}/dT$ of 2*H*-$Pd_{0.05}TaSe_2$. A dip in the $d\rho_{ab}/dT$ plot indicates the CDW transition temperature.

To investigate the effect of pressure on the CDW order, the temperature dependence of the in-plane resistivity $\rho_{ab}(T)$ is measured at various pressures, as shown in Figure 4.4**a**-**b**. The resistivity value at 200 K decreases to almost 50% at 0.075 mΩ cm at P = 34.7 GPa, from the ambient pressure value of 0.13 mΩ cm, indicating that pressure contributes to increasing the electrical conductivity of the system. Additionally, the hump feature in the resistivity is weakens, and T_{CDW} decreases monotonically to lower temperatures with pressure, signifying the gradual suppression of the CDW order. T_{CDW} is identified with the $d\rho_{ab}/dT$ curve corresponding to a dip that shifts to lower temperatures, down to ~45 K at 20.4 GPa (Figure 4.4**c**). This dip fades at higher pressures, suggesting the disappearance of the CDW order due to a quantum phase transition near a pressure of 21.5 GPa.

The Hall effect measurement at various pressures offers further insight into the electronic structure evolution with pressure. At ambient pressure, the Hall coefficient R_H is positive and exhibits weak *T*-dependence above T_{CDW} (Figure 4.4**d**). Near the onset of the CDW transition, R_H sharply decreases, which is attributed to the opening of the CDW gap located near the K-barrel of the Fermi surface [63]. It is worth noting that the abrupt change in R_H near the CDW transition becomes broader and shifts toward lower temperatures with increasing pressure. The extrapolation of this change to zero Kelvin yields a

critical pressure P_c = ~22.1 GPa, which is close to the pressure of the quantum phase transition determined by the resistivity measurements. The nearly *T*-independent R_H at P_c confirms the complete suppression of the CDW order, a behavior that persists up to pressures as high as 31.8 GPa.

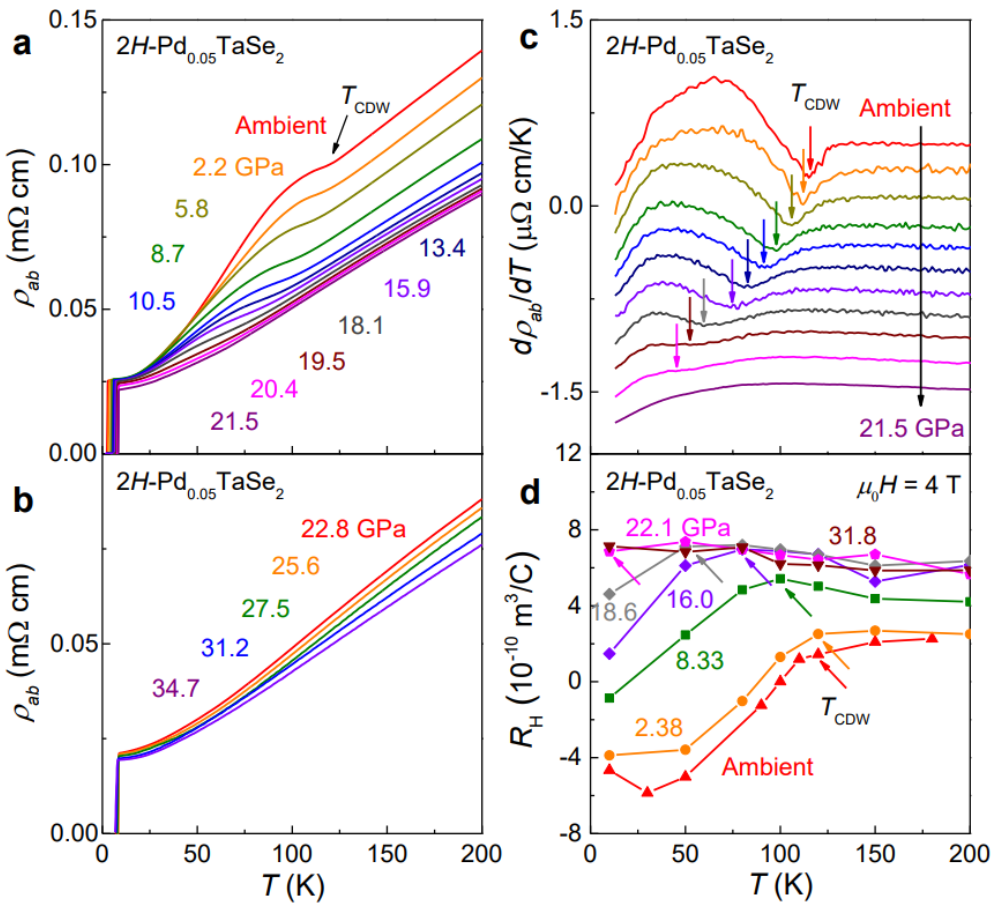

Figure 4.4 Temperature dependence of ρ_{ab} (**a**) for $0 \leq P \leq 21.5$ GPa and (**b**) for $22.8 \leq P \leq 34.7$ GPa. The black arrow marks the charge density wave (CDW) transition temperature T_{CDW}. (**c**) Temperature dependence of $d\rho_{ab}(T)/dT$ for $0 \leq P \leq 21.5$ GPa. Plots are shifted downwards by a constant value for clarity. The colored arrows indicate dips in the $d\rho_{ab}(T)/dT$ data corresponding to T_{CDW}. (**d**) Temperature dependence of the Hall coefficient R_H measured at various pressures between $0 \leq P \leq 31.8$ GPa. The R_H is obtained from a linear fit to the

Hall resistivity measured between -4 T and 4 T. The colored arrows mark the negative drop in the R_H curve.

4.3 Fermi liquid fits to the low-temperature resistivity

As the suppresion of the CDW order has been confirmed by both in-plane resistivity $\rho_{ab}(T)$ and Hall coefficient R_H, one interesting question to ask is whether the CDW order is suppressed in a 1st order quantum transition [54-56], or in a 2nd order quantum transition indicative of a quantum critical point (QCP) [57-58]. To explore this possibility, we have performed low-temperature resistivity measurements with a constant magnetic field of $\mu_0 H$ = 9 T applied parallel to the *c*-axis (Figure 4.5**a**-**b**). A constant magnetic field of $\mu_0 H$ = 9 T was applied to suppress superconductivity, enabling the investigation of normal state transport properties inside the superconducting dome.

At ambient pressure, ρ_{ab} can be described by a quadratic power law fit $\rho_{ab}(T) = \rho_0 + AT^2$ (red solid lines), at least up to a Fermi liquid temperature T_{FL} ~ 10 K where the data deviates upward at higher temperatures. This suggests that Fermi liquid properties dominate the low temperature transport for 2*H*-$Pd_{0.05}TaSe_2$ at ambient pressure below T_{FL}. By following the Rice-Kadowaki-Woods relation, we could associate the *A* value to the Sommerfeld coefficient γ_0 using the equation $A = \alpha_{KW}\ \gamma_0^2$, where α_{KW} is the Kadowaki-Woods ratio [64]. Combined with the γ_0 value of 10.14 mJ/mol K^2 obtained from heat capacity measurements in polycrystalline 2*H*-$Pd_{0.05}TaSe_2$ at 9 T field and

temperatures down to 160 mK (see, Figure 4.6), a α_{KW} value of 1.06 x 10^{-5} (μΩ cm mol^2 K^2 /mJ^2) could be extracted, which is comparable to the values of cuprate [65] and iron based superconductors [66].

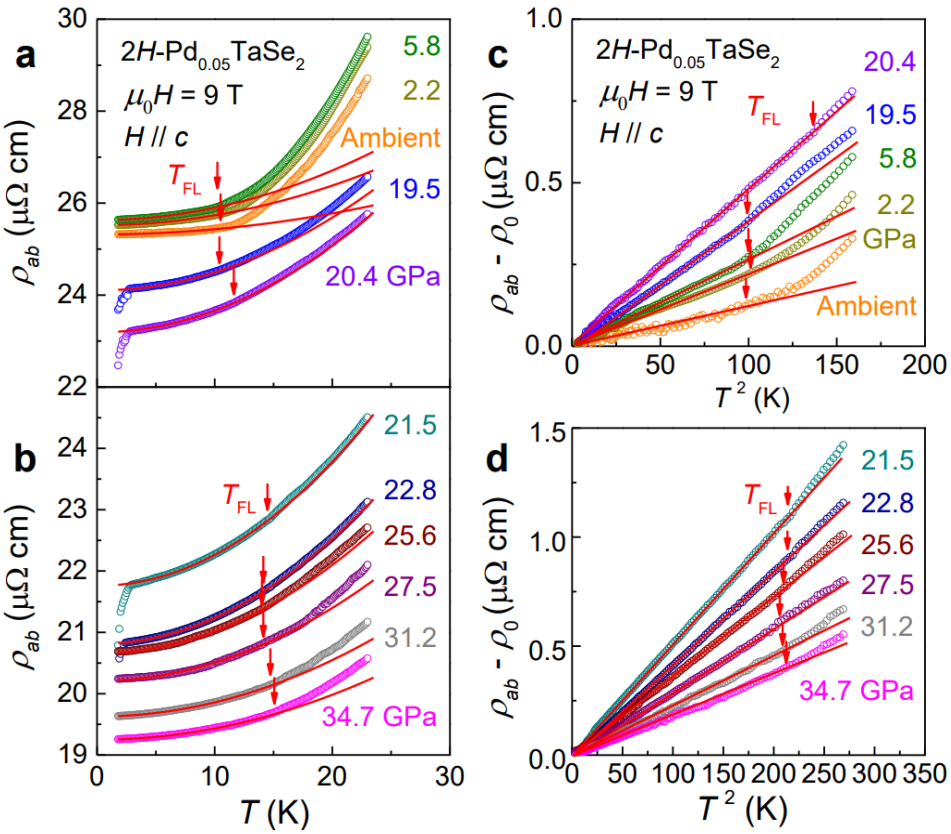

Figure 4.5 Temperature (T) dependence of ρ_{ab} measured at an applied field of $\mu_0 H$ = 9 T in the out-of plane direction (**a**) for $0 \leq P \leq 20.4$ GPa and (**b**) for 21.5 GPa $\leq P \leq$ 34.7 GPa. The red solid lines show the fitting results to a quadratic power law plot of $\rho_{ab}(T) = \rho_0 + AT^2$. Here, ρ_0 is the residual resistivity while A refers to the quadratic power law coefficient. The red arrow marks the Fermi liquid temperature T_{FL} obtained by the deviation temperature of the power law fitting. T^2 dependence of (ρ_{ab} - ρ_0) with an applied field of $\mu_0 H$ = 9 T (**c**) for $0 \leq P \leq 20.4$ GPa and (**d**) for 21.5 GPa $\leq P \leq$ 34.7 GPa. The red solid curves indicate linear guide lines.

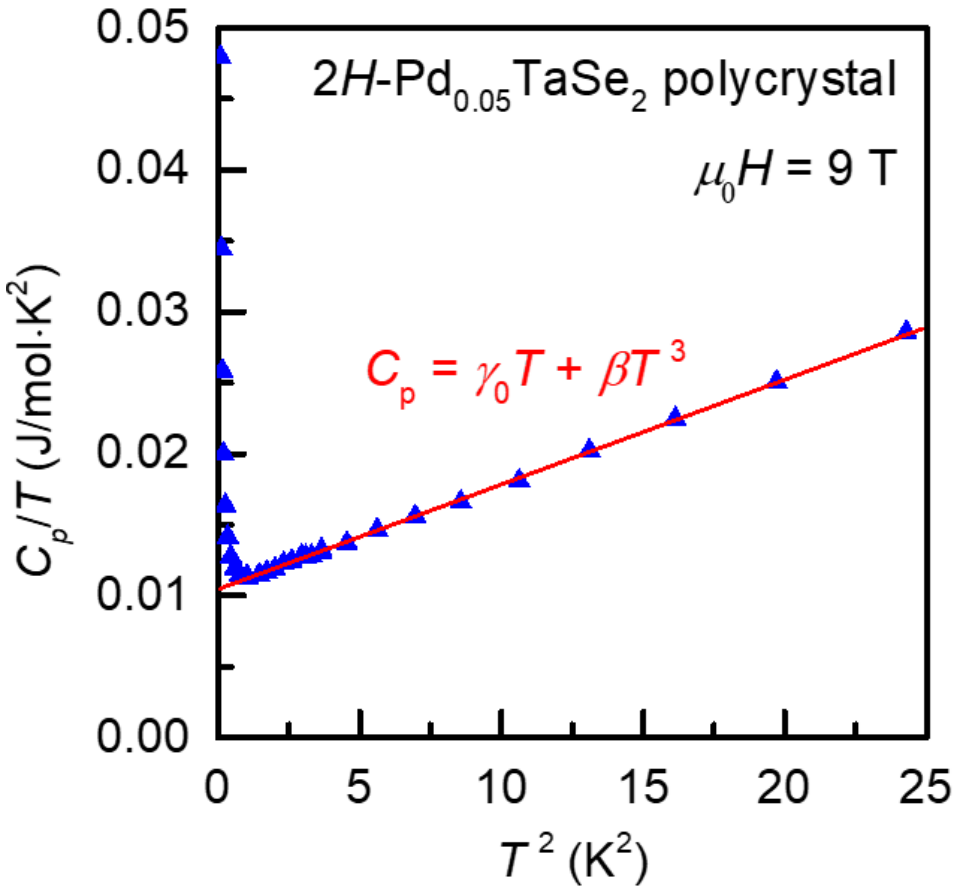

Figure 4.6 The C_p/T vs. T^2 curve of polycrystalline 2*H*-$Pd_{0.05}TaSe_2$ measured at an applied field of $\mu_0 H$ = 9 T. The solid red line represents the linear fit to the data at temperatures between 160 mK and 5 K. The deviation from the linear fit below 0.9 K may be due to the Schottkey anomaly. The extracted values from the linear fits are β = 7.64 mJ/mol K^4 and γ_0 = 10.14 mJ/mol K^2.

With the application of pressure, it is shown that T_{FL} does not change up to 19.5 GPa, indicating a negligible pressure dependence of the Fermi surface properties up to this pressure. However, at 20.4 GPa, T_{FL} exhibits a sudden increase to exhibit T_{FL} ~15 K near P = 21.5 GPa. Moreover, ρ_0 indicated by the extrapolation point to $\rho_{ab}(T)$ at 0 K seem to exhibit a drop near 19.5 GPa, which indicates an enhanced electrical conductivity possibly due to the closure

of the CDW gap near this pressure. If this is true, the sudden enhancement of T_{FL} can be understood by the increase in the overall Fermi surface size, as the fragmented Fermi surface due to the CDW gap formation should recover to its original size with the suppression of the CDW order near P_c.

In addition to the abrupt changes in ρ_0 and T_{FL}, the quadratic power law coefficient A also shows a striking change with pressure. This behavior can be well visualized in the (ρ_{ab}-ρ_0) vs. T^2 plot (Figure 4.5**c**-**d**), in which the residual resistivity ρ_0 is subtracted to better visualize the validity of the quadratic power law fit. It can be seen that the A value gradually increases up to 19.5 GPa. However, A is then quickly enhanced near P_c, exhibiting a sharp peak at P = 21.5 GPa. At higher pressures, the A value is quickly suppressed to exhibit lower values at 34.7 GPa. Assuming that the Kadowaki-Woods relation holds in 2*H*-$Pd_{0.05}TaSe_2$, it could be seen that γ_0 exhibits a factor 2.3 increase with pressure. As γ_0 is regarded to be proportional to the effective mass by the Sommerfeld equation, this experimental result suggests that there a sharp increase of effective mass is exhibited in a small pressure range of ~ 5 GPa. This result suggests that a quantum critical point (QCP) is exhibited in 2*H*-$Pd_{0.05}TaSe_2$ with pressure.

4.4 Raman spectra

To better understand the evolution of the phonon dispersions and the stability of the CDW phase under pressure, Raman spectra were employed at

room temperature up to 35.2 GPa. Figure 4.7**a** presents the Raman response of 2*H*-$Pd_{0.05}TaSe_2$ at ambient pressure, where three phonon modes are observed; a two-phonon mode at 141.5 cm^{-1}, an in-plane E_{2g}^1 vibrational mode at 206.0 cm^{-1}, and an out-of-plane A_{1g} mode at 232.3 cm^{-1}, These values agree well with the reported studies of 2*H*-$TaSe_2$ [67]. Here, we focus on the evolution of the two-phonon mode, which is known to be originated from the presence of a substantially softened acoustic phonon near the CDW *q*-vector at temperatures as high as 300 K [48]. Recently, it has been shown that this phonon softening is driven by a progressive shortening of the Ta-Ta bonding distance, termed as local lattice distortions [68].

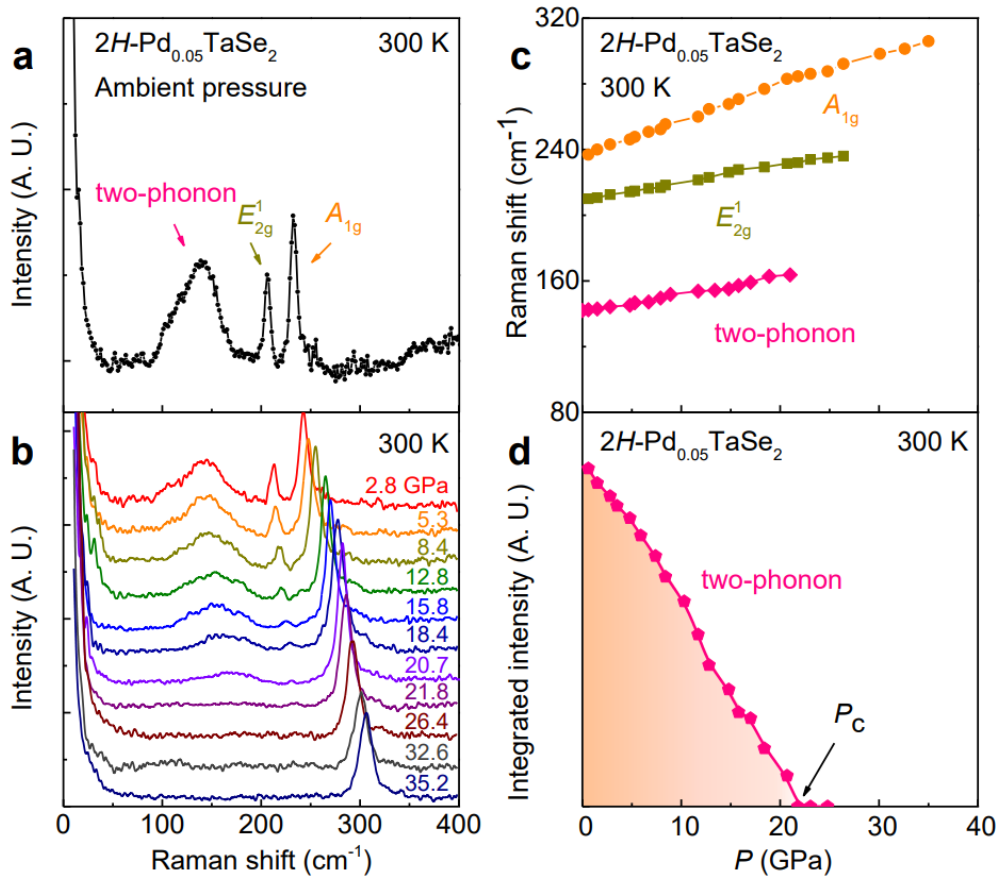

Figure 4.7 (**a**) The room temperature Raman spectrum of 2*H*-$Pd_{0.05}TaSe_2$ at ambient pressure. (**b**) Room temperature Raman spectra of 2*H*-$Pd_{0.05}TaSe_2$ at various pressures. (**c**) The Raman peak positions of 2*H*-$Pd_{0.05}TaSe_2$. The orange circles, yellow squares, and the pink diamonds indicate the peak positions of the A_{1g}, $E_{2g}{}^1$, two-phonon Raman modes, respectively. (**d**) The pressure-dependent integrated intensity of the two-phonon Raman mode.

Figure 4.7**b** shows the pressure evolution of the Raman spectra. Upon application of pressure, all Raman modes show blue-shifts in energy, accompanied by progressive widening of the peak signals. The positions of the three peaks vs. pressure are shown in Figure 4.7**c**. The pressure dependence of the A_{1g} and $E_{2g}{}^1$ does not exhibit any anomalies up to 26 GPa, indicating that a structural phase transition does not occur up to this pressure. Therefore, we conclude that the suppression of the CDW order at P_c = 22.1 GPa is not driven by any pressure-induced structural phase transition. This observation is indeed consistent with the recent XRD measurements in 2*H*-$TaSe_2$ under pressure up to 20 GPa [69].

In contrast to the one-phonon modes, the two-phonon Raman mode shows a non-monotonic evolution under pressure. While the frequency of the two-phonon mode does not change significantly, the intensity of this mode progressively decreases with applied pressure (Figure 4.7**d**). Following the theory presented by Klein *et al*. [70], the intensity of the two-phonon scattering I in 2*H*-$TaSe_2$ is related to the renormalized phonon energy of the

$$I \propto \left[\frac{\omega(\vec{q})^2 - \tilde{\omega}(\vec{q})^2}{2\omega(\vec{q})}\right]^2$$

acoustic phonon by ,

where $\omega_{ren,q}^2 = \omega_q^2 - \frac{2g_q^2\,\omega_q}{\hbar}|Re[\chi_0(\vec{q},\omega)]| \leq 0$.

Here, $\omega(q)$ represents the original phonon energy, $\omega_{ren}(q)$ represents the renormalized phonon energy, $\chi(q)$ indicates the momentum-dependent electronic susceptibility, and $g(q)$ represents the momentum dependent electron-phonon coupling constant. Therefore, the intensity of the two-phonon Raman mode can effectively scale the phonon renormalization. It could be seen in Figure 4.7**d** that the intensity of the two-phonon Raman mode leads to a complete disappearance at 21.8 GPa. As these Raman modes are closely linked to the short-range local lattice distortions of the CDW order above T_{CDW}, it could be concluded that local lattice distortions at high temperature are also suppressed near P_c, closely following the suppression of the long-ranged CDW order at low temperatures. Recalling that the local lattice distortions are regarded as a precursor phase to the CDW order, this observation suggests that the suppression of the CDW order is driven by the suppression of the Kohn anomaly and the short range local lattice distortions above T_{CDW}, which are continuously tuned by the application of pressure.

Figure 4.8**a** shows a summary of the pressure-temperature phase diagram of 2*H*-$Pd_{0.05}TaSe_2$; T_{CDW} as derived from the data of ρ_{ab} and R_H are plotted for each *P*. Moreover, the T_c obtained from ρ_{ab} are plotted as green triangles. The shade of orange indicates the presence of local lattice distortions obtained from the analysis of Figure 4.7, while the yellow and green shaded regions indicate the CDW and SC phases, respectively. Figure 4.8**b** depicts the

pressure dependence of R_H measured at 10K, measured just above the superconducting transition temperature T_c. Figure 4.8**c-e** shows the pressure dependence of the Fermi liquid temperature T_{FL}, residual resistivity ρ_0, and the quadratic power law coefficient A obtained from the analysis in Figure 4.5.

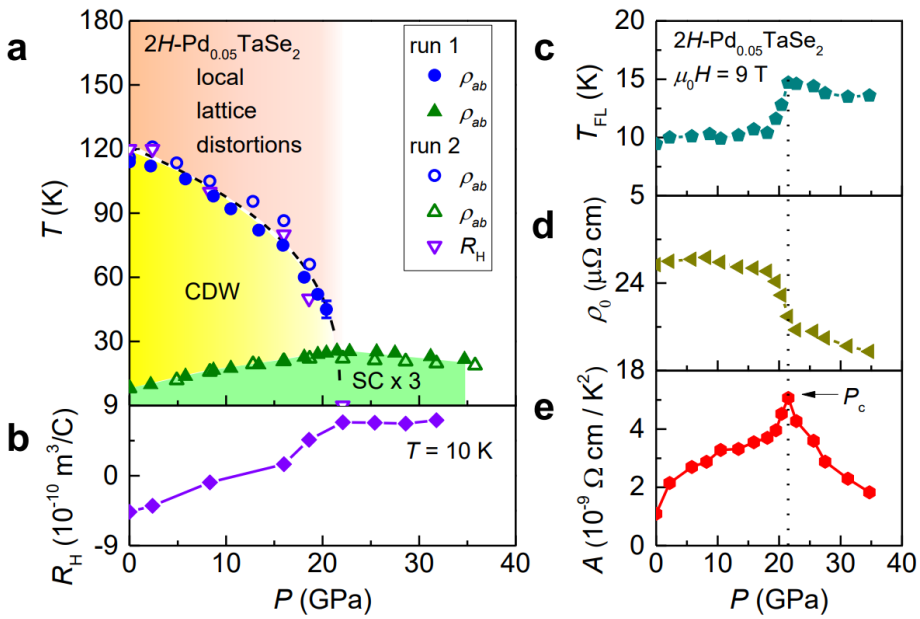

Figure 4.8 (**a**) Electronic phase diagram of 2*H*-$Pd_{0.05}TaSe_2$ with pressure. The filled blue circles represent T_{CDW} obtained from the ρ_{ab} measurement in the 1st run, while the unfilled blue circles and the unfilled purple triangles represent the T_{CDW} from the ρ_{ab} and R_H measurements in the 2nd run. A dashed black curve is shown for a guide to the eye. The filled (unfilled) green triangles represent the T_c obtained from ρ_{ab} measurements in the 1st (2nd) runs, respectively. The T_c is multiplied by a factor of 3 for clarity. (**b**) Pressure dependence of the Hall coefficient R_H (purple diamonds) measured at 10K. Pressure dependence of (**c**) the Fermi liquid temperature T_{FL}, the fitting parameters (**d**) ρ_0, and (**e**) A determined by quadratic power law plots of $\rho = \rho_0 + AT^2$ from Fig. 4.5. A vertical dotted line indicates the critical pressure $P_c \sim$ 21.5 GPa.

As the T_{CDW} is suppressed to result in a quantum critical point, T_c increases systematically. Intriguingly, our experimental observations clearly point out that the optimal T_c is manifested at the CDW quantum critical point, corroborating a strong correlation between the CDW order and the underlying superconductivity. The dome-shape of the superconducting properties can be further confirmed by the pressure evolution of the upper critical fields $\mu_0 H_{c2}(0)$, which is shown in the main manuscript of this paper [71].

At present, the generic origin for the increase of A near the quantum critical point of P_c in pressurized 2H-$Pd_{0.05}TaSe_2$ remains as an open question. One scenario is that the increase of the electronic density of states $N(E_F)$ due to the proximity of the system to the quantum critical point may increase the A value. If this scenario is true, it is expected that the collapse of multiple Fermi surface in the CDW phase across the quantum critical point could cause the increase of $N(E_F)$, and eventually A. Another scenario is that the fluctuations of the CDW amplitudons in the vicinity of the CCDW QCP provides the additional interaction for superconducting pairing [53]. It might be worthwhile to check the feasibility of both scenarios in future studies.

4.5 Conclusion

In conclusion, we report the electrical transport and vibrational properties in a Pd 5% intercalated 2H-$TaSe_2$ single crystal with a reduced CDW transition temperature of T_{CDW} = 115 K. The combined measurements of resistivity and Hall effect indicates that a full suppression of the CDW order is

exhibited near a critical pressure P_c = 22.1 GPa. In order to study the phonon dispersions related to the CDW order, the two-phonon Raman modes were performed as a function of pressure. Furthermore, the low-temperature resistivity measured at a magnetic field of $\mu_0 H$ = 9 T is analyzed to investigate the variation of the electronic density of states near the QCP. Our observations point to a rare example of a CDW QCP at P_c ~ 22.1 GPa, induced by a pressure-tuned Kohn anomaly in 2*H*-$Pd_{0.05}TaSe_2$.

Bibliography

1. Onnes, H. K. The Superconductivity of Mercury. *Commun. Phys. Lab. Univ. Leiden* **12**, 120 (1911).
2. Lee, H. -W. *et al*. Review of maglev train technologies. *IEEE Trans. Magn.* **42**, 7 (2006).
3. London, F. & London, H. The electromagnetic equations of the supraconductor. *Proc. R. Soc. A* **149**, 71 (1935).
4. Ginzburg, V. L. & Landau, L. D. On the Theory of superconductivity. *J. Exp. Theor. Phys.* **20**, 1064 (1950).
5. Bardeen, J. *et al*. Theory of Superconductivity. *Phys. Rev.* **108**, 1175 (1957).
6. Nagamatsu, J. *et al*. Superconductivity at 39 K in magnesium diboride. *Nature* **410**, 63 (2001).
7. Schilling, A. *et al*. Superconductivity above 130 K in the Hg–Ba–Ca–Cu–O system. *Nature* **363**, 56 (1993).
8. Suhl, H. *et al*. Bardeen-Cooper-Schrieffer Theory of Superconductivity in the Case of Overlapping Bands. *Phys. Rev. Lett.* **3**, 12 (1959).
9. Maki, K. Introduction to *d*-wave superconductivity. *AIP conference Proceedings* **438**, 83 (1998).
10. Chubukov, A. Pairing Mechanism in Fe-Based Superconductors. *Annu. Rev. Condens. Matter Phys.* **3**, 57 (2012).
11. Proust, C. *et al*. The Remarkable Underlying Ground States of Cuprate Superconductors. *Annu. Rev. Condens. Matter Phys.* **10**, 409 (2018).
12. Malinowski, P. *et al*. Suppression of superconductivity by anisotropic strain near a nematic quantum critical point. *Nat. Phys.* **16**, 1189 (2020).
13. Wang, W. *et al*. Competing electronic orders on kagome lattices at van Hove filling. *Phys. Rev. B* **87**, 115135 (2013).
14. Kiesel, M. L. *et al*. Unconventional Fermi Surface Instabilities in the Kagome Hubbard Model. *Phys. Rev. Lett* **110**, 126405 (2013).
15. Denner, M. M. *et al*. Analysis of Charge Order in the Kagome Metal AV_3Sb_5 (A = K, Rb, Cs). Phys. Rev. Lett. **127**, 217601 (2022).
16. Yu, S. –L. & Li, J. –X. Chiral superconducting phase and chiral spin-density-wave phase in a Hubbard model on the kagome lattice. *Phys. Rev.*

B **85**, 144402 (2012).

17. Neupert, T. *et al*. Charge order and superconductivity in kagome materials. *Nat. Phys.* **18**, 137 (2022).

18. Nie, L. *et al*. Charge-density-wave-driven electronic nematicity in a kagome superconductor. *Nature* **604**, 59 (2022).

19. Tazai, R. *et al*. Mechanism of exotic density-wave and beyond-Migdal unconventional superconductivity in kagome metal AV_3Sb_5 (A = K, Rb, Cs). *Sci. Adv.* **8**, eabl4108 (2022).

20. Shibauchi, T. *et al*. A Quantum Critical Point Lying Beneath the Superconducting Dome in Iron Pnictides. *Annu. Rev. Condens. Matter Phys.* **5**, 113 (2014).

21. He, M. *et al*. Strong-coupling superconductivity in the kagome metal CsV3Sb5 revealed by soft point-contact spectroscopy. *Phys. Rev. B* **106**, 104510 (2022).

22. Mi, X. *et al*. Multiband effects in thermoelectric and electrical transport properties of kagome superconductors AV_3Sb_5 (A = K, Rb, Cs). *New J. Phys.* **24**, 093021 (2022).

23. Zhang, W. *et al*. Emergence of large quantum oscillation frequencies in thin flakes of the kagome superconductor CsV_3Sb_5. *Phys. Rev. B* **106**, 195103 (2022).

24. Kuo, H. -H. *et al*. Measurement of the elastoresistivity coefficients of the underdoped iron arsenide $Ba(Fe_{0.975}Co_{0.025})_2As_2$. *Phys. Rev. B* **88**, 085113 (2013).

25. Li, B. *et al*. Diamond anvil cell behavior up to 4 Mbar. *Proc. Natl. Acad. Sci. U. S. A.* **115**, 1713 (2018).

26. Mao, H. K. *et al*. Calibration of the ruby pressure gauge to 800 kbar under quasi-hydrostatic conditions. *J. Geophys. Res.* **91**, 4673 (1986).

27. Kittel, C. *Introduction to Solid State Physics*. Wiley, 8th edition (2004).

28. Xu, S. *et al*. Superconducting phase diagrams of S-doped 2*H*–$TaSe_2$ under hydrostatic pressure. *Phys. Rev. B* **102**, 184511 (2020).

29. Oliveira, F. S. *et al*. Simple analytical method for determining electrical resistivity and sheet resistance using the van der Pauw procedure. *Sci. Rep.* **10**, 16379 (2020).

30. Oey, Y. M. *et al.* Fermi level tuning and double-dome superconductivity in the kagome metal $CsV_3Sb_{5-x}Sn_x$. *Phys. Rev. Materials* **6,** L041801 (2022).

31. Chen, K. Y. *et al*. Double superconducting dome and triple enhancement of T_c in the kagome superconductor CsV_3Sb_5 under high pressure. *Phys. Rev. Lett.* **126,** 247001 (2021).

32. Yu, F. H. *et al.* Unusual competition of superconductivity and charge-density-wave state in a compressed topological kagome metal. *Nat. Commun.* **12,** 3645 (2021).

33. Oey, Y. M. Kaboudvand, F. Ortiz, B. R. Seshadri, R. & Wilson, S. D. Tuning charge density wave order and superconductivity in the kagome metals $KV_3Sb_{5-x}Sn_x$ and $RbV_3Sb_{5-x}Sn_x$. *Phys. Rev. Materials* **6,** 074802 (2022).

34. Chu, J. -H. Kuo, H. -H. Analytis, J. G. & Fisher, I. R. Divergent nematic susceptibility in an iron arsenide superconductor. *Science* **337,** 710–712 (2012).

35. Kuo, H. –H. Chu, J. –H. Palmstrom, J. C. Kivelson, S. A. & Fisher, I. R. Ubiquitous signatures of nematic quantum criticality in optimally doped Fe-based superconductors. *Science* **352,** 958-962 (2016).

36. Hosoi, S. *et al*. Nematic quantum critical point without magnetism in $FeSe_{1-x}S_x$ superconductors. *Proc. Natl. Acad. Sci. U. S. A.* **113**, 29 (2016).

37. Hong, X. *et al*. Evolution of the nematic susceptibility in $LaFe_{1-x}Co_xAsO$. *Phys. Rev. Lett.* **125,** 067001 (2020).

38. Ishida, K. *et al*. Pure nematic quantum critical point accompanied by a superconducting dome. *Proc. Natl. Acad. Sci. U.S.A.* **118,** e2110501119 (2022).

39. Miao, H. *et al*. Geometry of the charge density wave in the kagome metal AV_3Sb_5. *Phys. Rev. B* **104**, 195132 (2021).

40. Tazai, R. Yamakawa, Y. Kontani, H. Charge-loop current order and Z_3 nematicity mediated by bond-order fluctuations in kagome metal AV_3Sb_5 (A = Cs, Rb, K). Preprint at https://doi.org/10.48550/arXiv.2207.08068 (2022).

41. Gruner, T. *et al*. Charge density wave quantum critical point with strong enhancement of superconductivity. *Nat. Phys.* **13**, 967-972 (2017).

42. Fernandes, R. M. Chubukov, A. V. & Schmalian, J. What drives nematic order in iron-based superconductors? *Nat. Phys.* **10**, 97-104 (2014).

43. Grüner, G. *Density waves in solids*, Addison-Wesley, (1994).

44. Koizumi, K. *et al*. Bulk-Sensitive Angle-Resolved Photoemission Spectroscopy on TTF-TCNQ. *J. Phys. Soc. Jpn.* **82**, 025004 (2013).

45. Hoesch M. *et al*. Giant Kohn Anomaly and the Phase Transition in Charge Density Wave $ZrTe_3$. *Phys. Rev. Lett.* **102**, 086402 (2009).

46. Zhu X. *et al*. Misconceptions associated with the origin of charge density waves. *Advances in Physics X* **2**, 622 (2017).

47. Kohn, W. Image of the Fermi Surface in the Vibration Spectrum of a Metal. *Phys. Rev. Lett* **2**, 393 (1959).

48. Shen, X. *et al*. Precursor phase with full phonon softening above the charge-density-wave phase transition in 2*H*-$TaSe_2$. Preprint at https://doi.org/arXiv.2207.11298 (2022).

49. Cheng, J. G. *et al*. Pressure Induced Superconductivity on the border of Magnetic Order in MnP. *Phys. Rev. Lett.* **114**, 117001 (2015).

50. Liu. Z. Y. *et al*. Pressure-Induced Superconductivity up to 9 K in the Quasi-One-dimensional KMn_6Bi_5. *Phys. Rev. Lett.* **128**, 187001 (2022).

51. Bilbro G. & McMillan, W. L. Theoretical model of superconductivity and the martensitic transformation in A15 compounds. *Phys. Rev. B* **14**, 5 (1976).

52. Das, T. & Dolui, D. Superconducting dome in MoS_2 and $TiSe_2$ generated by quasiparticle-phonon coupling. *Phys. Rev. B* **91**, 094510 (2015).

53. Halbinger, J. Pimenov, D. & Punk. Incommensurate $2k_F$ density wave quantum criticality in two-dimensional metals. *Phys. Rev. B* **99**, 195102 (2019).

54. Sipos, B. *et al*. From Mott state to superconductivity in 1*T*-TaS_2. *Nat Mater*. **7**, 960-965 (2008).

55. Wang, B. *et al*. Universal phase diagram of superconductivity and charge density wave versus high hydrostatic pressure in pure and Se-doped 1*T*-TaS_2. *Phys. Rev. B* **97**, 220504(R) (2018).

56. Moulding, O. Osmond, I. Flicker, F. Muramatsu, T. & Friedemann, S. Absence of superconducting dome at the charge-density-wave quantum phase transition in 2*H* -$NbSe_2$. *Phys. Rev. Research* **2**, 043392 (2020).

57. Klintberg, L. E. *et al*. Pressure- and Composition-Induced Structural Quantum Phase Transition in the Cubic Superconductor $(Sr,Ca)_3Ir_4Sn_{13}$. *Phys. Rev. Lett.* **109**, 237008 (2012).

58. Goh, S. K. *et al*. Ambient Pressure Structural Quantum Critical Point in the Phase Diagram of $(Ca_xSr_{1-x})_3Rh_4Sn_{13}$. *Phys. Rev. Lett.* **114**, 097002 (2015).

59. Moncton, D. E., Axe, J. D. & DiSalvo, F. J. Neutron scattering study of the charge-density wave transitions in 2*H*-$TaSe_2$ and 2*H*-$NbSe_2$. *Phys. Rev. B*

16, 801 (1977).

60. Yokota, K. *et al*. Superconductivity in the quasi-two-dimensional conductor 2*H*-$TaSe_2$. *Physica B Condens. Matter.* **284**, 551 (2000).

61. Bhoi, D. *et al*. Interplay of charge density wave and multiband superconductivity in 2*H*-Pd_xTaSe_2. *Sci. Rep.* **6**, 24068 (2016).

62. L. Li *et al*. Superconducting order from disorder in 2*H*-$TaSe_{2-x}S_x$. *npj Quant. Mater*. **2**, 11 (2017).

63. Borisenko, S. V. *et al*. Pseudogap and charge density waves in two dimensions. *Phys. Rev. Lett.* **100**, 196402 (2008).

64. Kadowaki, K. and Woods, S. Universal relationship of the resistivity and specific heat in heavy-fermion compounds. *Sol. State Comm.* **58**, 507 (1986).

65. Jacko, A. C. Fjæ restad, J. O. & Powell, B. J. A unified explanation of the Kadowaki–Woods ratio in strongly correlated metals. *Nat. Phys.* **5**, 422 (2009).

66. Hashimoto, K. *et al*. Evidence for superconducting gap nodes in the zone-centered hole bands of KFe_2As_2 from magnetic penetration-depth measurements. *Phys. Rev. B* **82**, 014526 (2010).

67. Hill, H. M. *et al.* Phonon origin and lattice evolution in charge density wave states. *Phys. Rev. B* **99**, 1 (2019).

68. Petkov, V. *et al*., Genesis of the periodic lattice distortions in the charge density wave state of 2*H*−$TaSe_2$. *Phys. Rev. B* **101**, 121114 (2020).

69. Xu, S. *et al*., Superconducting phase diagrams of S-doped 2*H*-$TaSe_2$ under hydrostatic pressure. *Phys. Rev. B* **102**, 184511 (2020)

70. Klein, M. V. Theory of two-phonon Raman scattering in transition metals and compounds. *Phys. Rev. B* **24**, 4208 (1981).

71. Sur, Y. *et al*., Pressure-induced quantum critical point of a strong coupling charge density wave order in 2*H*-$Pd_{0.05}TaSe_2$. *unpublished*.

Appendix A Operation of the cubic anvil cell apparatus and the characterization of pressure-induced superconductivity in $TaIrTe_4$

A.1 Introduction

The cubic anvil cell apparatus is a multi-anvil press specifically designed to generate hydrostatic pressure conditions, in constrast to the double anvil press methods that are utilized in the piston cylinder cell and the diamond anvil cell. Due to the presence of six anvils, which pressurize the sample in all three *x*- *y*- and *z*- directions, this apparatus can generate hydrostatic pressures in a large sample space exceeding 1 mm^3 in length. Moreover, the cubic anvil cell apparatus can provide constant pressure feedback even during measurement, which enables the maintenance of constact pressure conditions in both the cooling and warming runs. This, in turn, allows the measurement of intrinsic temperature dependence of the sample, measured under various pressure conditions.

In this chapter, The basic operational sequence of the cubic anvil cell apparatus is introduced. Furthermore, a new discovery of the pressure-induced superconductivity in a type II Weyl semimetal $TaIrTe_4$ is presented, along with the experimental progress related to this finding.

A.2 Experimental details

To conduct a cubic anvil cell measurement, several items must be prepared in advance. One crucial item is the pyrophyllite gasket, which is used to encapsulate the sample. The following paragraph provides the step-by-step instructions for engraving the pyrophyllite gasket from a pyrophyllite plate.

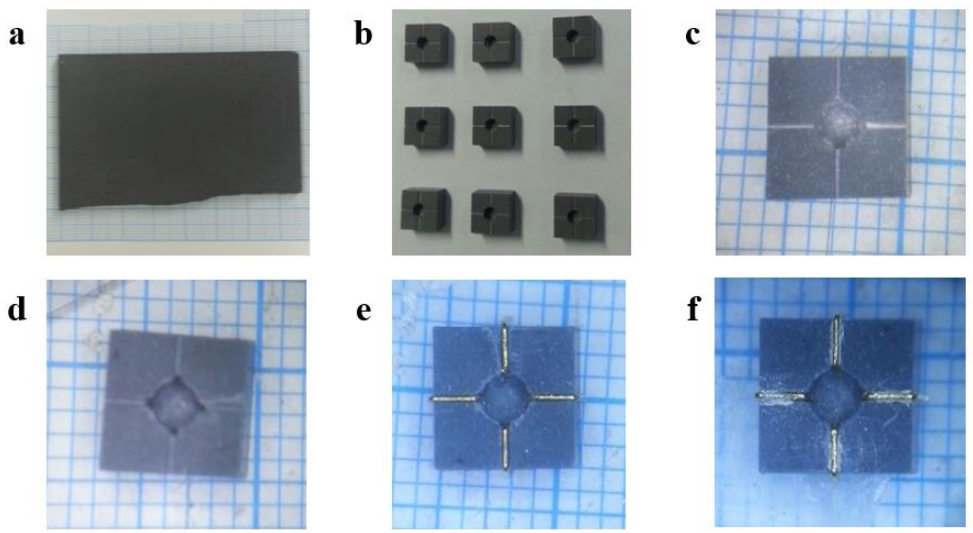

Figure A.1 (**a**) a photograph is provided of a pyrophyllite plate with a thickness of 7mm. (**b**) Engraved pyrophyllite gaskets with dimensions of 6mm in length and 3mm in height, which were made using the pyrophyllite plate in figure A1**a**. (**c**) A photo of an engraved gasket before additional preparation. (**d**) A pyrophyllite gasket with an inner section that was manually drilled to make room for the 100 μm Φ gold wires. (**e**) The same gasket as in figure A1**d**, with gold wires placed in the engraved hole. (**f**) The prepared pyrophyllite gasket with gold wires attached to the engraved hole using silver paste (Dupont 4929N).

To prepare pyrophyllite gaskets for a cubic anvil cell measurement, a large block of pyrophyllite is first cut to a depth of 7mm and affixed to a

gasket engraver with Loctite glue. Using a 3.18mm blade, the pyrophyllite plate is reduced to a depth of 3mm and cut into 6mm gaskets, which include 2Ø holes for the Teflon cup and 0.25mm lines for the gold foil. These gaskets go through annealing at 700℃, causing their dimensions to change from 6.03mm to 6.10mm. For the upper gasket, holes are drilled for 0.25mm gold wire by a hand drill, and the wires are loaded and attached using silver paste. Various stages in the preparation of pyrophyllite gaskets are shown in Figure A1, including a photograph of the pyrophyllite plate, engraved pyrophyllite gaskets, an engraved gasket before additional preparation, a pyrophyllite gasket with an inner section drilled to make room for 100 μm Φ gold wires, the same gasket with gold wires placed in the engraved hole, and the final prepared pyrophyllite gasket with gold wires attached to the engraved hole using silver paste (Dupont 4929N).

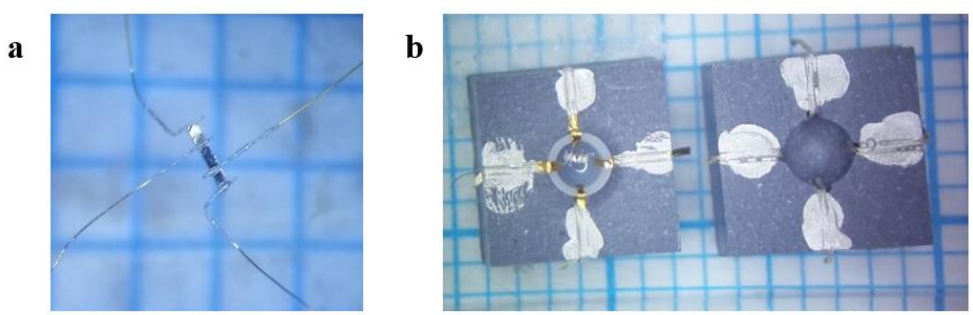

Figure A.2 (**a**) A metallic sample of length 0.8 mm which has been prepared using the four-probe contact configuration. Various stages in the preparation of pyrophyllite gaskets. (**b**) a photograph of a prepared pair of the pyrophyllite gaskets, with the sample loaded inside the teflon cup.

After the gasket is prepared, a sample of size no more than 1.5 mm should be prepared using the four-probe contact configuration. However, as the cubic anvil cell requires the contacts to be facing at four different directions, one of the voltage contacts should be attached upside down, as seen in Figure A2**a**. The gaskets should be then prepared in two separate pieces, the lower gasket and the upper gasket. For the lower gasket, a teflon cup is placed in the center, and a gold foil is attached with Loctite to the gasket to surround the teflon cup, as visualized in Figure A2**b**. The end of the gold foil should be placed above the teflon cup. Next, the sample is inserted into the Teflon cup. The four contact wires of the sample should be carefully placed beneath the gold foil. The teflon cup is then sealed, and the upper gasket is fitted on top the lower gasket and the sealed teflon cup. The unified gasket is then ready for the measurement.

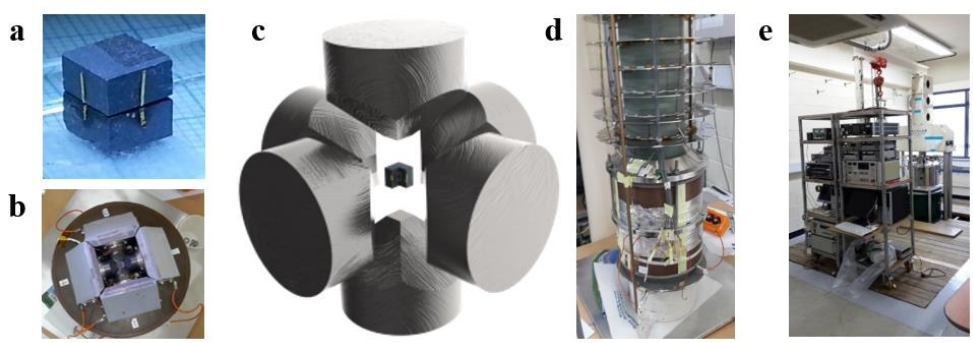

Figure A.3 (**a**) A photograph of a unified gasket ready for the cubic anvil cell measurement. (**b**) A photograph of the unified gasket loaded onto the four anvils in the *xy*-plane. The additional anvils in the up and bottom consist the six anvils required for the cubic anvil cell. (**c**) A schematic figure of the six anvils of the cubic anvil cell, with the unified gasket inside. (**d**) A photograph of a cubic anvil cryostat capable of cooling down to a temperature of 3.0 K. (**e**) A photograph of

the entire cubic anvil press along with the necessary electronics.

Figure A3**a** depicts the unified gasket with the sample loaded inside. This gasket is then inserted between the six anvils of the cubic anvil apparatus, as shown in Figures A3**b-c**. The six anvils are then clamped to the cryostat displayed in in Figure A3**d**, which is finally loaded into the cubic anvil system shown in Figure A3**e**. The cubic anvil cell is capable of applying pressures up to 8.5 GPa and reaching temperatures as low as 3.0 K, with a magnetic field capability of 5 T.

A.3 Liquid Helium cool down and warmup process

In the cubic anvil cell, both the sample and the anvil itself must be cooled. To conserve the costly liquid helium used for cooling, the cryostat is first cooled to 77 K using liquid nitrogen before the liquid helium is introduced. Below, I outline the five procedures for the daily transfer process:

1. Anvil press: Stabilize the cryostat at 280 K. Upon reaching 280 K, adjust the oil pump rate to 0.5 ml/min to slowly increase the pressure. Set the "target tons" to the desired pressure. Once the target pressure is attained, change the pump oil rate to 7.0 ml/min to maintain the current pressure through rapid feedback.

2. Nitrogen cooling: Confirm that the pump oil rate is 7.0 ml/min. Figure A4 shows a photograph of the different transfer lines within the cubic

anvil cell cryostat. Open the cryostat bottom-end valve and slightly open the LN_2 dewar valve. As the cryostat pressure starts to rise, open the cryostat top-end valve. Monitor the cryostat pressure to keep the gauge value within the green range. (Excessive flow may disrupt measurements). Be careful not to step on the cables, as the wires are sensitive to touch.

3. Nitrogen blowout: Once the cryostat temperature reaches 77 K, wait about 5 minutes for stabilization. Then, stop the nitrogen transfer by closing both the dewar and cryostat bottom-end valves. Connect the cryostat bottom-end and N_2 jacket bottom-end, ensuring the N_2 top-end is open. (Liquid nitrogen will be blown from the cryostat to the N_2 jacket.) Inject gaseous nitrogen into the cryostat top-end, making sure the cryostat pressure value stays within the green range. After the cryostat is emptied of LN_2 and its pressure drops to 0, close the cryostat bottom-end valve and stop the nitrogen gas injection. Close the N_2 jacket bottom-end and top-end valves (a relief valve is present on the N_2 jacket, allowing both to be closed). Disconnect the rotary output from the recovery port and connect it to the hose leading outside the room. Vacuum the cryostat using the bottom-end valve and ensure the pressure gauge reaches the lowest value. (If it does not, there may still be LN_2 in the cryostat.) Purge and vacuum three times using helium gas.

4. Helium cooling: Connect the cryostat top-end to the recovery line and transfer liquid helium. As the temperature drops to 4 K and the cryostat contains sufficient helium (approximately 40%), remove the transfer tube and start pumping with the large rotary pump located below. (A heat gun must be

used to defrost the line leading to the rotary pump to prevent damage.) Switch the LabVIEW program to the heating file and initiate the measurement.

5. Heating: Do not intervene until the temperature reaches 20 K, as the anvil's low heat capacity in this range allows for automatic heating. After reaching 20 K, use the heater to apply voltage very slowly (0.5 V per minute) and wait approximately 14 hours for the sample and the cryostat system to reach room temperature.

Figure A.4 A photograph displays the different transfer lines within the cubic anvil cell cryostat. The area enclosed by red boundaries denotes the liquid helium transfer lines, while the area enclosed by green boundaries signifies the liquid nitrogen transfer lines.

A.4 Investigation of the high-pressure resistivity in

$TaIrTe_4$

In this chapter, the in-plane resistivity data of $TaIrTe_4$ under high pressures up to 8.5 GPa will be discussed. $TaIrTe_4$ is a recently discovered compound, which was identified by a former alumnus of Prof. Kee Hoon Kim's research group, Dr. Seunghyun Kim [1, 2]. This compound constitutes the third member of type II Weyl semimetals, with WTe_2 and $MoTe_2$ being the first and second members, respectively. In Weyl semimetals such as WTe_2 and $MoTe_2$, large magnetoresistance values stemming from the Weyl points typically show suppression under pressure, and exhibit the presence of superconductivity near the magnetoresistance suppression point [3, 4]. Given that $TaIrTe_4$ is also a Weyl semimetal, there is a high possibility of pressure-induced superconductivity in this compound, reminiscent to those observed in WTe_2 and $MoTe_2$. Therefore, to investigate the possibility of superconductivity in $TaIrTe_4$ under high pressure, we have measured the temperature dependence of in-plane resistivity of $TaIrTe_4$ under high pressures up to 8.5 GPa.

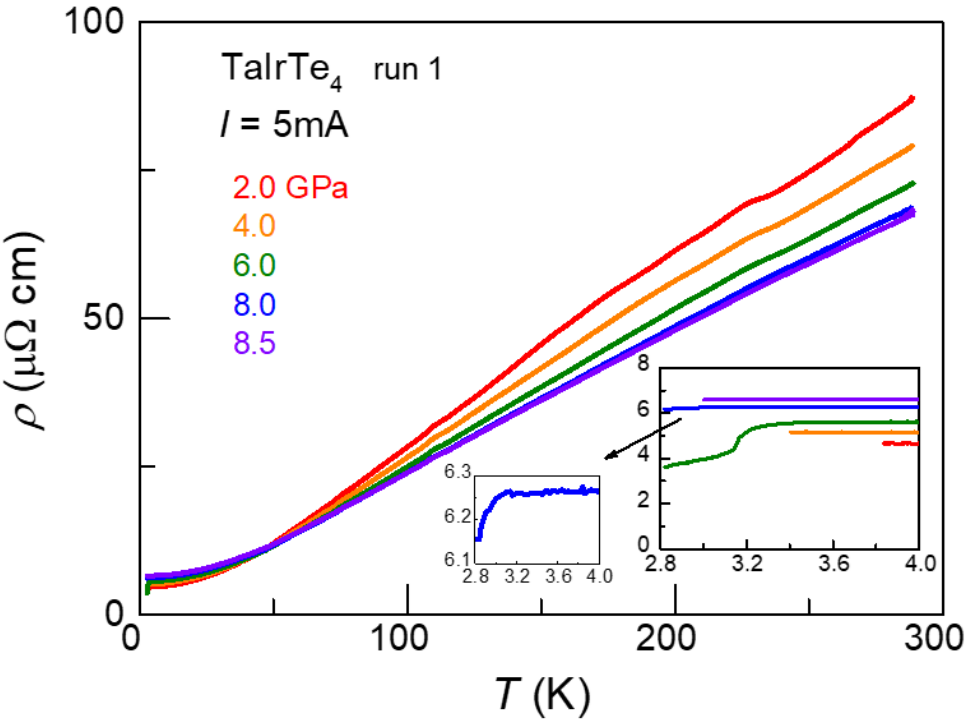

Figure A.5 In-plane resistivity *vs.* temperature plot of $TaIrTe_4$ at various pressures in the first pressure run. The applied current is set to 5 mA. (inset 1) A magnefied plot of low temperature in-plane resistivity vs. temperature of $TaIrTe_4$. (inset 2) A magnefied plot of low temperature in-plane resistivity vs. temperature of $TaIrTe_4$ for P = 8.0 GPa. A small downturn in the resistivity near 3 K indicates the onset of the superconducting transition.

Figure A5 illustrates the in-plane resistivity versus temperature plot for $TaIrTe_4$ at various pressures during the initial pressure run inside a cubic anvil cell. It is evident that resistivity measured at room temperature decreases with increased pressure, while resistivity at low temperatures rises with higher pressure. This suggests that the residual resistivity ratio (RRR) diminishes under pressure. In addition to this feature, an enlarged plot of low-temperature resistivity in the inset of Figure A5 reveals a downturn in resistivity at specific

pressures of 6 GPa and 8 GPa. This behavior is reminiscent of the superconductivity potentially expected in type II Weyl semimetals under high pressure. However, the zero resistivity characteristic of superconductivity was not observed down to the low-temperature limit of approximately 2.8 K, indicating that further measurements are necessary to ascertain the nature of this decrease in in-plane resistivity.

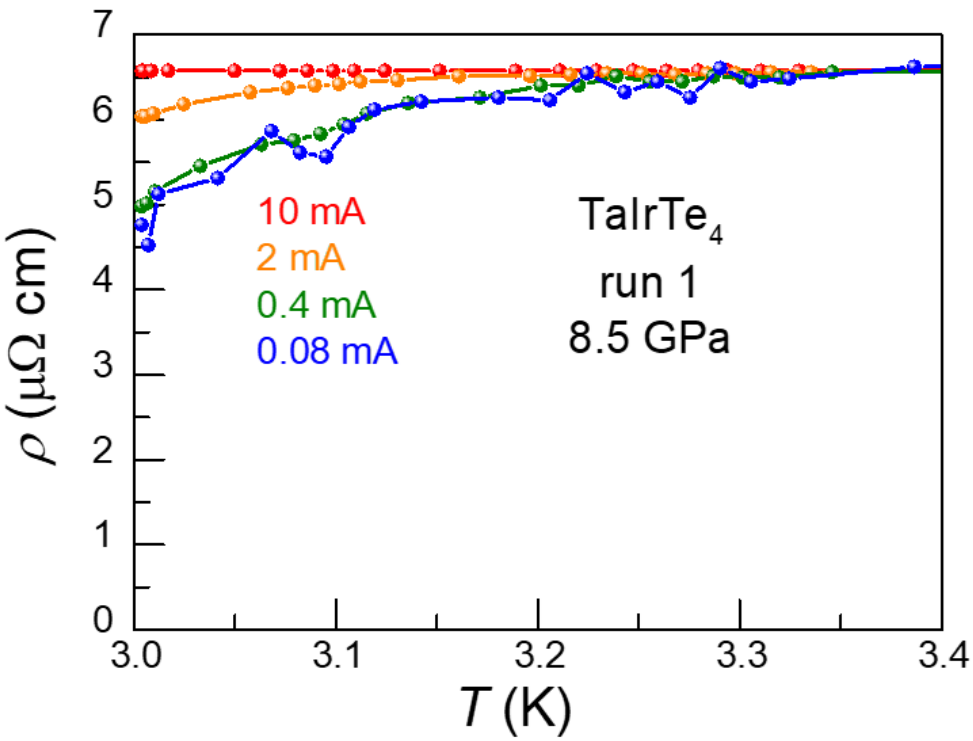

Figure A.6 A magnefied plot of the in-plane resistivity *vs*. temperature plot of $TaIrTe_4$ at 8.5 GPa in the first pressure run. The in-plane resistivity is measured under various applied current values, in order to characterize the nature of the resistivity downturn.

In order to investigate the nature of the decrease in in-plane resistivity near 3 K at high pressures, the in-plane resistivity of $TaIrTe_4$ at 8.5 GPa is

measured with various applied current. As shown in Figure A6, the resistivity downturn is highly dependent on the applied current, suggesting that the decrease in resistivity likely originates from superconductivity. Nevertheless, further measurements are undoubtedly necessary to attribute this feature to superconductivity, as neither of the two hallmarks of superconductivity—zero resistance nor perfect diamagnetism—has been observed in this system. If, however, this assertion proves to be accurate, our measurements indicate that the critical current for superconductivity at this pressure would lie between 2 mA and 10 mA.

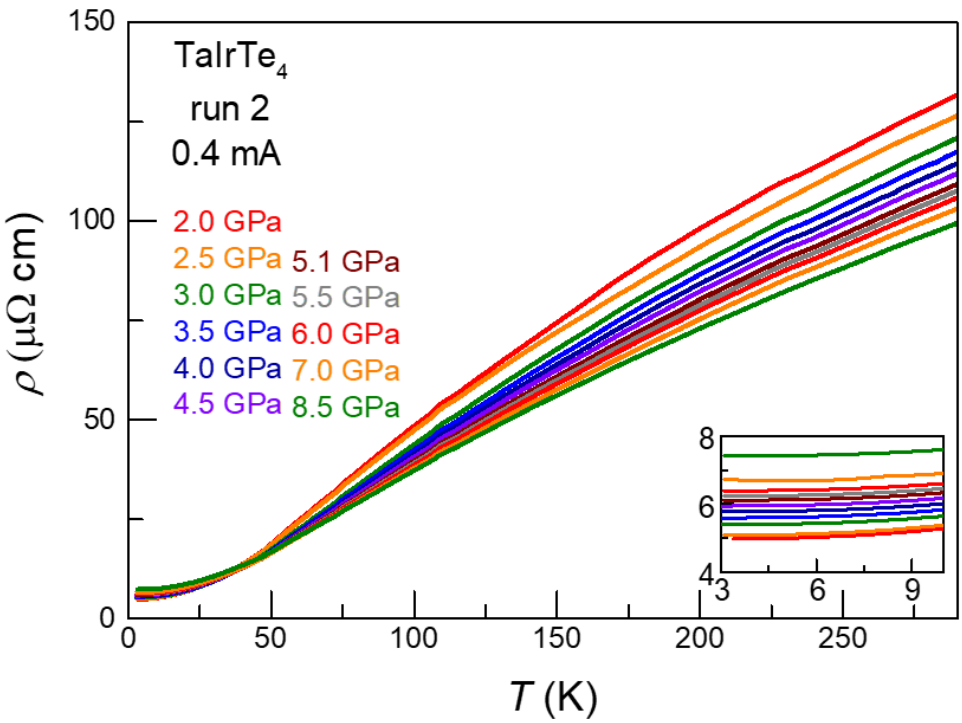

Figure A.7 In-plane resistivity *vs.* temperature plot of $TaIrTe_4$ at various pressures in the second pressure run. The applied current is set to 0.4 mA. (inset) A magnefied plot of low temperature in-plane resistivity vs.

temperature of $TaIrTe_4$.

To further confirm the existence of superconductivity in $TaIrTe_4$ at high pressures, an additional high-pressure experiment was conducted on the material. Figure A7 presents the in-plane resistivity versus temperature plot for $TaIrTe_4$ under various pressures during the second pressure run inside a cubic anvil cell. It is important to note that the applied current was reduced to 0.4 mA to better detect potential signatures of superconductivity in this second run. However, contrary to expectations, the resistivity measurements in this additional run did not reveal any signs of superconductivity, which is in stark contrast to the initial run. This trend can be clearly seen in the inset of Figure A7, which displays a magnified plot of low-temperature in-plane resistivity versus temperature for TaIrTe4. In this inset, no downturn in resistivity is observed, suggesting the absence of superconductivity in the second run.

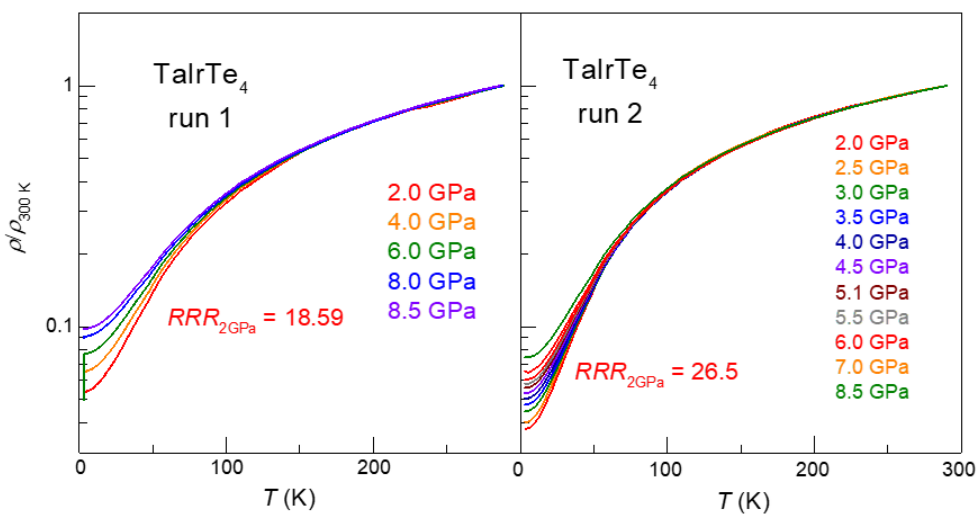

Figure A.8 The temperature dependence of the in-plane resistivity divided by room temperature resistivity of $TaIrTe_4$ at various pressures in the initial

pressure run (left) and the second pressure run (right). The residual resistivity ratio (RRR) of the samples measured at 2 GPa is shown for comparion.

The discrepancy between the two runs within the same compound is indeed challenging to comprehend. To understand this behavior and investigate the intrinsic properties of $TaIrTe_4$ under pressure, the temperature dependence of the in-plane resistivity divided by room temperature resistivity of $TaIrTe_4$ at various pressures in both the initial and second pressure runs has been plotted. By analyzing the residual resistivity ratio (RRR) of the two samples measured at 2 GPa, it can be concluded that the sample from the second run exhibits a higher RRR value of 26.5, compared to the RRR value of 18.6 in the first pressure run. A high RRR value is indicative of low impurity scattering and suggests a higher sample quality. This implies that the sample measured in the second run is of superior quality and more representative of the intrinsic properties. As a result, the absence of superconductivity can be considered the more intrinsic behavior of $TaIrTe_4$ under pressure. The pressure-induced superconductivity observed in the first pressure run of $TaIrTe_4$ may be attributed to a slight tellurium deficiency in the initial run, as such deficiency can sometimes promote superconductivity by acting as an electron donor and affecting the Fermi surface [5].

Bibliography

[1] K. Koepernik *et al*., $TaIrTe_4$: A ternary type-II Weyl semimetal. *Phys. Rev. B* **93**, 201101(R) (2016).

[2] S. Khim *et al*., Magnetotransport and de Haas–van Alphen measurements in the type-II Weyl semimetal $TaIrTe_4$. *Phys. Rev. B* **94**, 165145 (2016).

[3] Y. Qi *et al*., Superconductivity in Weyl semimetal candidate $MoTe_2$. *Nat. Commun*. **7**, 11038 (2016).

[4] X. –C. Pan *et al*., Pressure-driven dome-shaped superconductivity and electronic structural evolution in tungsten ditelluride. *Nat. Commun*. **6**, 7805 (2015).

[5] S. Cho *et al*., Te vacancy-driven superconductivity in orthorhombic molybdenum ditelluride. *2D Materials* **4**, 021030 (2017).

List of publications

1. Superconductivity optimization in the vicinity of a nematic quantum critical point in the kagome superconductor $Cs(V_{1-x}Ti_x)_3Sb_5$. **Yeahan Sur**, Kwang-Tak Kim, Sukho Kim, and Kee Hoon Kim. *Nat. Commun*. **14**, 3899 (2023)

2. Pressure-induced quantum critical point of a strong coupling charge density wave order in 2*H*-$Pd_{0.05}TaSe_2$. **Yeahan Sur**, Dilip Bhoi, Dong Hyun Jang, Kai Zhang, Ziyu Cao, Zhehao Gu, Jiawei Hu, Viktor V. Struzhkin, Xiao-Jia Chen, Keizo Murata, and Kee Hoon Kim. *In preparation.*

3. Solvothermal Synthesis and Interfacial Magnetic Interaction of *β*-FeSe/$SrTiO_{3-x}$ Nanocomposites. Seok Huh, Kang Hyun Song, Hee Jung Yang, Si Eun Jang, Kyungtae Kim, **Yeahan Sur**, Kiwan Nam, Kee Hoon Kim, Nam Hwi Hur. *ChemistrySelect* **5**, 30 (2020).

4. Experimental signatures of nodeless multiband superconductivity in a 2*H*-$Pd_{0.08}TaSe_2$ single crystal. Chanhee Kim, Dilip Bhoi, **Yeahan Sur**, Byung-Gu Jeon, Dirk Wulferding, Byeong Hun Min, Jeehoon Kim, and Kee Hoon Kim. *Sci. Rep.* **11**, 13383 (2021).

5. Interplay of charge density waves, disorder, and superconductivity in 2*H*-$TaSe_2$ elucidated by NMR. Seung-Ho Baek, **Yeahan Sur**, Kee Hoon Kim, Matthias Vojta, and Bernd Büchner. *New J. Phys.* **24**, 043008 (2022).

6. Pressure-dependent structure of $BaZrO_3$ crystals as determined by Raman Spectroscopy. Dong-Hyeon Gim, **Yeahan Sur**, Yoon Han Lee, Jeong Hyuk

Lee, Soonjae Moon, Yoon Seok Oh, and Kee Hoon Kim. *Materials* **15**, 4286 (2022).

List of patents

1. 초전도 구동 모터용 초전도 소재 개발. **서예환**, 이중우, 김석호, 김기훈. *출원 진행중*.

국문 초록

절대 영도에서 발현되는 상전이를 의미하는 양자 상전이 현상은, 100년 이상 동안 응집물질물리학 분야에서 중요한 현상으로 간주되어 왔다. 물리학적으로 매우 드물게 일어나는 이 양자 상전이 현상은, 어떠한 물질의 온도에 따른 이차 상전이 온도가, 온도와 관련없는 매개 변수 g에 의해 T = 0 K 에 도달하는 현상으로 정의된다. 이러한 현상이 일어나는 상 공간 근방에서는, 정렬된 상의 상관 시간 (correlation time) ξ_τ이 $\xi_\tau \propto 1/[\, g - g_c]^{\nu z}$의 공식을 따르게 되며, 여기서 $\boldsymbol{\nu}$ 는 상관 길이, $\boldsymbol{z}$는 동적 지수이고 g_c 는 매개 변수가 양자 임계점에 도달하는 지점이다. 특이하게도, $g = g_c$ 인 상 공간 근처에서는 상관 시간 ξ_τ이 발산하여 열적 시간 척도 L_τ 보다 커지게 되고, 물질의 기본 상태는 정렬된 상과 무질서한 상의 파동 함수가 중첩된 요동 (fluctuation) 상태로 정의된다. 이 근방의 물리적 특성은 하이젠베르크의 불확실성 원리와 관련된 양자 요동 (fluctuation)에 의해 결정되기 때문에, 초전도와 같은 독특한 물리적 특성이 형성될 수 있다. 본 논문에서는 다양한 상의 양자 임계점과 그 근방에서 나타나는 초전도 상에 대하여 연구를 진행하였다.

첫째로, 카고메 금속 $Cs(V_{1-x}Ti_x)_3Sb_5$에서 전하밀도파, 네마틱 상, 그리고 초전도 상 간의 상관관계가 연구되었다. 이 연구에서는 고품질의 $Cs(V_{1-x}Ti_x)_3Sb_5$ ($0 \leq x \leq 0.06$) 단결정을 성공적으로 합성하여, 파장 분산 X선 분광법 (wavelength-dispersive X-ray spectroscopy, WDS) 과 X선 회절(X-ray diffraction, XRD) 측정을 통해 정확한 도핑 비율과 체계적인 격자 상수의 변화를 측정하였다. Ti 도핑에 따른 네마틱 상과 초전도 상의 상관 관계를 탐구하기 위하여, 네마틱 감수율 측정을 진행하였으며, 그 결과 $Cs(V_{1-x}Ti_x)_3Sb_5$ 단결정의 Curie-Weiss 온도 θ_{nem}이 Ti 도핑에 따라 억제되며, $x \sim 0.009$에서 음수가 됨을 발견하였다. 또한, 임계 도핑 $x_c = 0.01$ 근방에서 Curie 상수 C와 네마틱 감수율 $\tilde{n}$이 최대값을 보이는 것을 통해, x_c

근방에서 네마틱 양자 임계점 (nematic quantum critical point, NQCP)이 존재한다는 강한 증거를 발견하였다. 추가로, 이 NQCP 근방에서 초전도 성질을 탐구한 결과, 초전도 전이온도와 초전도 부피비가 Ti 도핑에 따라 이례적인 이중 초전도 돔 모양을 띰을 관측하였으며, 첫번째 돔이 NQCP 인근에 위치함을 발견하였다. 이러한 관측 결과는, $Cs(V_{1-x}Ti_x)_3Sb_5$ 물질의 첫 번째 초전도 돔 근방에서 네마틱 양자 요동 (quantum fluctuation)이 초전도 전이 온도를 상승시키는 역할을 할 가능성을 시사하는 결과로서 학술적 의미가 크다.

둘째로, 전이 금속 찰코겐화합물 $2H$-$Pd_{0.05}TaSe_2$에서 강한-결합전하밀도파 상과 초전도 상 간의 상관 관계가 연구되었다. 구체적으로는, 전하밀도파 상전이 온도 T_{CDW} = 115 K 및 초전도 상전이 온도 T_c = 2.6 K를 띄는 $2H$-$Pd_{0.05}TaSe_2$ 단결정에서 압력에 따른 전기 수송 및 포논 진동 측성을 탐색하였다. 이를 통해, 압력이 인가되었을 때, 저항과 홀 계수 측정을 통해 전하밀도파 상전이 온도 T_{CDW}가 점차적으로 감소하여 임계 압력 P_c ~ 22.1 GPa에서 0K 근방에 도달함을 실험적으로 확인하였다. 추가적으로, $\mu_0 H$ = 9 T의 일정한 자기장을 인가한 상태에서 측정된 저항을 $\rho = \rho_0 + AT^2$ 피팅을 이용하여 분석한 결과, 이차항의 계수값 A가 P_c 근방에서 약 5배 증가함을 발견하여 이 근방에서 전자 상태 밀도가 크게 증가함을 관측하였다. 이에 더해, 라만 측정을 통하여 약 21.8 GPa 근방에서 이 물질의 전하밀도파 형성의 원인이 되는 Kohn anomaly가 사라지는 현상을 발견하였다. 이러한 결과들은, $2H$-$Pd_{0.05}TaSe_2$에서 압력을 통한 전하밀도파 양자임계점이 존재한다는 강력한 실험적 증거로서 의미가 크다.

주요어 : 양자 임계점, 단결정 성장, 준2차원 물질, 초전도, 전하밀도파, 네마틱 상, 도핑,압력, 응력

학번 : 2015-20330